# Multinuclear Solid State NMR Studies of $\alpha$-Tricalcium Phosphate and Silicon Substituted $\alpha$-Tricalcium Phosphate

A Thesis Submitted to the University of Warwick for the Degree of
Doctor of Philosophy

James F.MacDonald

University of Warwick, Department of Physics

THE UNIVERSITY OF
WARWICK

# Abstract

$\alpha$-tricalcium phosphate ($\alpha$-TCP, $Ca_3(PO_4)_2$) demonstrates both bioactive and resorbable characteristics. Substitution of $SiO_4^{4-}$ for $PO_4^{3-}$ in $\alpha$-TCP (Si-$\alpha$-TCP) is found to stabilize the structure at lower temperatures and improve mechanical (and possibly bioactive) properties. The mechanism of electroneutrality in the Si-$\alpha$-TCP structure is not fully understood, though is thought to take place through the creation of $O^{2-}$ vacancies or through excess $Ca^{2+}$. This study addresses some structural properties of $\alpha$-TCP using $^{31}P$ MAS NMR at intermediate $B_0$ fields (11.7 T) and $^{43}Ca$ DOR NMR at multiple fields (20.0 T, 14.1 T, 11.7 T), and via correlation of the measured $^{31}P$ and $^{43}Ca$ isotropic chemical shifts ($\delta_{iso}$) against calculated values obtained with GIPAW DFT methods using the CASTEP code. These results show that the structure has high short range order and clearly support the monoclinic $P2_1/a$ (12 P site/18 Ca site) model.

In contrast, solid state $^{31}P$ MAS and $^{43}Ca$ DOR NMR studies of Si-$\alpha$-TCP demonstrate that significant disorder broadening is characteristic of these data, however the corresponding $^{29}Si$ MAS NMR data affords reasonably resolved resonances, a low intensity $Q^2$ resonance at $\delta_{iso}$ –84.5 ppm, and multiple resonances in the range $\delta_{iso} \sim$ –70 $-$ –75 ppm, despite this shift range normally associated with $Q^0$ speciation, $^{29}Si$ refocused-INADEQUATE data shows that $Q^1$ resonances can also exist in this region. $^{31}P$-$^{29}Si$ HETCOR data from these systems suggests that, despite the intrinsic disorder, explicit $PO4^{3-}$ framework species can be associated with the different $Q^0/Q^1$ Si species, and while there is some dispersion of the silicon throughout the structure it is predominantly associated with a small number of P sites. DFT calculations for the Si-$\alpha$-TCP system suggest that the more favourable mechanism for charge balance is $Ca^{2+}$ excess, despite this, the $^{29}Si$ NMR data is in greater agreement with the DFT calculations for the $O^{2-}$ mechanism, whereby two adjoining cation-anion-columns in the structure are bridged together by a $Q^1$ unit , $^{29}Si$ NMR data also suggests the existence of $Ca_2SiO_4$ and $Ca_3Si_3O_9$ existing as solid solutions within the $\alpha$-TCP structure.

# Acknowledgments

# Declaration

This thesis is submitted to the University of Warwick in support of my application for the degree of Doctor of Philosophy. I hereby declare that this thesis written under the supervision of Dr. John V. Hanna has been entirely composed by myself and has not been submitted in any previous application for any degree, all work contained within is entirely my own unless specifically acknowledged or referenced.

James F. MacDonald

November 2012

# Contents

# Abbreviations

| | |
|---|---|
| $C_2S$ | Dicalcium silicate |
| CSA | Chemical shift anisotropy |
| CP | Cross polarisation |
| DFT | Density functional theory |
| DOR | Double angle rotation |
| DQ | Double quantum |
| FT | Fourier transform |
| FTIR | Fourier transform infra-red |
| FID | Free induction decay |
| FWHH | Full width half height |
| GIPAW | Gauge including projector augmented waves |
| GGA | Generalized gradient approximation |
| H-H | Hartmann-Hahn |
| HETCOR | Heteronuclear correlation |
| HECToR | High-End Computing Terascale Resource |
| HMQC | Heteronuclear multiple quantum correlation |
| Ha | Hydroxyapatite |
| INADEQUATE | Incredible natural abundance double quantum transfer experiment |
| MAS | Magic angle spinning |
| MQDOR | Multiple quantum double angle rotation |
| ND | Neutron diffraction |
| NMR | Nuclear magnetic resonance |
| ppm | parts per million |
| PBE | Perdew, Burke and Ernzerhof |
| QIS | Quadrupole induced shift |
| RAPT | Rotor assisted population transfer |

| | |
|---|---|
| REDOR | Rotational echo double resonance |
| SEM-WDS | scanning electron microscopy-wavelength dispersive spectroscopy |
| S/N | Signal to noise |
| SS NMR | Solid state NMR |
| TCP | Tricalcium phosphate |
| XRD | X-ray diffraction |
| XRF | X-ray fluorescence |

# List of Figures

# List of Tables

# Chapter 1

# Introduction

## 1.1 Background

Historically there are many recorded uses of a variety of materials being used in the treatment of ailments and injuries to the human body. Devices such as prosthetic limbs, eye components and in the replacement of teeth are some of the advances that have been made to date [2]. The ever increasing demand for a better quality of life and advances in modern materials science this has given rise to the contemporary field of biomaterials. Biomaterials science is a large multidisciplinary area of research that encompasses engineering, physics, chemistry and medicine.

The word 'biomaterial' is used to describe a broad range of devices and materials, that find a use in anything from surgical instruments to medical implants, and are made from all classes of materials, e.g. polymers, metals, glasses, and ceramics [3]. Essentially a biomaterial can be defined as " *a nonviable material used in a medical device, intended to interact with biological systems*" [4]. The range of materials and their application is vast, apart from those that are purely cosmetic in nature, the widest application is intended to prolong or improve the quality of peoples lives by aiding the repair of body parts or as a replacement for a particular bodily function, where devices of varying complexity are fashioned to fulfil a specific task [5]. Of course, not all materials are suitable for use as a biomaterial; the suitability of a particular material is called the 'biocompatibility' and this is used to describe how well a material will perform

at a specific application and how the host will respond [4]. For example, a device intended to help repair cartilage, would not necessarily be good in the replacement of a load bearing joint and vice versa. Biocompatibility also takes into account the reaction of the local tissue to the implant, and how it affects repair and also how the implant is affected during this process. Thus, materials used for specific jobs have to be non-toxic, not cause any undesirable side-effects, and be accepted by the body and not be rejected. Hence, the biocompatibility of a material is not a particular property of the material, but is a measure of how well a material functions in a specific physiological application [5]

One specific area of biomaterial research and implementation, is in the area of orthopaedics [6], with the aim being to assist with repairs and/or to correct defects to the skeletal system. These devices can range from artificial hip and knee joints to pins and rods for the repair of breaks and fractures. A lot of repair methods make use of bone cements and fillers [5] and many of these are designed to be a close analogue to the hydroxyapatite mineral component of bone and to play an active part in the repair process [6–8]

Bone is a living tissue, just like the other tissues in the body. Bone consists of an inorganic organic matrix, where the organic part is permeated by the inorganic part [9], both parts of the bone matrix account for around 50 % by volume, however the inorganic part is considerably more by weight; representing $\sim 75\%$ compared to $\sim 25\%$ for the organic component [10]. The organic component consists of water, proteins, and collagen, the hydroxapatite mineral part it is not a pure hexagonal or monoclinic form of hydroxyapatite, but instead consists of many impurities or substituents, e.g. sodium, carbon, magnesium, strontium, and others [11, 12]. While the shape and type of bones (flat bones and long bones) varies throughout the skeleton and the mechanical properties differ considerably; the ratio of inorganic to organic components stays reasonably constant [9, 13]. During the lifetime of a skeleton, bone continuously undergoes a process called remodelling [13], this is the continued breakdown of older bone which is reabsorbed into the body and is then replaced by new bone growing in its place. The minerals involved in this process are transported to and from the skeleton by particular cells that lie on the surface of the bone [14], and stimulation of these cells

initiates bone remodelling through chemical stimuli and mechanical loading [15].

As mentioned above, one particular class of biomaterial used in orthopaedics is that of bone fillers and bone cements [16], and often these are ceramic materials that are used in the form of blocks or granular powders [17], they are chosen/designed to be similar in nature to the mineral component of bone, and as such are frequently made from the calcium phosphate family of minerals [6, 18]. Depending on the application, they are often porous [5] so that bone can grow through them and they become an integral part of the bone structure itself. Depending on the particular compound, it can be broken down slowly over time so that they are eventually replaced by natural tissue and take part in the natural process of remodelling [19, 20]; these are known as 'resorbable' materials [11]. Two of the more commonly studied calcium phosphates used as biomaterials are hydoxyapatite [21] and $\alpha$-tricalcium phosphate [1]. These materials vary greatly in their application due differences in structural properties and their rate of dissolution. A common practice is to substitute various ions into the structure with the aim to augment certain properties, such as improving the crystallinity and the rate of dissolution [11]. Some substitutions are aimed at improving the bioactivity of the material, and one such substitution is performed with Si [12,22,23], as it is believed that Si is essential to bone mineralisation [24] and that tissue reactions with the implant will be quicker. It has been reported that there is a marked difference in the reaction times between silica glasses and calcium phosphates [25].

While classification and structural determination of the pure forms of the materials used are relatively straightforward through the use of X-Ray diffraction (XRD) and neutron diffraction(ND) techniques, understanding the substituted variants is generally a lot more difficult. This is often due to the substitution levels being of only a few wt%, making it difficult to detect and successfully state where in the unit cell the substituted ions are located. Initial characterisation of substituted calcium phosphates is often achieved through the use of Fourier transform infra-red spectroscopy (FTIR) and Raman spectroscopy, with phase checks by XRD and possibly crystal structure refinements [23, 26, 27] However, performing full crystal structure refinements can be challenging and often requires neutron diffraction data, due to similarities in the P and Si X-ray scattering wavelengths. Some results regarding the hydroxyapatite phase

have been reported [28]. Nevertheless, satisfactory results can be difficult even with neutron data, even though there are few places Si can be located in the unit cell. However this is likely due to the charge balance mechanisms not being fully understood, there are seven proposed mechanisms for Si substitution into hydroxyapatite [29]. Likewise, there are also problems associated with determining the location of the Si, in Si substituted $\alpha$-tricalcium phosphate ($\alpha$-TCP). This structure has two proposed charge balance mechanisms [30] and the biggest problem , is that the unit cell is very large and as yet there is no full crystal structure refinement published, though there are a number of partial structure refinements from XRD [23, 31] and ND [29] studies. However, none of these make an attempt to refine atomic positions or Si location. The more obvious choice of technique to help clarify some of the unsolved structural problems would be solid state NMR (SS NMR), as the short range information it provides is highly complimentary to that of diffraction techniques, which are long range order techniques.

Solid state NMR has significantly advanced since its origins in the 1930's and 1940's. A historical account can be found in Andrew and Szczesniak [32]. This technique is capable of detecting the minute differences between chemical sites in a material, and there are also more advanced experimental techniques that allow for correlations between different nuclear species so that connectivity and positioning in crystal structures can be determined.

Solid state NMR is not without its challenges when studying calcium phosphates systems as they generally only have one or two abundant NMR active nuclei (i.e. $^{31}$P or $^{1}$H) to target. In contrast the elemental portions of these compounds are generally Ca and O which are very difficult nuclei to study using SS NMR, due to the very low natural abundance of $^{43}$Ca and $^{17}$O, (of each $< 1\%$). Similarly, when Si is substituted into these materials it is usually at the dopant level and also has a low natural abundance ($^{29}$Si $\sim 5\%$). These problems associated with SS NMR of substituted calcium phosphates are reflected in the literature, or rather, by the lack of literature. Despite the interest in such materials, there are (in general) very few studies on biomaterials and doped biomaterials using SS NMR, and these focus on the easier nuclei such as $^{1}$H and $^{31}$P [33, 34]. At the time of writing there are only four papers published, regarding Si

in calcium phosphates; two for hydroxyapatite [35] [36], one for $\beta$-TCP [37] and one for $\alpha$-TCP [38]. They are all limited to rudimentary single pulse methods reporting chemical shift data only, and consist of either multiphase samples or low quality data. Likewise, given the difficulties associated with $^{43}$Ca and $^{17}$O measurements, there are some studies [39–42] however there are none for $\alpha$-TCP.

## 1.2   Aims

The aims of this project are to undertake a comprehensive study of $\alpha$-TCP using solid state NMR and first principles GIPAW DFT calculations, and in order to investigate the changes that take place within the $\alpha$-TCP structure when $SiO_4{}^{4-}$ is substituted for $PO_4{}^{3-}$. The intentions are to gain some insight into how the extra negative charge from the $SiO_4{}^{4-}$ is balanced in the structure; i.e. whether it was through either $Ca^{2+}$ excess or through the formation of $O^{2-}$ vacancies as this has not been successfully demonstrated. This investigation also focuses on the location(s) of the substituted Si in the $\alpha$-TCP structure as it is not possible to determine this through diffraction methods. The large $\alpha$-TCP structure is notoriously difficult to refine and is exacerbated when substitutions at the few wt% dopant level are present, as it is not possible to accurately specify a location for the few substituted Si ions in the unit cell of 312 atoms.

The solid state NMR study of these systems focuses on three of the nuclei present in the sample, i.e. $^{31}$P, $^{29}$Si and $^{43}$Ca. While $^{31}$P is 100% naturally abundant, the other two are low abundance nuclei, so the $^{29}$Si and the $^{43}$Ca SS NMR studies reported are for isotopically enriched systems.. This maximises the ability of the SS NMR technique to detect changes to the local structure of $\alpha$-TCP caused by the Si incorporation, either through the $^{31}$P, $^{43}$Ca and $^{29}$Si measurements. In order to gain a complete understanding of the $\alpha$-TCP and the Si substituted (Si-$\alpha$-TCP) structures (and the relationship between them), homonuclear ($^{31}$P–$^{31}$P) and hetronuclear ($^{31}$P–$^{29}$Si) 2D correlation experiments have been carried out.

First principles GIPAW DFT calculations have been performed on the $\alpha$-TCP and the Si-$\alpha$-TCP structures with the aim of understanding how the $^{31}$P and $^{43}$Ca SS

NMR data are related to the crystal structure, and to determine the charge balance mechanism and the energetically more favourable locations for the Si species in the substituted unit cell.

## 1.3 Thesis Overview

In Chapter 2 the background theory of the magnetic resonance phenomenon is presented along with the theory behind the main internal interactions that influence the NMR experiment and are present. These interactions include the chemical shift, dipolar coupling, quadrupole coupling and J-coupling.

Chapter 3 provides details of the experimental methods used in solid state NMR related to this project, an overview of the spectrometer and some mechanical and pulse techniques used in solid state NMR for improving resolution. Also discussed are the specific NMR experiments that have been implemented in this thesis.

Chapter 4 details the $^{31}$P SS NMR study of $\alpha$-TCP, through the use of 1D magic-angle-spinning (MAS) experiments, and introduces the effect of sample impurities and its effect on the resultant MAS NMR data. In addition, 2D homonuclear dipolar re–coupling experiments on $\alpha$-TCP, accompanied by first principles GIPAW DFT calculations have been implemented on the $\alpha$-TCP structure, allows a precise and unambiguous assignment of the complicated $^{31}$P MAS NMR spectrum to be undertaken in relation to the crystal structure.

In chapter 5, a $^{31}$P and $^{29}$Si SS NMR study of Si-$\alpha$-TCP is reported. Starting with a comparison between the $^{31}$P data from the Si–$\alpha$-TCP and $\alpha$-TCP systems highlighting the observed changes. Changes in the observed 2D $^{31}$P homonuclear dipolar re–coupling data is also discussed. $^{29}$Si MAS NMR measurements on the labelled Si-$\alpha$-TCP system, along with the observed changes that occur based on the levels of Si incorporation, are reported and discussed. Determination of the existence of network forming $Q^1$ units in the sample through the use of the $^{29}$Si refocused-INADEQUATE experiment is presented, and a 2D $^{31}$P–$^{29}$Si hetronuclear correlation (HETCOR) study demonstrates the connectivity between the substituted Si and the surrounding P network. This analysis is discussed with the aid of calculations on the two charge balance

mechanisms, and assignment of the $^{29}$Si resonances to specific crystal sites within the $\alpha$-TCP structure is discussed.

In Chapter 6 a $^{43}$Ca study of $\alpha$-TCP and Si–$\alpha$-TCP, using MAS NMR and double angle rotation (DOR) NMR is presented and supported with GIPAW DFT calculations. The study presents the first reported $^{43}$Ca DOR results and provides the measurement of all 18 unambiguously resolved $^{43}$Ca resonances. This measurement also represents the largest number of resonances ever reported in a DOR spectrum. A variable field DOR study has allowed the quadrupolar product ($P_Q$) and isotropic shift ($\delta_{iso}$) to be determined for every site, and a partial assignment of the $^{43}$Ca resonances to the crystal sites was achieved. Linear correlations in isotropic chemical shift ($\delta_{iso}$) with the immediate local Ca environment is observed.

# Chapter 2

# Background Theory

## 2.1 Introduction

Nuclear Magnetic Resonance is a powerful spectroscopic technique used to probe the local environment of atomic sites. The theory of magnetic resonance and its application is covered in depth by a large volume of literature, those that have been used to source this material [43–51] cover the subject in varying detail. What will be covered here is the main background theory and its key points, starting with the classical description of magnetic resonance and then followed by the quantum mechanical description and the internal interactions.

## 2.2 A Simple Classical Description of NMR

Nuclear magnetic resonance is possible due to the intrinsic magnetism of the nucleus; all magnetically active nuclei that have a spin quantum number $I > 0$ posses angular momentum, and as a consequence of this they also have a magnetic moment $\mu$. By analogy, it can be convenient to think of the nuclear spin as a magnetic dipole, and if we consider a case of where we have just one such dipole then the magnetic moment of this dipole is proportional to the angular momentum

$$\mu = \gamma I \hbar \tag{2.1}$$

where $\hbar$ is Planck's constant $h/2\pi$. The constant of proportionality $\gamma$ is called the gyromagnetic ratio (units $\text{rad}^{-1}\text{T}^{-1}$) and each nucleus has a uniquely defined $\gamma$. The fact that each nucleus has a unique $\gamma$ means that (in principle) every magnetically active isotope can easily be distinguished from all others. The highest value of $\gamma$ for the stable nuclei is that of the proton ($^1$H) and corresponds to a precession frequency $\nu_0 = \gamma/2\pi = 42.6$ MHz per Tesla of applied magnetic field ($\mathbf{B}_0$).

If we now consider an idealised sample consisting of a large ensemble of identical spin $I = \frac{1}{2}$ nuclei or magnetic dipoles, there will exist a net magnetic moment equivalent to a bulk magnetisation $\mathbf{M}$. This is just the sum of the magnetic moment vectors per unit volume

$$\mathbf{M} = \sum_i \mu_i \qquad (2.2)$$

However we find in the absence of an external magnetic field the individual magnetic moments will point in all directions in space, in effect cancelling each other out (see Figure 2.1a) and there will be no bulk magnetisation (i.e. $\mathbf{M} = 0$). If this idealized ensemble is then placed in a static uniform magnetic field $\mathbf{B}_0$, then there is a slight preference for the magnetic moments to align with this magnetic field creating a bulk magnetisation (see Figure 2.1b). The proportion of nuclei that align with the magnetic
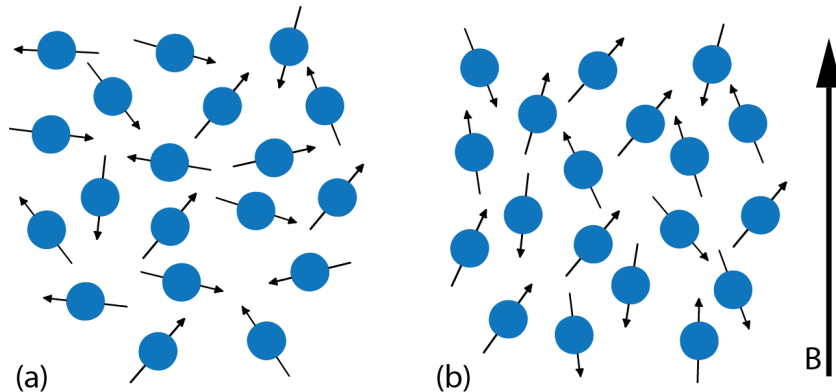


Figure 2.1: (a) In the absence of an external magnetic field the individual magnetic moments will point in all directions in space so that the average bulk magnetism will be zero (b) If placed in an external static magnetic field there will be a slight preference for the magnetic moments to align with the field, with those of a lower energy being parallel and those in the higher state being anti-parallel. As there are slightly more in the lower state then there will be a bulk magnet moment in the direction of $\mathbf{B}$

9

field is generally very small and is given by

$$\mathbf{M} = \frac{N\gamma^2 I(I+1)\hbar^2}{3kT}\mathbf{B}_0 \qquad (2.3)$$

which is considered to be a Curie-like relationship, where $N$ is the number nuclei, $k$ is the Boltzmann constant and $T$ is the temperature. At thermal equilibrium there will be slightly higher portion of the nuclei in the lower energy state caused by the Zeeman splitting of the ground state (see Section 2.4 ), those in the lower state align with the field and those in the higher energy state will be anti-aligned thus determining the magnetic moment. It is also apparent that the more spins in the ensemble that occupy the lower energy state will result in a larger magnetic moment. It follows from this that magnetic moment $\mathbf{M}$ will be related to the total angular momentum $\mathbf{L}$ of the system by

$$\mathbf{M} = \gamma\mathbf{L} \qquad (2.4)$$

The net magnetic moment will not actually align with magnetic field as it has angular momentum and the external field exerts a torque on the magnetic moment

$$\mathbf{T} = \mathbf{M} \times \mathbf{B}_0 \qquad (2.5)$$

and

$$\mathbf{T} = \frac{d}{dt}\mathbf{L} \qquad (2.6)$$

Then combining Equations 2.4 to 2.6 we get an expression describing the motion of $\mathbf{M}$ in the static field $\mathbf{B}_0$

$$\frac{d\mathbf{M}}{dt} = \gamma\mathbf{M} \times \mathbf{B}_0 \qquad (2.7)$$

If the magnetic moment is inclined to the field $\mathbf{B}_0$ at an angle $\theta$ then the net magnetic moment will precess in a cone (see Figure 2.2b) around the direction of the magnetic field at a constant angular frequency $\omega_0$, where

$$\omega_0 = -\gamma\mathbf{B}_0 \qquad (2.8)$$
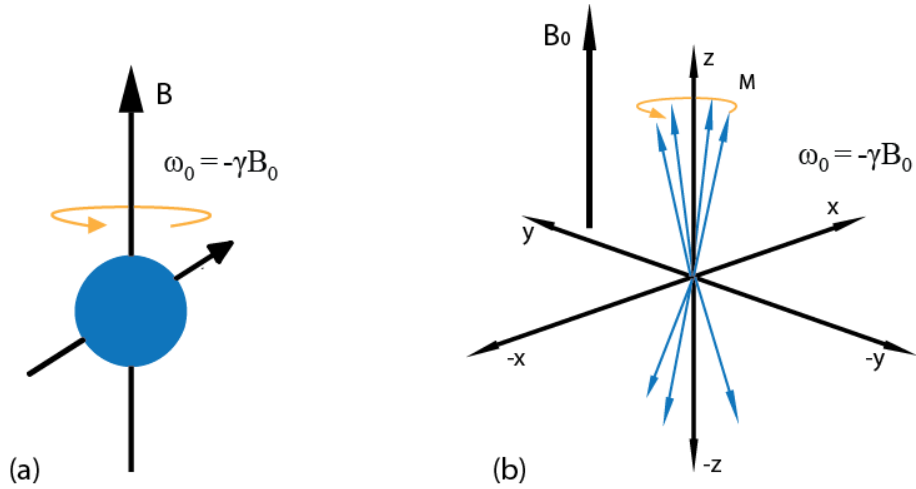
Figure 2.2: (a) In a static magnetic field nuclei with a spin $I > 0$ will precess around the field with frequency $\omega_0$ (b) When many nuclei are present they contribute to a bulk magnetism M which also precesses around $\mathbf{B}_0$ describing a cone with frequency $\omega_0$

.

$\mathbf{B}_0$ is the direction of the magnetic field and is usually defined to be in the $z$ direction in a Cartesian coordinate system, $\omega_0$ is called the Larmor frequency (however it is more often presented as $\nu_0 = \omega_0/2\pi$). The negative sign before $\gamma$ is related to the direction of the precession, as $\gamma$ can take positive or negative values. When looking along the direction of $\mathbf{B}_0$ then nuclei with a positive $\gamma$ precess in an anti-clockwise direction and those with a negative $\gamma$ precess clockwise however the consequences of this are usually ignored.

Now that a precessing magnet moment in a static uniform field model is established, this system can be perturbed if a second smaller magnetic field is applied using an oscillating electromagnetic wave of frequency $\omega_{rf}$ that is orthogonal to $\mathbf{B}_0$. This time dependent field can be represented by two vectors that are rotating in opposite directions in the $x$-$y$ plane and having frequencies $\pm\omega_0$. Only the component rotating in the direction of the precessing magnetization is important which will be called $\mathbf{B}_1$; the component rotating in the opposite direction will have little interaction with the magnetisation along $\mathbf{B}_0$.

To simplify the interaction between the oscillating field and the magnetisation along $\mathbf{B}_0$ it is useful to translate from the laboratory frame of reference $x$, $y$, $z$, to a rotating frame $x'$, $y'$, $z'$, where $z = z'$ that rotates around $z$ at frequency $\omega_{rf}$. In this rotating frame $\mathbf{B}_1$ looses its time dependence and appears static, the magnetization will then

start precessing around what is called the effective field, the effective field $\mathbf{B}_{eff}$ in the rotating frame is given by

$$\mathbf{B}_{eff} = \mathbf{B}_0 + \frac{\omega_{rf}}{\gamma} + \mathbf{B}_1 \qquad (2.9)$$

However if the radio frequency pulse ($rf$) is applied at $\omega_{rf} = \omega_0$ then the contribution of the $\mathbf{B}_0$ field is removed from the rotating frame and the magnetization appears stationary (see Figure 2.3a). The magnetisation will then start to process around the only remaining field which is $\mathbf{B}_1$. Furthermore, it can now be observed that the component of $\mathbf{B}_1$ that was rotating the opposite direction to the magnetisation does not interact in the rotating frame as it will have frequency $2\omega_0$.

By implementing the correct intensity and duration of the $\mathbf{B}_1$ field it is possible to rotate the magnetisation in the $y'$-$z'$ plane by any desired amount. The angle of rotation $\theta$ in radians during a time $t$ that the $\mathbf{B}_1$ field is applied for is given by

$$\theta = \gamma B_1 t = \omega_1 t \qquad (2.10)$$

Therefore, if the $rf$ pulse is applied so that the $\mathbf{B}_1$ field lies along the direction of the $x'$ axis then by applying what is called a $90°$ or $\pi/2$ pulse, then the magnetisation will be rotated onto the $-y'$ axis (see Figure 2.3b). When the $\mathbf{B}_1$ field is turned off, the
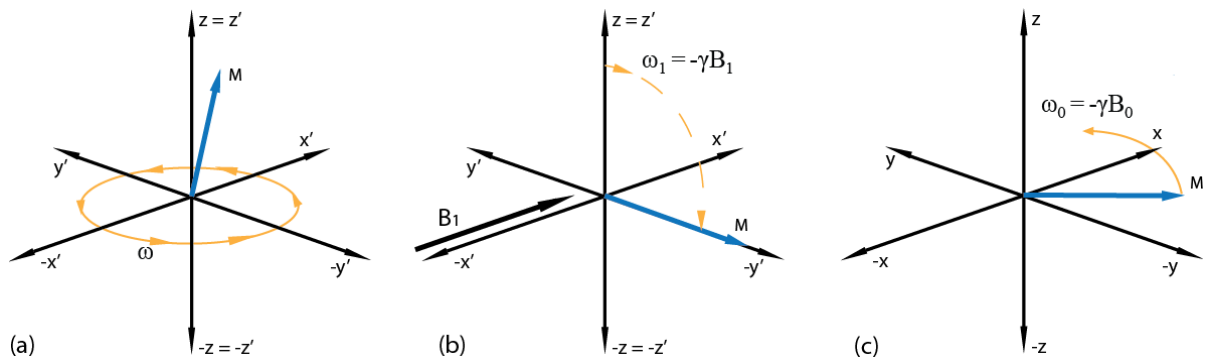


Figure 2.3: (a) When transferred to rotating frame with frequency $\omega_0$ the bulk magnetism will appear static. (b) If a second oscillating magnetic field is applied along $x'$ at frequency $\omega_0$ so that it appears stationary in the rotating frame the magnetisation will start to precess around it with frequency $\omega_1$. (c) If the second field is turned off after the magnetisation has rotated $90°$ from $z$ to lie on the $y'$ axis then the magnetisation will again start to precess around $z$ at $\omega_0$ however this time in the $x$ - $y$ plane.

rotating frame is removed and the magnetisation will again start to precess around $\mathbf{B}_0$ at $\omega_0$ in the laboratory frame, however this will now occur in the $x$-$y$ plane (see Figure 2.3c). The magnetisation will not stay there permanently but will return to equilibrium along $z$ with some finite time (see Section 2.3). This rotating magnetic moment in the $x$-$y$ plane produces a circulating magnetic field, and this induces a current in an appropriately positioned receiver coil. This oscillating current is called the free induction decay (FID) or the NMR signal.

## 2.3 Behaviour of the Bulk Magnetism Over Time

When a system of spins or a sample is placed in a static magnetic field it does not instantaneously have a bulk magnetisation, the act of placing it in an external magnetic field perturbs the energy levels of the system from a state of equilibrium and it takes some time before the system relaxes back into a different state of equilibrium. Likewise, after the magnetisation has been rotated to the $x$-$y$ plane it does not remain there indefinitely. The act of applying an $rf$ pulse has allowed the system to absorb enough energy to move to an unstable non-equilibrium state, and after the $rf$ pulse is turned off, the bulk magnetisation will start to relax back to the initial state of equilibrium along $\mathbf{B}_0$. This process of relaxation to equilibrium along $\mathbf{B}_0$ is called longitudinal relaxation or spin-lattice relaxation and is characterised by the time constant $T_1$. It is called spin-lattice relaxation as this phenomenon is stimulated by vibrations in the lattice, any energy absorbed by the lattice either through placing it in an external magnetic field or subjecting it to an $rf$ pulse will raise the energy of the system, the energy will then be dissipated throughout the lattice by an increase in amplitude of the vibrations, through which the sample will then relax back to equilibrium. In order to do this there must be an exchange of energy from the spins that were excited and the rest of the sample. This re-establishment of the magnetisation along $\mathbf{B}_0$ is best described as an exponential function and is dependant on the time constant $T_1$; $T_1$ is seen to be the time it takes for 63% of the full magnetisation to relax back along $z$.

There is a second process of relaxation that also affects the spin system. This is the transverse or spin-spin relaxation and determines how quickly the magnetisation

13

in the $x$-$y$ plane decays, and this process is characterised by time constant $T_2$. This de-phasing of the individual spins that constitute the macroscopic moment is manifest by each spin experiencing a slightly different magnetic field and thus precessing at slightly different Larmor frequencies, so after a certain amount of time they have lost all synchrony with each other and the net magnetic moment in the $x$-$y$ plane is lost.

The definitions of $T_1$ and $T_2$ lead to the phenomenological Bloch equations, which describe the build up and decay of the magnetism in relation to the motion of the magnetisation in the magnetic field. In other words, these equations describe the macroscopic behaviour of the ensemble of spins over time, and this time dependence of the magnetisation for the transverse and longitudinal components are given by

$$\frac{dM_x}{dt} = -\frac{M_x}{T_2}, \quad \frac{dM_y}{dt} = -\frac{M_y}{T_2}, \quad \frac{dM_z}{dt} = -\frac{M_z - M_0}{T_1} \tag{2.11}$$

By combining Equation 2.11 with the equation of motion defined in Equation 2.7 a new expression for the equation of motion that describes the behaviour of the magnetisation with respect to $T_1$ and $T_2$ in a magnetic field $\mathbf{B}$ is obtained

$$\frac{d\mathbf{M}}{dt} = \gamma \mathbf{M} \times \mathbf{B} - \frac{M_x + M_y}{T_2} - \frac{M_z - M_0}{T_1} \tag{2.12}$$

It is helpful to break up Equation 2.12 into its individual components

$$\frac{dM_x}{dt} = \gamma(M_y B_z - M_z B_y) - \frac{M_x}{T_2} \tag{2.13}$$

$$\frac{dM_y}{dt} = \gamma(M_z B_x - M_x B_z) - \frac{M_y}{T_2} \tag{2.14}$$

$$\frac{dM_z}{dt} = \gamma(M_x B_y - M_y B_x) - \frac{M_z - M_0}{T_1} \tag{2.15}$$

If an $rf$ pulse is applied along the $x´$ direction of $\omega_1 = \gamma \mathbf{B}_1$ then in a rotating frame of frequency $\omega$, relative to the laboratory frame, there will be an effective static field of

$$\mathbf{B}_{eff} = \mathbf{B}_0 + \frac{\omega}{\gamma} + \mathbf{B}_1 = \frac{(\omega - \omega_0) - \omega_1}{\gamma} \tag{2.16}$$

where $\mathbf{B}_0 = -\omega_0/\gamma$. As there is no component $B_y$, then under these conditions the

equations of motion in the rotating frame become

$$\frac{dM_x}{dt} = (\omega - \omega_0)M_y - \frac{M_x}{T_2} \tag{2.17}$$

$$\frac{dM_y}{dt} = -(\omega - \omega_0)M_x - \omega_1 M_z - \frac{M_y}{T_2} \tag{2.18}$$

$$\frac{dM_z}{dt} = \omega_1 M_y - \frac{M_z - M_0}{T_1} \tag{2.19}$$

If $\omega_1 = \omega = \omega_0$ then the contribution of $\mathbf{B}_0$ is removed form the effective field then the only residual component will be $\mathbf{B}_1$; similarly if the application of $\mathbf{B}_1$ is very short compared to $T_1$ or $T_2$ then the system of equations simplify further and in terms of $\mathbf{B}_1$ become

$$\frac{dM_x}{dt} = 0 \tag{2.20}$$

$$\frac{dM_y}{dt} = \gamma B_1 M_z \tag{2.21}$$

$$\frac{dM_z}{dt} = -\gamma B_1 M_y \tag{2.22}$$

For the application of an *rf* pulse along the $x$ axis of $\omega_1 = \gamma B_1$ the above equations will have the following solutions

$$M_x = 0 \tag{2.23}$$

$$M_y = M_0 sin(\omega_1 t) \tag{2.24}$$

$$M_z = M_0 cos(\omega_1 t) \tag{2.25}$$

It can be seen that by applying a pulse along the $x\,´$ axis, it is possible to rotate the magnetisation through any angle $\theta$ in the $y\,´$- $z\,´$ plane, where the angle of rotation is determined by $\omega_1 t$. This process of rotating the magnetisation away from $z$ is known as nutation. Similarly, if the pulse was along the $y\,´$ axis it is possible to rotate the magnetisation anywhere in the $x\,´$- $z\,´$ plane. Indeed, it is possible through combinations of pulses to get the magnetisation to point in any direction.

After the pulse along the $x\,´$ axis and with the magnetisation lying along $y\,´$, if the $\mathbf{B}_1$ field is turned off, at time $t = 0$ the magnetisation is in a state $M_x = 0$, $M_y = M_0 sin(\theta)$, $M_z = M_0 cos(\theta)$ the magnetisation is then free to precess around $\mathbf{B}_0$ again,

however, this time in the $x$ - $y$ plane at frequency $\omega_0$. The equations of motion in this case are reduced to

$$\frac{dM_z}{dt} = -\frac{M_z - M_0}{T_1} \tag{2.26}$$

$$\frac{dM_x}{dt} = \gamma M_y B_z - \frac{M_x}{T_2} \tag{2.27}$$

$$\frac{dM_y}{dt} = \gamma M_x B_z - \frac{M_y}{T_2} \tag{2.28}$$

as there is no contribution from any transverse magnetic field components $\mathbf{B}_x$ and $\mathbf{B}_y$ and the only external field contribution is $\mathbf{B}_z$. Therefore, for free precession in the static magnetic field the solutions to the equations of motion are given by

$$M_x = M_0 cos(\omega_0 t) exp^{(-\frac{t}{T_2})} \tag{2.29}$$

$$M_y = M_0 sin(\omega_0 t) exp^{(-\frac{t}{T_2})} \tag{2.30}$$

$$M_z = M_0(1 - exp^{(-\frac{t}{T_1})}) \tag{2.31}$$

It can be observed from these solutions to the Bloch equations that the magnetic moment rotating at the Larmor frequency $\omega_0$, decays in the $x$-$y$ plane exponentially with time constant $T_2$ (see Figure 2.4c) giving rise to the detectable decaying signal or FID (see Figure 2.4b). Simultaneously the magnetisation builds up again along $z$, again exponentially with constant $T_1$ (see Figure 2.4a), this later case is also the same for when the system of spins is placed in the magnetic field

The length of $T_1$ and $T_2$ varies from sample to sample and with the nucleus involved. In liquids both $T_1$ and $T_2$ are on the order of seconds with $T_1$ always being longer. However, in most solids $T_2$ is generally very short in the order of milliseconds and can be as short as microseconds, and $T_1$ can vary greatly from milliseconds to days. Both of these times are very important to NMR experiments. $T_1$ places a restriction on how quickly the experiment can be repeated, and this dictates how much signal-to-noise can be achieved in any particular measurement. The number of acquisitions is crucial in the achievement of good signal-to-noise, as it is proportional to the square root of the number of acquisitions. $T_2$, on the other hand, determines how long the detectable
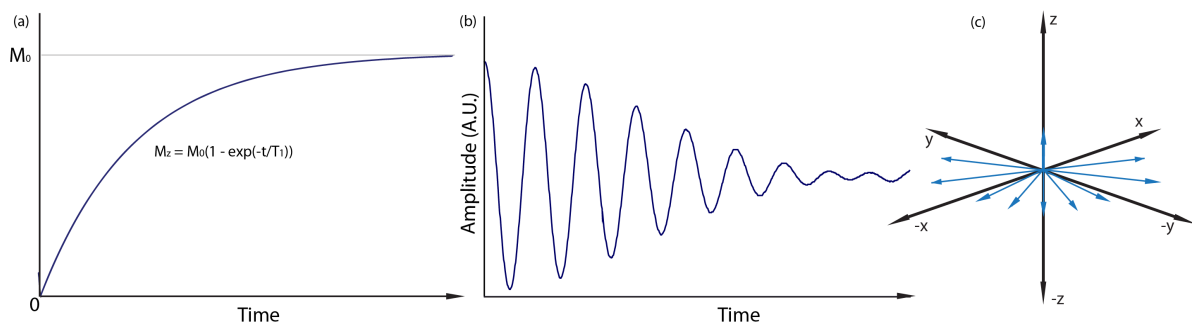
Figure 2.4: (a) When the sample is placed in the static field or after a pulse the magnetisation relaxes exponentially along the $z$ axis with time constant $T_1$. (b) The amplitude of the rotating magnetic moment (detectable signal) decays with time constant $T_2$. (c) The decay of the transverse magnetisation is due to the spins that make up the magnetic moment losing phase coherence, due to each spin seeing a slightly different magnetic field and therefore having slightly different precession frequencies.

signal lasts; as the magnetisation is decaying in the $x$-$y$ plane, then so does the intensity of signal that is induced in the coil. In practice the measured time constant for the transverse decay is actually shorter than $T_2$, and this is called $T_{2^*}$. This is due to inhomogeneities in the magnetic field causing the magnetisation to decay much faster than just through the conventional spin-spin relaxation process, in this case $T_{2^*}$ is given by

$$\frac{1}{T_{2^*}} = \frac{1}{T_2} + \frac{1}{T_{2'}} \qquad (2.32)$$

where $T_2$ is the dephasing due to spin-spin interactions and $T_{2'}$ is the contribution caused by magnetic field inhomogeneities.

## 2.4 The Quantum Mechanical Approach

While a classical approach can adequately describe the basics of the NMR experiment and the evolution of the macroscopic magnetism over time, an understanding of what is taking place at the microscopic level within the sample is also necessary. Therefore it is important to understand how the different nuclear spins evolve over periods of time as a consequence of the quantum nature of the NMR interactions influencing each spin system. Hence a quantum mechanical approach is required.

In a quantum mechanical system the energy levels of a wave function $\psi$ are given

by the time dependent Schrödinger equation

$$i\hbar\frac{\partial\psi}{\partial t} = H\psi \tag{2.33}$$

where $H$ is the Hamiltonian or energy operator for the system. If the system is considered to be closed; i.e. if all energy is conserved and it is time invariant, then the description can be simplified by using the time independent version of Equation 2.33

$$H\psi = E\psi \tag{2.34}$$

Following from this, the Hamiltonian for an isolated nuclear spin $\mathbf{I}$ in a static magnetic field along $\mathbf{B}_0$ is given by

$$H = -\gamma\hbar\mathbf{I}\mathbf{B}_0 \tag{2.35}$$

This is known as the Zeeman Hamiltonian; if $\mathbf{B}_0$ is defined to be along the $z$ axis then the Zeeman Hamiltonian becomes

$$H_Z = -\gamma\hbar I_z \ B_0 \tag{2.36}$$

The allowed values of $I_z$ are given by the quantum number $m$ and have $2I+1$ states that take integer steps between $+I$ and $-I$. In the absence of an applied field these states are degenerate, however when a static magnetic field is applied then the degeneracy of the states is lifted. This phenomenon is called the Zeeman effect (see Figure 2.5) and it causes each of the $2I+1$ levels to have a slightly different energy. In the case of a spin $I = \frac{1}{2}$ nucleus the two allowed states have values of $m$ that are $\pm \frac{1}{2}$.

The energy of the different levels can be found using the wave functions describing the different states of the spin system. $I_z$ has eigenfunctions $|I, m>$ (in Dirac notation $|I, m> = \psi_{I,m}$ and $< I, m| = \psi_{I,m}^*$) where $I$ is the nuclear spin number. As $H_Z$ is proportional to $I_z$ then $|I, m>$ are also eigenfunctions of $H_Z$, then by operating on the wave functions with $H_Z$ the following is obtained

$$H_Z|I, m> = -\gamma\hbar B_0 I_z|I, m> = E|I, m> \tag{2.37}$$
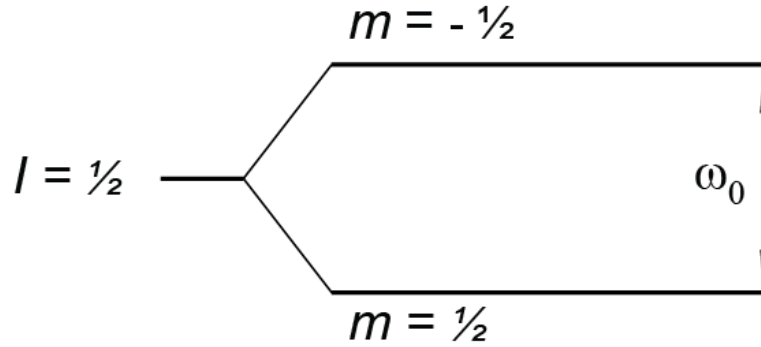
Figure 2.5: When placed into a static magnetic field the normally degenerate nuclear ground state will split into $2I+1$ energy levels, with the separation between them being equal to the Larmor frequency $\omega_0$

$I_z$ has eigenvalues $m$ which can take the values $\pm \frac{1}{2}$ then

$$E = -\gamma \hbar B_0 m, \;\; \text{so} \;\; E_1 = -\gamma \hbar B_0 \left( \frac{1}{2} \right) \;\; \text{and} \;\; E_2 = -\gamma \hbar B_0 \left( -\frac{1}{2} \right) \tag{2.38}$$

and the energy $\Delta E$ of the transition between the two states is given by

$$\Delta E = E_2 - E_1 = \gamma \hbar B_0 \tag{2.39}$$

As $B_0 = -\omega_0 / \gamma$ then we can see that the expression in Equation 2.39 matches the expression in Equation 2.8, and it can be seen that the energy separation of the two levels is equal to the Larmor frequency. This constitutes the fundamental resonance condition and it describes the ability of a system to absorb energy and make the transitions between energy levels. This is the fundamental premise of the magnetic resonance phenomenon.

While it is relatively simple to consider a simple isolated nucleus, it is not very practical. It is more realistic to consider a larger ensemble of spins of some arbitrary spin $I = \frac{1}{2}$ nucleus. To find the magnetisation along $z$ for this ensemble of spins we need to calculate the expectation value of $\mu_z$. For the ensemble average the expectation value of an operator is given by

$$< A > = < \Psi | A | \Psi > \tag{2.40}$$

Therefore the expectation value of $\mu_z$ for the entire system is given by

$$< \mu_z >= \gamma\hbar < \Psi|I_z|\Psi >= \gamma\hbar \sum_\Psi P_\Psi < \Psi|I_z|\Psi > \qquad (2.41)$$

$P_\Psi$ is the population of the various states, which is given by a Boltzmann distribution

$$P_\Psi = \frac{N_{\Psi i}}{N} = \frac{exp\left(\frac{-E_{\Psi i}}{kT}\right)}{\sum_{\Psi j} exp\left(\frac{-E_{\Psi j}}{kT}\right)} \qquad (2.42)$$

where $E_{\Psi i}$ is the energy of the state $\Psi i$, and $N_{\Psi i}$ is the number of states. For a spin $I = \frac{1}{2}$ nuclei and using Equation 2.41 the expectation value of the $\mu_z$ magnetisation is given by the population difference of the two states

$$< \mu_z >= \gamma\hbar\frac{1}{2}\left(P_{1/2} - P_{-1/2}\right) \qquad (2.43)$$

which is equivalent to Equation 2.3. Similarly if an $rf$ pulse of $B_1\cos(\omega_1 t)$ is applied along $x$ then it can be found that the expectation values of $\mu_y$ and $\mu_x$ will be

$$< \mu_y >= \gamma\hbar\frac{1}{2}\left(P_{1/2} - P_{-1/2}\right) sin(\omega_1 t) \qquad (2.44)$$

$$< \mu_x >= 0 \qquad (2.45)$$

Similarly, this result is equivalent to the expressions given in Equations 2.24 and 2.23 derived by the classical approach. Hence, the system of spins has been perturbed from equilibrium by the application of the $rf$ pulse, and the resulting magnetisation after the $rf$ pulse is turned off, will behave according to Equations 2.29, 2.30 and 2.31.

However the quantum mechanical description does not describe a nutation of the magnetic moment with the application of an $rf$ pulse, but rather it describes a change in the populations of the spin states. Keeping track of the populations of spin states and how they evolve through the application of rf pulses can be achieved by using the density operator approach, however due to space limitations only the main outcome will be considered here, and this is based around the concept of coherences.

Coherences are associated with the generation of transverse magnetisation and are

a quantum mechanical description of the system rather than a diagrammatic magnetic vector representation. Coherences arise from the mixing of the Zeeman spin states thus creating a superposition of states. Changes in coherence order are a change in energy of magnetic quantum number $m$ through either the absorption or emission of one quantum of energy.

The simplest description is of a single spin system, in an external magnetic field the system can be in either the state $|\alpha>$ or $|\beta>$ and the system has no coherence. If energy is introduced to the system by the application of an $rf$ pulse, the system will then be transformed to a mixture of states $|\alpha, \beta>$ creating a change in coherence order of $\pm 1$. Under these conditions there is now considered to be coherence between the spin states. If the system is expanded to consider many spins, at equilibrium slightly more spins are in the $|\alpha>$ state than the $|\beta>$ state and align with the field giving a net polarisation. After an $rf$ pulse the populations will then be equalised and a mixed state $|\alpha, \beta>$ will be created, however for there to be a net polarisation the superposition of states must be partially aligned and in phase with one another, hence the system is said to be coherent. Again the system has undergone a change of coherence order $\pm 1$, both orders of coherence being created simultaneously. The -1 quantum coherence corresponds to the magnetisation vector from the classical approach and the +1 coherence constitutes a mirror image, the -1 coherence is the source of the signal in the NMR experiment.

In reality, the application of a pulse in a many spin system creates many orders of coherence, however as it is only the -1 coherence that is ever directly detected these are not part of the NMR signal. Despite this it is possible to select and deliberately excite higher orders of coherence such as double quantum ($\pm 2$) or triple quantum ($\pm 3$) coherences through the use of phase cycling the pulses (see Chapter 3.4)and these coherences are then reconverted back to a -1 coherence for detection, with any undesirable coherences being filtered out by phase cycling the reconversion pulses.

## 2.5 Internal Interactions

While the Zeeman interaction is the dominant interaction in NMR caused by external magnetic fields, there are several internal interactions that influence the NMR experiment. Indeed these interactions are what makes NMR useful as an analytical technique rather than just the observation of an interesting phenomenon. These interactions are the chemical shielding (or chemical shift), the dipolar coupling interaction, the scalar (or J-coupling), the quadrupole coupling (for $I > \frac{1}{2}$), the Knight shift and the paramagnetic shift. Thus the total Hamiltonian $H$ for the system will be made up of

$$H_{total} = H_Z + H_{rf} + H_{Int} \tag{2.46}$$

where $H_Z$ is the Zeeman Hamiltonian, $H_{rf}$ is the contribution of the $\mathbf{B}_1$ field and $H_{int}$ is the Hamiltonian due to internal interactions. $H_{int}$ for the system will be made up of all the contributions from separate the internal interactions

$$H_{Int} = H_{CS} + H_D + H_{QC} + H_J + H_K + H_P \tag{2.47}$$

For the purpose of this thesis, the Knight shift and the paramagnetic effect will be omitted as they are only relevant for conducting materials and materials with unpaired electrons, respectively, which are not relevant to the subject mater of this study.

For simplicity it is easier to deal with each internal interaction separately the Hamiltonian for each interaction can be described in a general sense by

$$H_I = b\mathbf{I} \cdot \mathbf{A} \cdot \mathbf{S} \tag{2.48}$$

where $H_I$ is one of the component Hamiltonians from Equation 2.47. There is a different constant b for each interaction, $\mathbf{I}$ is the spin term in the interaction expressed by a vector, $\mathbf{A}$ represents the particular interaction in question and takes the form of a $2^{nd}$ rank Cartesian tensor expressed as a 3 x 3 matrix, (specifying the orientation dependence of the particular interaction) and $\mathbf{S}$ is another vector quantity and is either a magnetic field term or another spin term depending on the interaction.

Each interaction is further simplified by describing it in its own principle axis system (PAS) so that only the diagonal terms remain in the Cartesian tensor. However the principle axis system is not the same for the different interactions; for example in the chemical shift interaction it pertains to the surrounding electronic environment of the nucleus in question, and for dipolar coupling it describes the internuclear vector between the interacting nuclei. However these interactions often need to be explained in terms of the Zeeman Hamiltonian in the laboratory frame of reference or the rotating frame of reference, and as these interactions cover all possible orientations in space it is unlikely they will coincide with the laboratory frame or the rotating frame, therefore rotations of the PAS into the other frames are required.

These rotations between coordinate frames are achieved using Euler angles or an appropriate operator to transfer a static frame of reference to a rotating frame. Rotations using the Euler angles $(\alpha, \beta, \gamma)$ to transform from one frame of reference $x$, $y$, $z$ to another $X$, $Y$, $Z$ are expressed as $\mathbf{R}(\alpha, \beta, \gamma) = \mathbf{R}_z(\alpha)\,\mathbf{R}_y(\beta)\,\mathbf{R}_z(\gamma)$, this specifies a rotation around $z$ of angle $\alpha$, then a rotation around $y$ of $\beta$, and a final rotation around $z$ of $\gamma$ which can therefore translate from the frame $x$, $y$, $z$ to any general orientation $X$, $Y$, $Z$. When relating to transformations of tensors from one frame to another, the rotations $\mathbf{R}(\alpha, \beta, \gamma)$ are defined as a 3 x 3 matrix So that a rotation of the tensor $\mathbf{T}$ from $x$, $y$, $z$ to $X$, $Y$, $Z$ is described by

$$\mathbf{T}(X, Y, Z) = \mathbf{R}(\alpha, \beta, \gamma)\mathbf{T}(x, y, z)\mathbf{R}^{-1}(\alpha, \beta, \gamma) \tag{2.49}$$

A rotation about $z$ from a static frame of reference for an operator F to a rotating frame $F_{rot}$ is given by

$$F_{rot} = R(-\phi)FR(\phi) \text{ where } R = exp^{-i\phi I_z} \tag{2.50}$$

where $\phi$ is the time dependant angle and is defined as $\phi = \omega t$

## 2.5.1 The Chemical Shift

The single interaction that makes NMR such a powerful technique is the chemical shift. Not only does each NMR active isotope have a different resonant frequency, but so do the same isotopes if they are in different electronic (or chemical) environments. This is because the electrons that are surrounding the nucleus also interact with the static field $\mathbf{B}_0$. When the electrons surrounding a nucleus are influenced by an external magnetic field they circulate around the nucleus creating current loops and therefore a magnetic field, this magnetic field acts in such a way that it shields the nucleus from the external magnetic field. This has the ability to change ever so slightly the $\mathbf{B}_0$ field seen at the nucleus and hence a shift in frequency from $\omega_0$. The induced field is very much dependant on the electron density about each position and is therefore related to the bonds between atoms, therefore the same isotopes with different electronic configurations will have different processional frequencies. It is this change in frequency that is termed the chemical shift.

Equation 2.48 when expressed in terms of the chemical shielding becomes,

$$H_{CS} = \gamma \mathbf{I} \cdot \boldsymbol{\sigma} \cdot \mathbf{B}_0 \tag{2.51}$$

Where $\boldsymbol{\sigma}$ is a 2nd rank tensor in the principle axis frame

$$\boldsymbol{\sigma}^P = \begin{pmatrix} \sigma_{xx}^P & 0 & 0 \\ 0 & \sigma_{yy}^P & 0 \\ 0 & 0 & \sigma_{zz}^P \end{pmatrix}.$$

The principle values of the chemical shielding tensor are known as the isotropic value ($\sigma_{iso}$), the anisotropy ($\Delta_\sigma$) and the asymmetry ($\eta$) and are defined as

$$\sigma_{iso} = \frac{1}{3}(\sigma_{xx}^P + \sigma_{yy}^P + \sigma_{zz}^P)$$

$$\Delta_\sigma = \sigma_{zz}^P - \sigma_{iso}$$

$$\eta = \frac{\sigma_{xx}^P - \sigma_{yy}^P}{\Delta_\sigma} \tag{2.52}$$

However most of the orientations of the principle axis will not coincide with the required frame of reference, thus a rotation from the principle axis to the lab frame is required. This is achieved by using the rotation matrix specifying the rotations by the Euler angles in Equation 2.49.

The induced field at the nucleus taking into account effects from the shielding ($\sigma$) and $\mathbf{B}_0$ is then given by

$$\mathbf{B}^{ind} = \boldsymbol{\sigma}^{lab} \cdot \mathbf{B}_0 = \begin{pmatrix} \sigma_{xx} & \sigma_{xy} & \sigma_{xz} \\ \sigma_{yx} & \sigma_{yy} & \sigma_{yz} \\ \sigma_{zx} & \sigma_{zy} & \sigma_{zz} \end{pmatrix} \cdot \begin{pmatrix} 0 \\ 0 \\ \mathbf{B}_0 \end{pmatrix} = \begin{pmatrix} \sigma_{xz}\mathbf{B}_0 \\ \sigma_{yz}\mathbf{B}_0 \\ \sigma_{zz}\mathbf{B}_0 \end{pmatrix} \tag{2.53}$$

The terms $\sigma_{xz}$ and $\sigma_{yz}$ only make second order contributions and can be neglected and it is only the component $\sigma_{zz}$ that aligns with $\mathbf{B}_0$ that is of interest. Therefore the Hamiltonian that represents the chemical shielding becomes.

$$H_{CS} = \gamma I_z \cdot \sigma_{zz} \cdot B_0 \tag{2.54}$$

The contribution to the observed frequency for the NMR signal from the chemical shielding $\omega_{CS}$ is then

$$\omega_{CS} = \gamma \sigma_{zz} B_0 = -\omega_0 \sigma_{lab} \tag{2.55}$$

In order to find $\sigma_{zz}$ we need to consider the principle values (see Equation 2.52) of the shielding tensor with respect to the orientation of the $\mathbf{B}_0$ field in the laboratory frame. This is done by expressing the orientation of the principle axis with respect to the laboratory frame by the polar coordinates $\theta$ and $\phi$, the expression for $\sigma_{zz}$ is then

$$\sigma_{zz} = \sigma_{iso} + \frac{\Delta_\sigma}{2} + [(3cos^2\theta - 1) + \eta(sin^2\theta cos2\phi)] \tag{2.56}$$

By combining the expression for $\sigma_{zz}$ with Equation 2.55 the full expression for how the chemical shielding influences the observed frequency is obtained

$$\omega_{CS} = -\omega_0 \sigma_{iso} - \frac{1}{2}\omega_0 \Delta_\sigma + [(3cos^2\theta - 1) + \eta(sin^2\theta cos2\phi)] \tag{2.57}$$

25

These three parameters that make up the above term are known as the isotropic shift the anisotropy and the asymmetry and relate to the symmetry of the local environment, this will then influence the chemical shielding for each orientation to the main field. However in liquids rapid molecular motion tends to average out the values and all that is left is the isotropic component. Conversely in solids, as all molecules are fixed all orientations are therefore possible, and this is especially true in polycrystalline materials. The resulting spectrum will consist of a broad peak built up of many different resonances that are given by these orientations (see Figure 2.6). This phenomenon is called inhomogeneous broadening and the shape of the peak will reflect any anisotropy or asymmetry at that particular atomic position. However it will be seen in Chapter 3.2 that rapid molecular motion can be simulated in a solid.
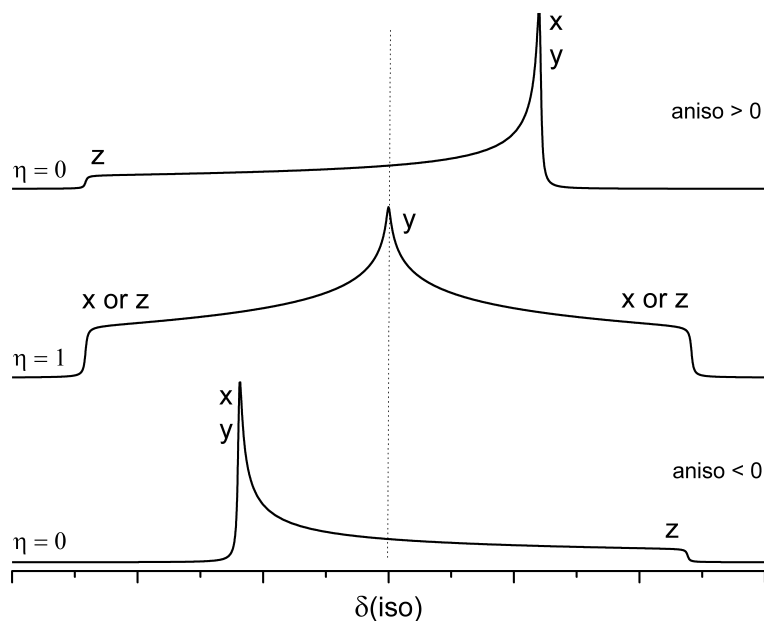


Figure 2.6: Hypothetical powder patterns for a single molecular site spin $I = \frac{1}{2}$ nucleus showing the anisotropy due to different orientations of the crystallites, the sharp labelled features coincide with the principle values of the shielding tensor, the isotropic chemical shift is marked by the dotted line.

The value for chemical shielding is normalised, as this makes comparisons between different magnetic field strengths possible. Absolute frequencies are not measured in an NMR experiment, rather they are quoted with respect to a reference frequency given by a standard compound, and the frequencies measured in the experiment are given with respect to the changes in frequency from that reference. This is called the

chemical shift $\delta$ and has units of ppm (parts per million). The chemical shift is defined as

$$\delta = \frac{\nu_{sample} - \nu_{ref}}{\nu_{ref}} = \frac{\sigma_{ref} - \sigma_{sample}}{1 - \sigma_{ref}} \qquad (2.58)$$

This ability to measure accurately the subtle changes in frequencies is fundamental to NMR, and the major contributions to the chemical shift come from the low lying excited electronic states. Hence, it can be seen that the chemical shift range for different nuclei can vary significantly. It has been established that heavier atoms tend to have a larger chemical shift ranges (on the order of thousands of ppm), whereas lighter atoms might have much smaller shift ranges in the tens of ppm. However, there can also be a contribution from directly bonded electronegative atoms, and the chemical shift can be further influenced by the next nearest neighbours.

### 2.5.2 The Dipolar Interaction

The Dipolar interaction arises from direct dipole-dipole contact between nuclei. As each nuclear spin possess a magnetic moment this has an associated magnetic field with it that propagates through space and interacts with the magnetic fields of the surrounding nuclei. This is a mutual interaction as the magnetic field of a spin interacts with the field of a second spin, the field of the second spin will also interact with the field generated by the first spin. This interaction is generally broken into two different categories; like spins that interact (homonuclear) and unlike spins that interact (heteronuclear). The magnitude of the heteronulcear and homonuclear dipolar couplings are both dependant on the inverse cube of the distance between the nuclei and the orientation of the resultant vector due to the nuclei involved. Both of these cases give slightly different outcomes and will be discussed later but now the interaction will be dealt with in a general sense.

The dipole Hamiltonian can be expressed in the form of equation as

$$H_D = -2\mathbf{I} \cdot \mathbf{D} \cdot \mathbf{S} \qquad (2.59)$$

where $\mathbf{I}$ is spin term one, $\mathbf{S}$ is spin term two and $\mathbf{D}$ is the dipole coupling tensor which

has principle values -d/2, -d/2 and d, where d is defined as

$$d = \hbar \left( \frac{\mu_0}{4\pi} \right) \frac{1}{r^3} \gamma_I \gamma_s \tag{2.60}$$

The tensor $\mathbf{D}$ describes the interaction between the spins $\mathbf{I}$ and $\mathbf{S}$ with respect to each other and the distance between them. However the full solution to this is rather lengthy so a slightly different approach will be invoked here. Fortunately it can be approached from a more classical point of view.

Classically, the energy of two interacting magnetic dipoles is given by

$$E_d = \frac{\mu_0}{4\pi} \left( \frac{\boldsymbol{\mu}_1 . \boldsymbol{\mu}_2}{r^3} - 3 \frac{(\boldsymbol{\mu}_1 . \mathbf{r})(\boldsymbol{\mu}_2 . \mathbf{r})}{r^5} \right) \tag{2.61}$$

By substituting in the quantum mechanical operator (see Equation 2.1) for the nuclear magnetic moment into Equation 2.61 an expression for the Hamiltonian due to dipole-dipole interactions is obtained

$$H_D = \frac{\mu_0}{4\pi} \frac{\gamma_I \gamma_S}{r^3} \hbar \left( \mathbf{I}_I . \mathbf{I}_S \frac{(\mathbf{I}_I . \mathbf{r})(\mathbf{I}_S . \mathbf{r})}{r^2} \right) \tag{2.62}$$

As the interaction between the spins depends on the internuclear vector between the spins, it is common to express the dipole Hamiltonian in spherical polar coordinates

$$H_D = \frac{\mu_0}{4\pi} \frac{\gamma_I \gamma_S}{r^3} \hbar (A + B + C + D + E + F) \tag{2.63}$$

This leads to a complicated expression for the interaction, and terms A-F (often referred to as the dipolar alphabet) are

$$A = I_z S_z (3cos^2\theta - 1) \tag{2.64}$$

$$B = -\frac{1}{4} [I_+ S_- + I_- S_+](3cos^2\theta - 1) \tag{2.65}$$

$$C = \frac{3}{2} [I_z S_+ + I_+ S_z] sin\theta cos\theta exp^{(-i\phi)} \tag{2.66}$$

$$D = \frac{3}{2} [I_z S_- + I_- S_z] sin\theta cos\theta exp^{(+i\phi)} \tag{2.67}$$

$$E = \frac{3}{4}[I_+S_+]sin^2\theta exp^{(-2i\phi)} \tag{2.68}$$

$$F = \frac{3}{4}[I_-S_-]sin^2\theta exp^{(+2i\phi)} \tag{2.69}$$

With $I_+$ and $I_-$ being the raising and lowering operators $I_+ = I_x + iI_y$ and $I_- = I_x - iI_y$ likewise for $S_+$ and $S_-$. It is now convenient to consider the Hamiltonian for the dipole-dipole interactions separately for homonuclear and heteronuclear coupling, as there are slight differences in the physical effects.

In the case of homonuclear coupling it is necessary to transfer the Hamiltonian to the rotating frame of reference with respect to the observed spin. As both spins are of the same kind this has to act on both. By using the rotation operator defined in Equation 2.50 that describes a rotation about $z$ for the spin system, then

$$H_D = -\frac{\mu_0}{4\pi}\frac{\gamma_I\gamma_S}{r^3}\hbar[(A+B) + R_z(-\phi)(C+D+E+F)R_z(\phi)] \tag{2.70}$$

When transferred to the rotating frame A and B remain unaffected, however the expressions C-F obtain a time dependence at frequencies $\omega$ and $2\omega$ and can for these purposes be discarded. The raising and lowering operators are redefined in terms of the Cartesian spin operators. Therefore only the time independent or secular part remains and the Hamiltonian for homonuclear dipole coupling becomes

$$H_D = -\frac{\mu_0}{4\pi}\frac{\gamma_I\gamma_S}{r^3}\hbar\left[I_zS_z - \frac{1}{2}(I_xS_x + I_yS_y)\right](3cos^2\theta - 1) \tag{2.71}$$

However if the same process is applied in the case of hetronuclear coupling, when transformed to the rotating frame, as the spins are different, it only acts on the observed spin I and the Hamiltonian becomes

$$H_D = -\frac{\mu_0}{4\pi}\frac{\gamma_I\gamma_S}{r^3}\hbar[A + R_z(-\phi)(B+C+D+E+F)R_z(\phi)] \tag{2.72}$$

It can now be seen that the B term has also become time dependant, and when the time dependencies are removed the heteronuclear dipole Hamiltonian reduces to

$$H_D = -\frac{\mu_0}{4\pi}\frac{\gamma_I\gamma_S}{r^3}\hbar I_zS_z(3cos^2\theta - 1) \tag{2.73}$$

The implications from the two different types of coupling manifest themselves in their dependence on the B term, while the A term remains integral in both the homonuclear and heteronuclear cases. The A term represents an energy shift of the spin levels while the B term is often termed a flip-flop term. This flip-flop process is a continuous exchange of energy between the different spin states of the coupled spins, implying that the different spins can spontaneously change from $-\frac{1}{2}$ to $+\frac{1}{2}$ in a two spin system. However this only happens when energy in the system is conserved; if the nuclear species are different then $\gamma$ is different and energy is no longer conserved, hence the removal of this effect in the heteronuclear case. This effect does not change the longitudinal magnetisation as this process is continuous, however it does affect the observed signal, as what is observed during this process is a large range of transition frequencies which translates as a broadened spectrum tending to a Gaussian line shape (see Figure 2.7a). This depends critically on the strength of the dipole-dipole interaction and this process is called homogeneous broadening.

In the case of heteronuclear coupled spins the flip-flop term is not present and there is no mixing of the Zeeman states, and therefore the cause of homogeneous broadening is not present. However there is a shift in the energy levels due to the coupling which has an angular dependence of $\pm(3\cos^2\theta - 1)$ which consequently exhibits the same features that are found in a CSA pattern, though there will also be a mirror image (see Figure 2.7b) with one feature arising from the + transitions and the other from the – transitions.

In addition, it is possible for a hetronuclear coupled spin system to contribute to homogeneous broadening if it is strongly bonded to another spin which is part of a homonuclear network. This will effect one or more of the spins in the homonuclear network and will influence the flip-flop interaction, and therefore will contribute to the homogeneous broadening of the final spectrum.

As was the case with the chemical shift anisotropy, the dipolar interaction is motionally averaged out in liquids. In polycrystalline materials the effects of dipolar coupling can cause significant resolution problems. They can be removed or reduced by magic angle spinning (see Chapter 3.2), however this is dependant on the magnitude of the interaction and it is often necessary to use special pulse sequences simultaneously to
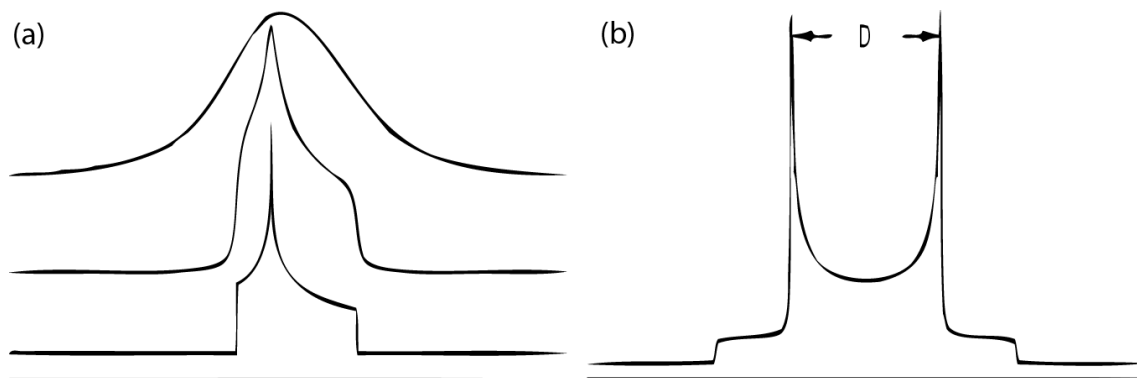
Figure 2.7: (a) Hypothetical powder pattern showing the influence of homonuclear dipole coupling on the line shape, with the bottom line shape exhibiting no dipole coupling, middle slight broadening due to coupling and top tending to a Gaussian shape due to significant homonuclear dipole-dipole coupling. (b) Simulated line shape due to hetronuclear dipole coupling, resembles a Pake doublet, essentially a CSA line shape with a mirror image due to the $\pm(3\cos^2\theta - 1)$ contribution to the transition levels, the splitting of the horns is equal to the dipole coupling constant

suppress the interaction or irradiate with $rf$ during signal acquisition the spins that are not being observed to uncouple them from the spin system under investigation. In many cases it is actually desirable to probe dipole couplings through the use of special pulse experiments, as the dipole-dipole interaction is a function of distance; this can give valuable structural information as to what chemical positions are spaciously proximate to others.

### 2.5.3 Quadrupole Coupling

The large majority of nuclei that are potentially observable in NMR experiments have a nuclear spin of $I > \frac{1}{2}$, these are known as quadrupolar nuclei. Not only do they have a magnetic dipole moment, but they also have a nuclear electric quadrupole moment, which arises from a non-spherical charge distribution at the nucleus. The quadrupole moment will interact with any electric field gradients produced by surrounding electrons. This non-magnetic interaction is termed quadrupole coupling and the strength of the interaction depends on both the strength of the electric field gradient and the size of the quadrupole moment. Hence the strength of the interaction can vary widely depending on the nucleus involved and the surrounding environment. For example, a quadrupolar nucleus possessing cubic site symmetry will experience an electric field gra-

dient effectively reduced to zero and thus exhibit a zero quadrupole interaction, while other positions possessing more general site symmetry can experience quadrupole interactions up to many MHz in magnitude. The nuclear quadrupole moment eQ, is the product of the charge of the proton e and the quadrupole moment Q, and is a constant for each specific nuclear species and is not influenced by the chemical environment.

The nuclear electric quadrupole moment is fixed within the nucleus and does not interact directly with the static magnetic field $\mathbf{B}_0$, it can still be quantized with respect to $\mathbf{B}_0$, due to the fact that the fixed magnetic moment will tend to align with the field. In contrast the electric field gradient is spatially fixed at a specific orientation within the molecular frame and since it is a purely electronic interaction there is no direct interaction with the magnetic field $\mathbf{B}_0$. However, the electric field gradient at the nucleus does interact with the magnetic moment of the nucleus, the result of this is to perturb the energy levels of the Zeeman interaction (see Figure 2.8) so that the transition frequency between the split levels is no longer equal. For convenience the following discussion will focus on $\frac{1}{2}$ integer nuclear spins only.
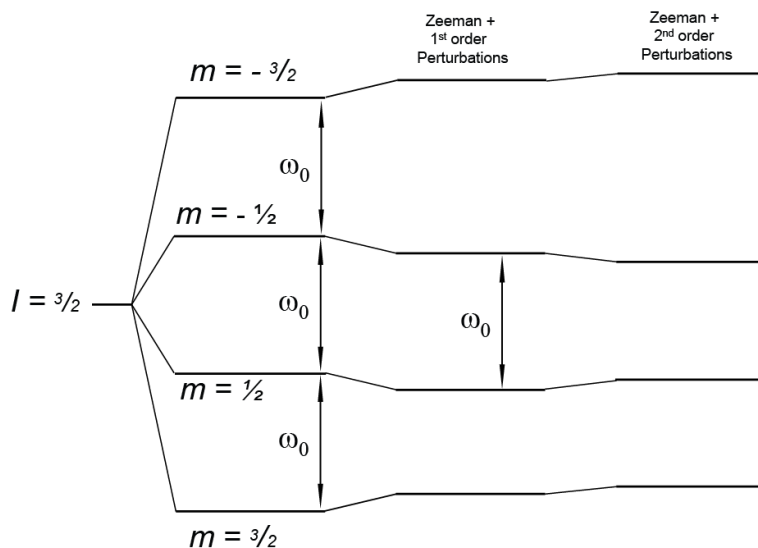


Figure 2.8: Energy level diagram for a spin $I = \frac{3}{2}$ nucleus in a magnetic field, under Zeeman splitting all levels are split by an equal amount, due to quadrupole coupling first order perturbations shift the levels $|+m>$ and $|-m>$ by an equal amount and there is no change to the $\frac{1}{2}$ - $-\frac{1}{2}$ transition. However if the quadrupole interaction is large enough second order perturbations affects the separation of all transition levels.

.

As with the other interactions the Hamiltonian describing the quadrupole interaction can be given by Equation 2.48 and takes the form

$$H_{QC} = \frac{eQ}{2I(2I-1)\hbar}\mathbf{I}\cdot\mathbf{V}\cdot\mathbf{I} \tag{2.74}$$

where $I$ is the nuclear spin number and $\mathbf{V}$ is a second rank Cartesian tensor that describes the electric field gradient at the nucleus in its principle axis frame. The principle axis frame is chosen so that $V_{xz} = V_{yz} = V_{xy} = 0$, and the principle values are $|V_{zz}| \geq |V_{yy}| \geq |V_{xx}|$, eq $= V_{zz}$ and $\eta = (V_{xx}-V_{yy})/V_{zz}$. By expanding the tensor product of Equation 2.74 and writing in terms of the tensor elements in its principal axis frame the following expression is obtained

$$H_{QC} = \frac{e^2qQ}{4I(2I-1)\hbar}[3I_z^2 - I(I+1) + \frac{1}{2}\eta(I_x^2 + I_y^2)] \tag{2.75}$$

where the constant $e^2qQ/\hbar$ is known as the quadrupole coupling constant and has units rads$^{-1}$, however it is more commonly expressed in Hz as $C_Q = e^2qQ/h$

It is necessary to describe the quadrupole Hamiltonian with respect to the Zeeman interaction which is expressed in the laboratory frame, thus requiring a rotation to the laboratory axis frame using the Euler angles in Equation 2.49. To simplify this analysis it is assumed that the quadrupole interaction has cylindrical symmetry (i.e. $\eta = 0$), therefore in the laboratory frame

$$\begin{aligned} H_{QC} = \frac{e^2qQ}{4I(2I-1)\hbar}[\frac{1}{2}&(3cos^2\theta - 1)(3I_z^2 - I^2) \\ &+ \frac{3}{2}sin\theta cos\theta[I_z(I_+ + I_-) + (I_+ + I_-)I_z] \\ &+ \frac{3}{4}sin^2\theta(I_+^2 + I_y^-)] \end{aligned} \tag{2.76}$$

where $I_+$ and $I_-$ are the raising and lowering operators $I_+ = I_x + iI_y$ and $I_- = I_x - iI_y$. However Equation 2.76 shows that there are off diagonal elements in the matrix for the quadrupole Hamiltonian, which are seen as perturbations to the energy levels of the Zeeman interaction. Therefore, in order to understand these effects on the NMR spectra of quadrupole nuclei, corrections for perturbations to the Zeeman levels need

to be taken into account, however in most cases these perturbations can be truncated after second order effects.

If the quadrupole interaction is small compared to the Zeeman interaction then only first order perturbations need to be taken into account and the energy of these are given by

$$E_{QC}^{(1)} = \frac{e^2 qQ}{4I(2I-1)\hbar}(3m - I(I+1))\frac{1}{2}[(3cos^2\theta - 1) + \eta cos2\phi sin^2\theta)] \qquad (2.77)$$

then the frequency contribution for the first order perturbations are

$$\omega_{QC}^{(0)} = \frac{3e^2 qQ}{4I(2I-1)\hbar}[\frac{1}{2}(3cos^2\theta - 1) + \frac{1}{2}\eta sin^2\theta cos2\phi] \qquad (2.78)$$

It can be seen that after first order perturbations there is no frequency change to the central $\frac{1}{2}$ - $-\frac{1}{2}$ transition, however the outer satellite transitions have been shifted in frequency by $(2m - 1)\omega_0$ and now also have an angular dependence of $(3cos^2\theta - 1)$.

If however, the quadrupole interaction is sufficiently large compared to the Zeeman interaction, then higher order perturbations have to be taken into account, usually to second order. The expression for the energy corrections for second order perturbations is

$$\begin{aligned}
E_{QC}^{(2)} = &\left(\frac{e^2 qQ}{4I(2I-1)\hbar}\right)^2 \frac{m}{\omega_0} \times \left(-\frac{1}{5}(I(I+1) - 3m^2)(3 + \eta^2)\right. \\
&+ \frac{1}{28}(8I(I+1) - 12m^2 - 3)[(\eta^2 - 3)(3cos^2\theta - 1) + 6\eta sin^2\theta cos2\phi] \\
&+ \frac{1}{8}(18I(I+1) - 34m^2 - 5)\left[\frac{1}{40}(18 + \eta^2)(35cos^4\theta - 30cos^2\theta + 3)\right. \\
&\left.\left.+ \frac{3}{7}\eta sin^2\theta(7cos^2\theta - 1)cos2\phi + \frac{1}{4}\eta^2 sin^4\theta cos4\phi\right]\right) \qquad (2.79)
\end{aligned}$$

It can be see that with second order perturbations, not only is there now an energy correction to the central transition, but it has also gained an angular dependency of $(3cos^2\theta - 1)$ and $(35cos^4\theta - 30cos^2\theta + 3)$, which will broaden the spectral line of the central transition. Even though equation 2.79 is a complicated expression it is easily observed that the frequency of the coupling is proportional to the square of the first

order coupling divided by the Larmor frequency.

$$\omega_{QC}^{(2)} \sim \left| \frac{(\omega_{QC}^{1})^2}{\omega_0} \right| \tag{2.80}$$

These corrections to the energy terms for the Zeeman splitting have several implications regarding the resulting spectra of solids systems, although in liquids it is not really a problem as this interaction is largely averaged out by molecular tumbling.

If the quadrupole interaction is small then the first order energy correction to the $\frac{1}{2}$ - $-\frac{1}{2}$ transition is zero, and as this is independent of orientation the spectrum will exhibit a sharp resonance at the isotropic chemical shift (see Figure 2.9a). In addition the satellite transitions will have a frequency shift with peaks appearing at multiples of $\pm 2\omega_{QC}$ from the peak due to the central transition. As the satellite transitions possess an angular dependence, and for a site with $\eta = 0$, they will resemble a Pake pattern in a powder. Since the spectrum is made up of all the orientations of the different crystallites, those sites that have their principle axis perpendicular to the magnetic field make up the horns, and those with their principle axis parallel to the magnetic field contribute to the low intensity edges of the pattern, with all other angles making up the rest of the pattern. The overall width of the satellite spectrum will be equal to $C_Q$ and the horns will be separated by $C_Q/2$. If $\eta$ is $> 0$ then the shape of each
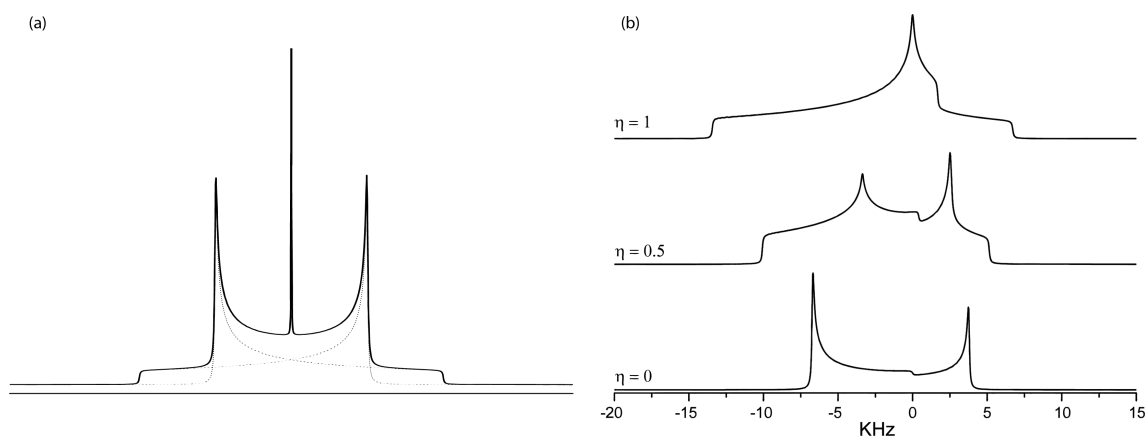


Figure 2.9: Examples of quadrupole broadened powder line shapes (a) a spin $I = \frac{3}{2}$ with first order perturbations and $\eta = 0$ the central transition gives a sharp line, while the satellite transitions give a Pake doublet reflecting the different orientations of the electric field gradient tensor. (b) The central transition broadened to second order, all sites have the same $C_Q$ and isotropic chemical shift but different $\eta$.

satellite peak will change in similar way to that for the CSA lineshape.

On the other hand, when the quadrupole interaction is sufficiently large and second order effects have to be taken into account, the broadening of the central transition can be quite severe. There will no longer be a sharp resonance at the isotropic position (see Figure 2.9b), and the shape and width of the central transition is dependant of several factors, such as $C_Q$, $\eta$ and $B_0$. The isotropic shift for the central transition is also affected by the second order perturbations and no longer appears at the centre of gravity of the lineshape, but is displaced with respect to the true isotropic shift by what is called the quadrupole induced shift (QIS)

$$QIS = -A(I)\frac{C_Q(1+\frac{\eta^2}{3})}{\mu_0^2} \tag{2.81}$$

where A$(I)$is a spin dependant term

$$A(I) = \frac{3}{40} \cdot \frac{I(I+1) - \frac{3}{4}}{I^2(2I-I)^2} \tag{2.82}$$

Furthermore, the shape of the quadrupole line can also be influenced by the strength of the $rf$ field used to excite the system, as this can lead to a miss-match in intensities due to non-selective excitation of the different orientations of crystallites and the satellite transitions. This can be overcome by using $rf$ at high frequency $\omega_{rf} >> \omega_{C_Q}$ where all transitions are excited equally and the outcome is similar to that for a spin $I$ = $\frac{1}{2}$ nucleus; conversely if $\omega_{rf} << \omega_{C_Q}$ then the pulse is not capable of irradiating the satellite transitions this is selective excitation and leads to a reduction in intensity of the signal. However in the intermediate case $\omega_{rf} \sim \omega_{C_Q}$, the response of the quadrupolar nuclei to the $rf$ can cause problems. The excitation response of quadrupolar nuclei is dependent on the applied $rf$ and $\omega_{C_Q}$, however $\omega_{C_Q}$ itself, depends on molecular orientation. Therefore the response of nuclei in chemically equivalent environments, but with different orientations to the applied field, will have a different response to the $rf$. This manifests as each molecular orientation having a different nutation rate, which is seen in the spectrum as distortions to the lineshape, it is found that the only way to remove these effects is to use 'hard pulses' (high power $rf$ pulses with short tip

angels).

## 2.5.4  J-coupling

J-coupling also known as scalar coupling or indirect dipole–dipole coupling arises from the interaction of the electrons between two or more nuclei that are directly bonded together. This is similar to the dipole-dipole interaction, where the magnetic fields interact through space and cause observable effects to surrounding nuclei, however in the case of J-coupling the interaction is strictly a through bond phenomenon. in this case perturbations to the electrons in the bond caused by one nucleus give rise to an additional magnetic field at the second nucleus. The Hamiltonian that describes this interaction is

$$H_J = -2\mathbf{I} \cdot \mathbf{J} \cdot \mathbf{S} \tag{2.83}$$

Where $\mathbf{J}$ is a 3 x 3 tensor matrix. However there is no $\mathbf{B}_0$ dependence on the J-coupling tensor as it is completely isotropic, therefore the 3 x 3 tensor reduces to a scalar whose value is the average of the diagonal elements in coupling tensor

$$J = \frac{1}{3}(J_{xx} + J_{yy} + J_{zz}) \tag{2.84}$$

The Hamiltonian for the J-coupling thus reduces to

$$H_J = 2\pi J \mathbf{I} \cdot \mathbf{S} \tag{2.85}$$

While this J-coupling tensor is reduced to its isotropic part, there is a small anisotropic interaction which can still occur; this is averaged out in liquids, and while still present in solids it is very small with respect to other interactions and is therefore is obscured and is generally ignored. Likewise in solids even the isotropic component is often obscured by other larger interactions such as dipolar and quadrupolar effects.

In liquids however, just as the dipole-dipole interaction is averaged out by molecular tumbling the J-coupling being isotropic in nature is preserved and reveals invaluable structural information. This causes a splitting of the resonance from the Zeeman interaction into the number of interactions present. For example if only one bond is

37

present, between two spin $I = \frac{1}{2}$ nuclei, then what will appear in the spectrum is two lines separated by the value of the J-coupling (see Figure 2.10a). If coupled to two identical nuclei, then three lines will appear of a 1:2:1 intensity all separated by the J-coupling value (see Figure 2.10b). The value of J-coupling ranges from Hz to 100's of Hz, the magnitude of the J-coupling is influenced by the covalence of the bond and the number of bonds, the respective gyromagnetic ratios, and whether the interaction is homonuclear or heteronuclear, with heavy nuclei found to have larger J-couplings.
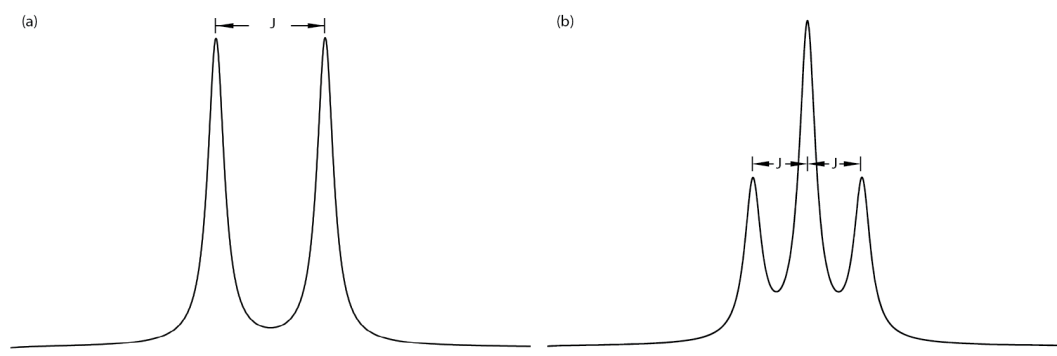
Figure 2.10: Example of J-coupled spectra, (a) A doublet showing a spin half $\frac{1}{2}$ coupled to another spin $\frac{1}{2}$ separated by the scalar coupling J. (b) A triplet, this time a spin coupled to two other spins.

Despite the problems associated with solids, it is still possible to resolve J-couplings, the anisotropy for the J-coupling is similar to that in the dipole interaction and can be suppressed using magic angle spinning as it contains a $(3\cos^2\theta - 1)$ term. However, the required resolution needed for small J-couplings is still difficult. This can take the form of poor instrument set up, any broadening caused by structural disorder, residual dipole-dipole couplings can also be a problem, though this can be removed through the use of very high magic angle spinning and decoupling techniques, if not, then the use of specific pulse programs that can resolve the J interaction or suppress the dipole-dipole interaction are used. Even if not possible to resolve the actual J-coupling in solids it is still possible to use the experiments to determine if there are any directly bonded nuclei in a sample as by suppressing all other signals, any signal that is left will be due to J-coupled sites.

# Chapter 3

# Experimental Techniques in Solid State NMR

The NMR experiment is technically challenging for a number of reasons, this is in part due to the very weak signal that is produced by the oscillating magnetic moment. The strength of the signal is influenced by several factors, the size of the nuclear magnetic moment in question, the population difference given by the Boltzmann distribution, thus high strength static magnetic fields of many Tesla are preferable. Signal strength is also dependant on the natural abundance of the isotope, affecting the required volume of sample needed, and can be problematic when using magic angle spinning. High levels of resolution are also required to be able to differentiate between the slightly different frequencies, arising from slightly different chemical environments, which in liquids can be less than 1 Hz. However the resolution capabilities of the instrument are not so much of an issue in modern systems and the problem has been largely solved by using high homogeneity magnetic fields across the sample volume. Problems with resolution can still cause issues, but they tend to be more sample dependant especially in solids. What follows here is a brief description of the hardware involved in the solid state NMR experiment followed by some of the techniques and experiments that are used to extract various information from the samples.

## 3.1 The Solid State NMR Spectrometer

The solid state NMR spectrometer is a complicated piece of equipment, however most of it can be broken up into several distinct parts which are illustrated by the block diagram in Figure 3.1, it is not necessary to explain the technicalities of each part and the focus will be purely on the function of each part, more detailed reading can be found in references [44, 50–56]
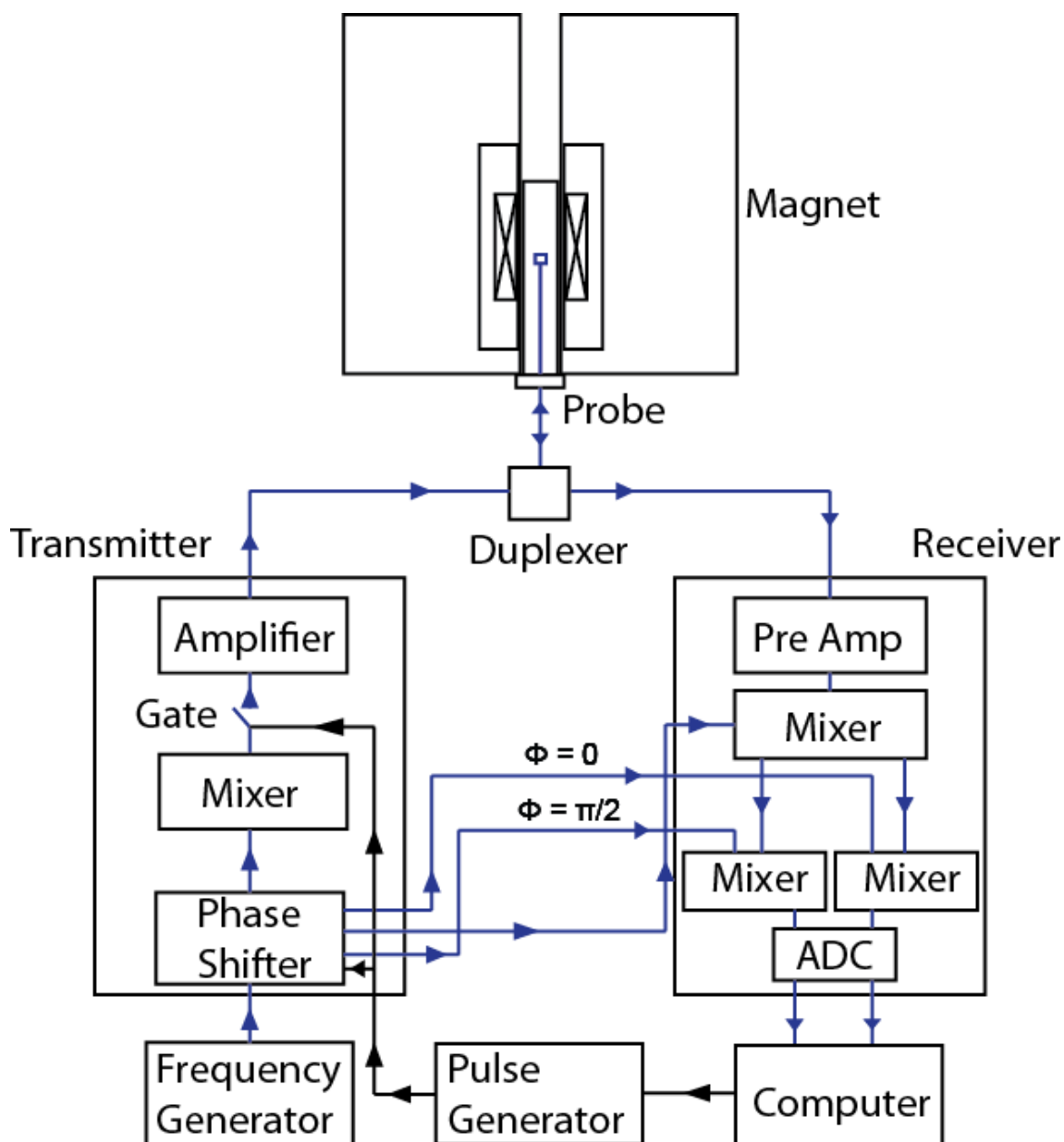


Figure 3.1: A Schematic overview of a single channel solid state NMR spectrometer, with the key parts illustrated.

### 3.1.1 The Magnet

The first thing that is required is a static magnetic field, generally this is as strong as physically possible, with the more common field strengths used today being greater than 7 T up to very high fields of 20 T or more, however lower fields 3-4T are still used in some cases such as looking at paramagnetic materials. The static magnetic field must have very high homogeneity across the sample volume, and in solid state experiments the volume is of the order of tens of cubic centimetres. In order to achieve such large stable magnetic fields super conducting solenoids are used, the solenoid is cooled down to the boiling point of liquid helium by full immersion in a bath of the same, and once charged with current runs almost indefinitely. The bath of liquid helium is surrounded by a vacuum jacket to help stop thermal leakage, this vacuum jacket is in turn surrounded by a reservoir of liquid nitrogen which is also surrounded by another vacuum space, with both reservoirs requiring refilling regularly. The bore of a magnetic used in solid sate NMR is typically 83 mm in diameter so as to accommodate the probes and the large sample volumes, conversely a liquids magnetic will typically have a bore size of 59 mm.

The field homogeneity of the sample volume is improved by making corrections to the field produced by the main solenoid, these are the superconducting shim coils and the room temperature shim coils. Shim coils are separate sets of coils with different geometries that allow manipulation and fine adjustment to the shape and homogeneity of the overall magnetic field. The super conducting shim coils are set shortly after the magnet is first charged (put to field) and after it has stabilised. The room temperature shim coils are not physically attached to the magnet but fit inside the bore of the magnet, these coils can be adjusted by the user, this is done by varying the amount of current in each coil. Shimming with the room temperature coils is done routinely, as each probe has a slightly different geometry and sample volume and requires slight differences in the region of high homogeneity. However it does not need to be done every time the probe is changed, as it is possible to store the values and recall them for each probe at the user interface, but will still need changing periodically.

### 3.1.2 Transmitter

In order to manipulate the magnetic moment or spin system in the sample, radio frequency ($rf$) pulses are required. The transmitter section (see Figure3.1) will be made up of several channels to produce various frequencies simultaneously allowing for complicated multi-frequency experiments. The specific workings of the transmitter differs between different manufactures and models, so an explanation will be given in the most general of terms for single channel operation. In simplest terms the transmitter section consists of several parts: an $rf$ synthesiser, a pulse programmer, a fast switch (or gate) and an amplifier in order to create usable amplitude radio frequencies at the Larmor frequency required.

The radio frequency synthesiser is used to create an oscillating voltage of well defined frequency, this frequency is called the intermediate frequency or reference frequency of the spectrometer $\omega_{IF}$. The intermediate frequency supplies a continuous stable source of $rf$ that all of the other necessary frequencies can be derived from. NMR experiments require specific phases and lengths of pulses, the phase of the intermediate frequency is changed as desired by a pulse programmer. The pulse programmer also controls a fast switch (also known as the pulse gate), the fast switch gives accurate control of the length of pulses and essentially chops sections out of the continuous $\omega_{IF}$ of the desired length. Prior to the pulse being generated by the gate, the intermediate frequency is mixed with another frequency ($\omega_{mix}$) from a variable frequency source to make the desired Larmor frequency ($\omega_0$), depending on the particular spectrometer this can take the form $\omega_{IF} - \omega_{mix} = \omega_0$ or $\omega_{IF} + \omega_{mix} = \omega_0$ as different manufacturers/models have different intermediate frequencies. After the pulse gate the $rf$ pulse is passed through an amplifier, this is because all the previous treatment to the $rf$ was achieved at very low voltages, and the amplifier then scales up the $rf$ to the desired amplitude, where the power output from the amplifier can vary between a few watts to a kilowatt or more at peak power.

### 3.1.3 The duplexer

After the $rf$ is of the desired frequency, amplitude and duration, it passes through what is called the duplexer (see Figure 3.1). The duplexer performs a very specific and important job, as it not only allows the $rf$ coil to transmit the high voltage used to create the $\mathbf{B}_1$ field but also allows the same coil to receive the detected voltage as well. As the transmitted voltage is high, hundreds of volts compared to the received voltage, which is of the microvolt range. Then there has to be some mechanism that stops the transmitted voltage being directed to the receiver, as the receiver is designed to detect very small voltages and will be severely damaged if any of the voltage from the transmission is allowed through.

There are different ways of doing this, such as using fast switching, or a very common method is to use a mixture of quarter wavelength cables and crossed diodes which uses the $rf$ itself to cause the switching in the circuit. The diodes in the circuit under high voltage look like a switch, causing all the voltage from the transmitted pulse, not to see the part of the circuit going to the receiver and therefore it all goes to the probe, then when the voltage induced in the receiver coil is not high enough to activate the diodes all the signal goes to the receiver.

### 3.1.4 The Probe

One of the most essential components of the NMR system is the probe. There are many different types of probes, as it is not possible to construct a single probe that will do all tasks, for use in solids these range from static probes, high volume low spinning speed probes, low volume high spinning speed probes, low temperature probes (cryoprobes) high temperature probes (furnace probes) multi channel probes, special low frequency probes and more.

The probe has to be able to place the sample in the region of homogeneous magnetic field also known as the sweet spot. The probe contains all of the electronics required to transmit the pulses generated by the spectrometer as an electromagnetic wave, subsequently it also contains the electronics for detection of the oscillating magnetic field created by the sample.

While there are different types of probe based on whether the experiment is for liquids or solids the basic concept is essentially the same. The sample is located at the most homogeneous region of the $B_0$ field, and is surrounded by the coil (often called the work coil) that produces the $B_1$ field and detects the decaying signal from the sample. Other arrangements using two coils can be used, one for transmission and the other for detection, but this configuration is used less often due to electronic effects between the two coils and due to physical limitations in construction.

The electronics in the probe are often complicated so a simple description of the main workings will suffice. The coil makes up part of an $LC$ circuit (see Figure 3.2) often called a tank circuit. The tank circuit consists of the work coil in parallel with a capacitor (often called the tuning capacitor). The object of the tuning capacitor is to store energy in the electric field between the capacitor plates, and the inductor (coil) stores energy in its magnetic field. As the capacitor discharges a current flows in the coil, the current flowing in the coil produces a magnetic field around the coil. The energy that was stored in the capacitor is transmitted to the magnetic field until the capacitor is completely discharged, the energy in the coil is then reduced by charging the capacitor with the opposite polarity, this process flows back and forth, hence the circuit is said to resonate at a particular frequency. This frequency is approximately

$$\omega = \frac{1}{\sqrt{LC}} \tag{3.1}$$

Of course this does not happen indefinitely as energy is lost from the system through resistance. If the circuit is tuned to the same frequency as the signal transmitted from the spectrometer, then the circuit will create a oscillating magnetic field at that frequency, essentially the Larmor frequency. When receiving a signal the opposite happens the rotating magnetic moment induces voltages in the coil of a particular frequency or frequencies and the response of the tank circuit when tuned to these frequencies is to accumulate energy of the weak NMR signal.

A second capacitor is often connected in series with the tank circuit, this is called the match capacitor and matches the impedance of the tank circuit to the rest of the spectrometer circuit which is often 50 ohms. Once the circuit has been tuned and

44
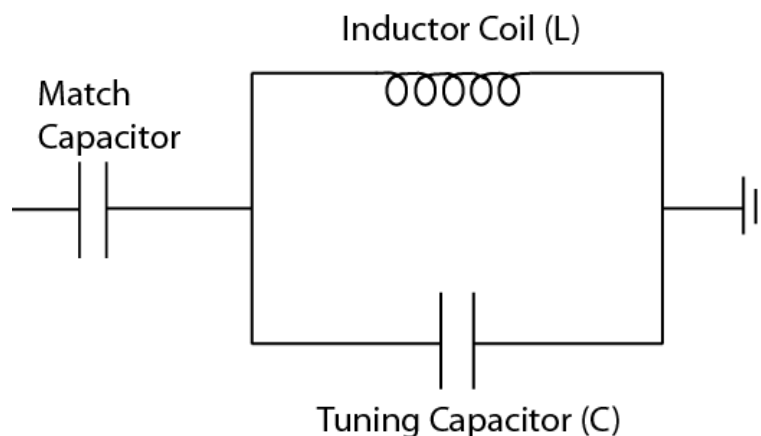
Figure 3.2: Illustration of a resonance circuit similar to that found in a NMR probe, where it is used to create the $\mathbf{B}_1$ field and detect the signal form the sample.

matched it can only be used for a specific frequency and therefore in most cases to a particular nucleus, however, though rare, it is possible that two different nuclei present in a sample have similar frequencies.

Probes are often constructed so that they can be tuned to many different frequencies using variable capacitors and exchangeable capacitors. Probes can also be constructed so that they can be tuned to several different frequencies at once, all operating through the same coil, however this also makes the electronics configuration of the probe more complicated due to keeping all the channels separate from each other.

## 3.1.5 The Receiver

After the signal generated by the spectrometer has been transmitted to the probe and used to manipulate the spins in the sample and a signal has been induced in the coil it then comes back to the duplexer where it is directed to the receiver. The signal which is an oscillating voltage of the form

$$S(t) = cos(\omega_0 t) exp^{(\frac{-t}{T_2})} \tag{3.2}$$

This very weak signal is then passed through a pre-amplifier where the signal is scaled up to a more useful voltage level. The next process reduces the frequency of the NMR signal which can vary widely depending on the nucleus, and in order to simplify the operation of the system the frequency of the detected signal is mixed with $\omega_{IF}$ and

the signal now oscillates at some relative Larmor frequency $\omega_{rel}$, doing this greatly simplifies the operation of the receiver as none of the electronics need to be re-tuned for different nuclei. The signal now has the form

$$S(t) = cos(\omega_{rel}t)exp^{(\frac{-t}{T_2})} \tag{3.3}$$

however the signal given by equation 3.3 does not differentiate between signals that are of higher frequency and lower frequency than $\omega_{rel}$, therefore the signal is split into two components. The two components are then passed to phase sensitive detectors, and are again combined with the intermediate frequency produced by the spectrometer, however one of the signal components is combined with the intermediate frequency that has had a 90° phase shift. After the phase shift the two signals are then filtered so they make up the two components $S_{real}$ and $S_{imag}$ of a complex signal having components,

$$S(t)_{real} = cos(\omega_{rel}t)exp^{(\frac{-t}{T_2})} \tag{3.4}$$

$$S(t)_{imag} = sin(\omega_{rel}t)exp^{(\frac{-t}{T_2})} \tag{3.5}$$

this two output scheme is called quadrature detection, the advantage of this is that now it is possible to tell the difference between frequencies that are moving faster or slower than that of the Larmor frequency. These two separate components of the complex signal are then passed to analogue-to-digital converters (ADC) where the signal is converted to a digital form. The two separate digital components of the signal are then passed to the computer with the user interface where they can be stored, Fourier transformed and be subjected to further post processing by the user.

## 3.2    Magic Angle Spinning

Probably the most widely used experimental technique used in solid state NMR is magic angle spinning [32], more commonly known as MAS. In liquids rapid molecular tumbling averages out many of the internal interactions, however this is not possible in solids. The large majority of samples analysed are polycrystalline in nature and there-

fore consist of many crystallites with random orientations. The internal interactions, chemical shift, dipolar coupling, scalar coupling and the quadrupole interaction all have components that are dependant on crystal orientation and are said to be anisotropic. Therefore solid state NMR spectra contain broad lines caused by the slightly different frequencies arising from the many different crystallite orientations. While it is possible to analyse such spectra and determine structural properties, it becomes increasingly difficult to interpret and analyse such spectra if they contain more than one chemically inequivalent crystal site with overlapping resonances.

Fortuitously the molecular orientation dependence of the internal interactions discussed in Chapter 2.5, all involve the same $3cos^2 \theta$ - 1 term, and in a powder sample effectively all values of $\theta$ are represented. If the sample is rotated, the angle $\theta$ will vary with time as the orientation of each crystallite changes. This angular dependence $3cos^2 \theta$ - 1 is proportional to the $2^{nd}$ degree Legendre polynomial

$$P_2(cos\theta) = \frac{1}{2}(3cos^2\theta - 1) \qquad (3.6)$$

for the angle 54.74° $P_2$ = 0. The angle 54.74° is called the 'magic angle' and it is found that by rotating the sample at the 'magic angle' it is possible to average out the $3cos^2 \theta$ - 1 term from the internal interactions, provided that the rotation rate is fast enough compared to the size of the interaction. Therefore it is possible to simulate the rapid molecular motion in liquids and in theory reduce the line width of solid state experiments to that of liquid state experiments. However this is generally not the case, there will in most instances be significant narrowing of the line widths, but residual effects from dipolar coupling can still cause broadening and the chemical shift anisotropy can be significantly large enough that it is not possible to average it out completely. Disorder can also be a problem in solid state NMR, in liquids slight differences in frequency will be averaged out by molecular tumbling, but this is not the case in solids, even under MAS, and manifests as broadening of the lines. Similarly, quadrupolar nuclei that have large $C_Q$'s are still broad under MAS, as the second order perturbations have a second angular dependence, and the line width is only partially narrowed (by approximately a third)by MAS [51], however it is possible to overcome

this and will be discussed in the next section.

In order to average out the anisotropy of the interaction the rotation rate ($\omega_r$) has to be a factor of three or more greater than the anisotropy ($\Delta\omega$) and it is not always possible to achieve this, if the rotation of the sample $\omega_r << \Delta\omega$ then it will not be much different than the static spectrum. If the rotation rate of the sample $\omega_r \approx \Delta\omega$ the line width will still narrow significantly with a narrow line at the isotropic chemical shift but will also be joined by what are called spinning sidebands (see Figure 3.3a) which are shifted from the isotropic peak by $\pm \omega_r$. The isotropic peak will not necessarily be the most intense peak or the central peak as overall shape of the spinning side band pattern will reflect the shape of the anisotropy, and the only way to determine what peak is the isotropic shift is to spin at different speeds, as the isotropic shift is the only one that will not move, if the spinning speed is increased the number and intensity of side bands will decrease.

Despite improving resolution, several factors have to be taken into consideration when using MAS, the anisotropies are field dependant and this can provide complications at higher magnetic fields and requires even faster spinning speeds. The presence of spinning side bands can make interpretation of spectra difficult when there are multiple sites, however sometimes it is desirable to have spinning side bands as they can be analysed to give information as to the anisotropies and asymmetries in the sample.

MAS probes come in many different configurations, these range from high sample volume (several grams of sample) with slow spinning speeds 2-4 KHz, to very small volume (tens of milligrams of sample) and very high spinning speed greater than 60 KHz, speeds of up to 80 or 90 KHz are possible but not quite routine yet. They all work in generally the same way (see Figure 3.3b), with the sample holder (otherwise known as a rotor), sitting on an gas bearing, the rotor has a turbine cap at one or both ends which is also driven by gas, the gas is usually compressed air or nitrogen. Due to the incredible forces involved when the samples are spun, the materials that the rotors can be made from are limited as they have to be strong and light enough, the most common materials used for rotors are zirconium dioxide ($ZrO_2$) and silicon nitride ($Si_2N_3$).
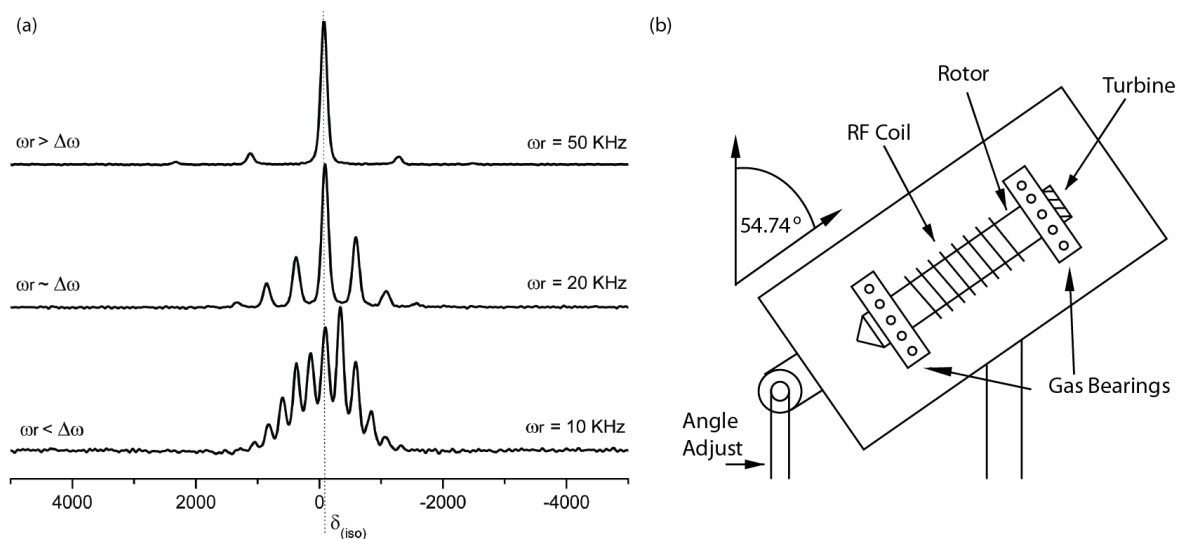
Figure 3.3: (a) MAS spectra showing how changes in the rotation frequency $\omega_r$ $\omega_r$ affects the line shape and width, when spun at various speeds relative to the static line width $\Delta\omega$ (b) a schematic representation of a MAS probe head.

## 3.3 Double Angle Rotation

As described in the previous section, spinning at the magic angle helps to reduce the broad lines of solid state NMR experiments to narrow lines at the isotropic shift, by averaging out the angular dependence of the internal interactions. However, if second order perturbations to the Zeeman interaction due to large quadrupole couplings have to be taken into account, MAS will only reduce the linewidth by around a third through the removal of first order effects, which have the same angular dependency ($3cos^2$ $\theta$ - 1) as the other internal interactions, this can leave significant broadening due to the second order effects, and can make interpretation of the spectra complicated if there are overlapping sites. The reason the linewidth is only partially narrowed, is because the second order perturbations have a different angular dependence, this angular dependence is proportional to the fourth degree Legendre polynomial $P_4(cos\theta)$, where

$$P_4(cos\theta) = \frac{1}{8}(35cos^4\theta - 30cos^2\theta + 3) \tag{3.7}$$

Comparing the angular dependence of $P_2(\cos\theta)$ (Equation 3.6) and $P_4(\cos\theta)$ (Equation 3.7) it can be seen that there is no common root. However, relative to the magic angle

54.74°, $P_4(\cos \theta) = 0$ has two solutions, 30.56° and 70.12° (see Figure 3.4). Therefore, as none of these solutions coincide with the magic angle, in order to remove all angular dependencies from second order quadrupole interactions will require rotating at two angles simultaneously, the magic angle 54.74° and one of the solutions to $P_4(\cos \theta) = 0$ relative to the magic angle.
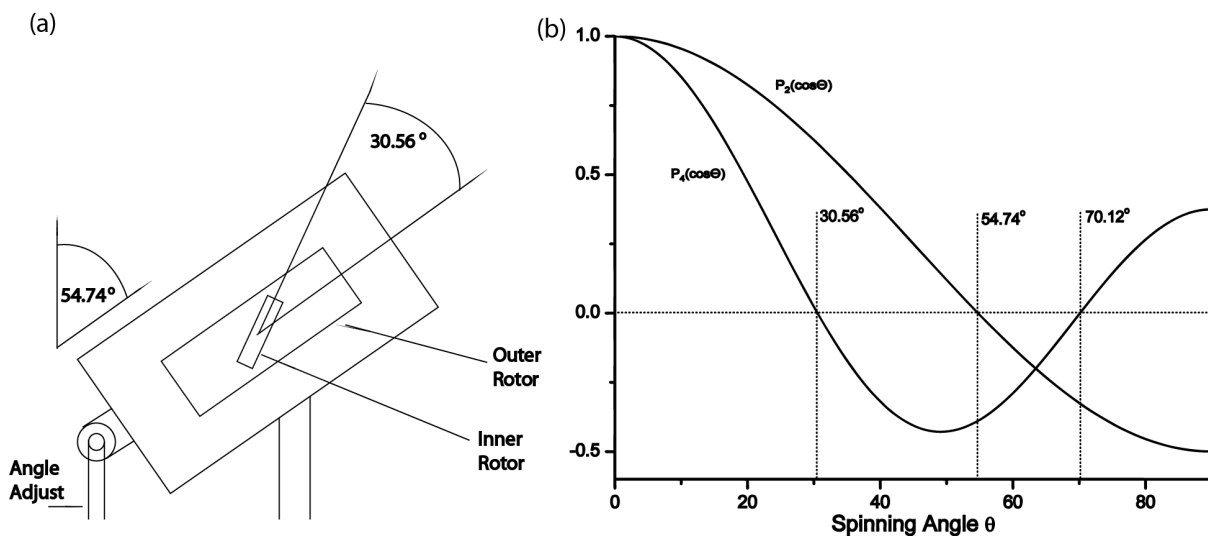


Figure 3.4: (a) Schematic representation of the DOR mechanism, the inner rotor is spun at an angle 30.56° relative to the inner rotor which spins at the magic angle 54.74°. (b) plot of $P_2(\cos \theta)$ and $P_4(\cos \theta)$ as can be seen there is no common root for the two functions.

A mechanical solution to satisfy spinning around two separate axes simultaneously was first implemented by Samoson *et al* [57]. This involved spinning a large rotor at the magic angle and having a secondary smaller rotor inside the large one spinning at an angle relative to the outer rotor (see Figure 3.4a), with the angle being a solution of $P_4(\cos \theta) = 0$ (i.e. $\theta = 30.56°$). This technique is known as double rotation (DOR) and can remove all first order and second order sources of quadrupolar broadening, and has been shown for several nuclei that is possible to reduce the linewidth to that comparable of spin $\frac{1}{2}$ nuclei. [58]

However, there are some drawbacks, due to the very complicated arrangement for spinning it is not possible to achieve very high spinning speeds, the outer rotor can only really achieve a maximum of 2 KHz with the inner rotor at $\sim 4.5$ times this. The low speed is often less than the static line width $\Delta \omega$ and can cause problems with side bands, especially in the presence of multiple sites just as with MAS, and with the

slow spinning speed it is not so useful for nuclear species that have very large $C_Q$'s. Despite this, the problems with side bands can be mitigated to a certain extent by synchronising every acquisition with half a rotor period and keeping the phase cycling constant for every two subsequent pulses, this removes all odd numbered side bands, effectively doubling the rotor period [58]. The small sample size can also be a hindrance for lower abundance nuclei and the technique is more suited to high natural abundance nuclei, though this can be overcome with isotopic enrichment. However as in MAS crystallographic disorder can still cause severe problems [59].
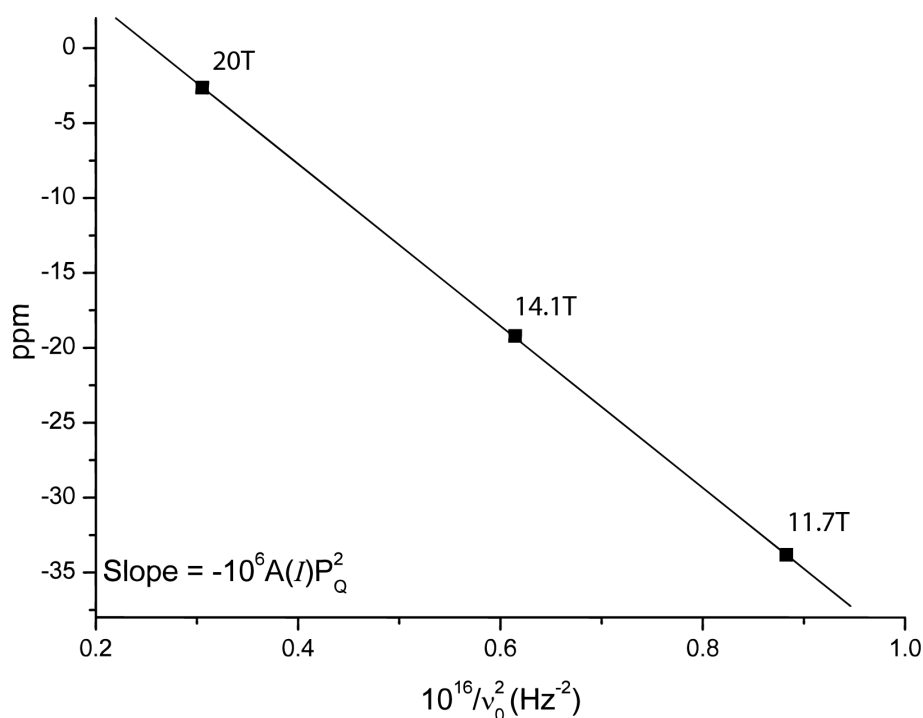


Figure 3.5: Plot of DOR line position at three different magnetic fields against $1/\nu_0^2$, the intercept gives the isotropic shift $\delta_{iso}$ and the slope $P_Q$ (see Equation3.8)

Despite the resonances being narrowed in the DOR experiment so that they are comparable to spin $I = \frac{1}{2}$ nuclei, the resonances do not appear at the isotropic chemical shift, instead they appear at the centre of gravity of the MAS quadrupole lineshape. The lines are shifted from the isotropic shift ($\delta_{iso}$) by the quadrupole induced shift (see Chapter 2.5.3 for QIS), so the shift from the DOR ($\delta_{DOR}$) experiment is,

$$\delta_{DOR} = \delta_{iso} - QIS = -A(I)\frac{P_Q^2}{\nu_0^2} \tag{3.8}$$

where A($I$) is a spin dependent term defined in Chapter 2.5.3 and $P_Q = C_Q(1 + \eta_Q^2/3)^{1/2}$. $P_Q$ is called the quadrupolar product and $\nu_0$ is the Larmor frequency. It can be seen from the expression in Equation 3.8, that $\delta_{DOR}$ is inversely proportional to $\nu_0^2$ and $\delta_{DOR}$ will shift in a linear fashion, depending on the strength of the $\mathbf{B}_0$ field. Therefore by repeating the DOR experiment at different magnetic field strengths, it is possible to extract $P_Q$ and the isotropic chemical shift, by plotting the observed shift from each experiment against $1/\nu_0^2$, where the intercept gives the true isotropic chemical shift and the slope gives the information relating to $P_Q$ [58], an example of this is presented in Figure 3.5.

## 3.4 The NMR Experiment

The information that can be extracted from a spin system in an NMR experiment is contained within the amplitudes and frequencies of the acquired NMR signal, this information is determined by the type of experiment that is implemented in the first place. The type and nature of the experiment is contained in what is called the pulse program . The pulse program is designed to excite or suppress parts of the spin system through the $rf$ so that the required information appears in the signal. The pulse program contains all of the parameters for the operation of the spectrometer to transmit and receive the $rf$ at the desired frequency, and contains among others the following parameters, the amplitude of the pulses, the length of the pulses, the delays between pulses, the phases of pulses and the receiver, and the time the signal is acquired for.

### 3.4.1 Pulse Programs

The simplest type of pulse sequence is the single pulse experiment (see Figure 3.6) and simply consists of a pulse of the required amplitude and length to create a transverse magnetisation, followed by the time the signal is acquired for. The single pulse experiment is used for many applications, such as calibrating the power requirements and the length of pulses, setting the room temperature shims, setting the magic angle and acquiring the reference for whatever nucleus is being observed. By far the most

common use of the one pulse experiment is to gain chemical shift information. This can be done in a single scan depending on the strength of the signal, but more likely needs repeat acquisitions to reduce the noise level in the spectrum, then the experiment is just repeated over and over with a delay inserted between each repeated pulse equal to approximately five times $T_1$, until a satisfactory signal to noise ratio (S/N) is achieved.
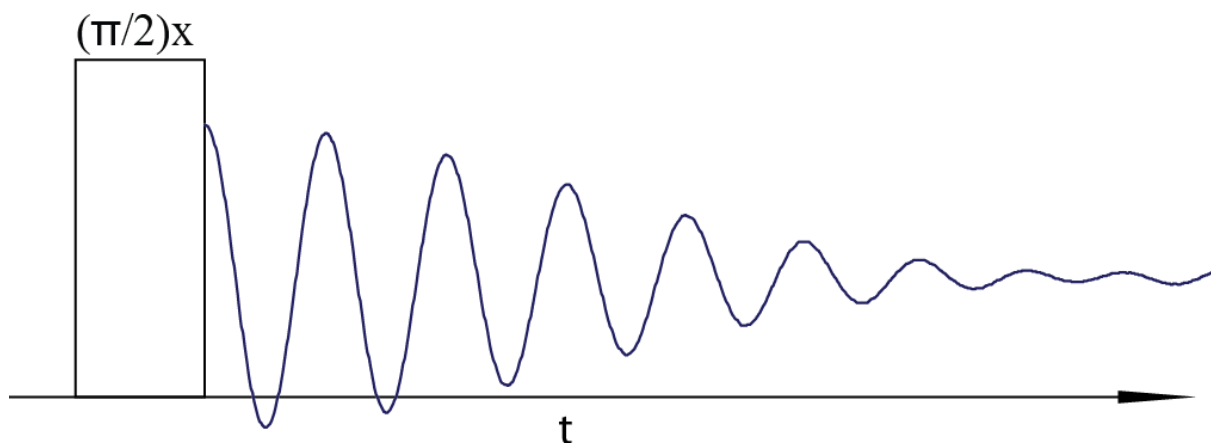


Figure 3.6: Pictorial representation of the single pulse experiment, a $\pi/2$ pulse is applied along $x$ then the FID is acquired, experiment is repeated after system has relaxed back along $\mathbf{B}_0$, and then repeated until a satisfactory S/N ratio is achieved.

However it is not always as straight forward as this, noise is a constant problem in NMR experiments and has many sources [50], and in many cases the noise levels are larger than the observable signal, fortunately as noise is random in nature, repeated experiments averaged or added together increase the S/N ratio. The S/N ratio increases as $\sqrt{n}$ where $n$ is the number of repeat experiments, and as $n$ is proportional to the time it takes to do each experiment, it can be seen that in order to double the signal to noise the experiment needs to be four times as long. This can be a limiting factor as instrument time is usually constrained and if a decent signal to noise is not acquired in one day there is often not much point in continuing, as that needs an increase to four days then sixteen days and so on.

Apart from the single pulse experiment, all other NMR experiments contain two or more *rf* pulses. One such example, is the spin echo experiment [60], while not used directly for the work in this thesis, it is the simplest two pulse experiment that can be used to help explain the concept of phase cycling the pulses, and the delays between pulses that are used in more complicated pulse sequences. The spin echo (see

Figure 3.7) has a variety of experimental applications, it can be used to overcome loss of signal due to probe ringing (physical movement of the *rf* coil), or by the need for dead times caused by physical effects in the spectrometer, or by allowing for a longer signal acquisition time due to very short $T_2$ times.



(π/2)x    (π)y

$t_1$    $t_2$
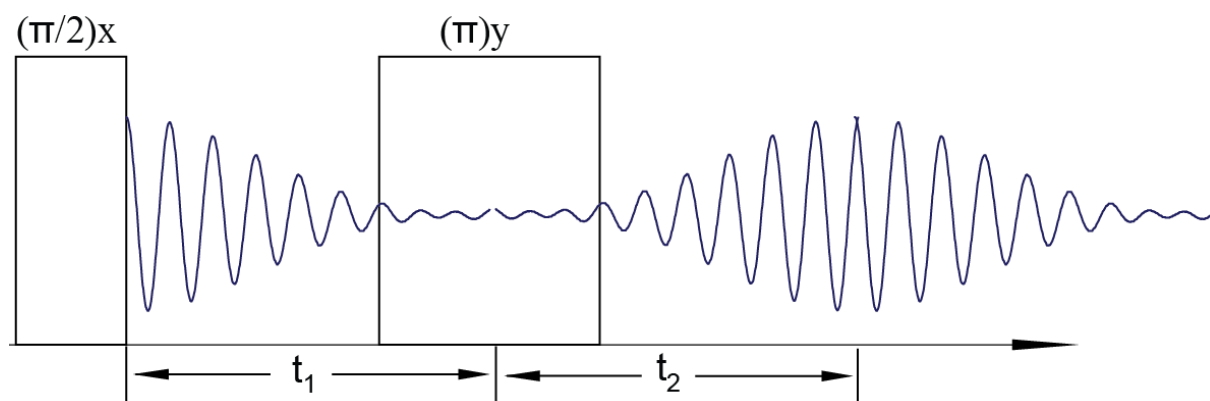
Figure 3.7: The spin echo experiment, after a time $t_1$ the de-phasing magnetisation in the $x$-$y$ plane is refocused with a $\pi$ pulse that forms a back to back FID with peak amplitude at time $t_2$

Essentially the experiment refocuses the magnetism in the $x$-$y$ plane, caused by the de-phasing of the spins, from the classical approach, as the spins start to de-phase in the $x$-$y$ plane, this can be seen as some spins are moving slower than the magnetisation and others are moving faster. The application of a 180° $y$ pulse after time $t_1$ flips the magnetisation, so that the faster spins are now moving behind the magnetisation and so catch up with the magnetisation, the fast spins and the magnetisation will then catch up with the slower components. The result of this, is that a back-to-back FID will form with highest amplitude at $t_2$, The timings $t_1$ between the pulses and $t_2$ after the 180° pulse can be calibrated to retain the signal intensity. Acquisition usually starts before the end of $t_2$ so that only the top of the echo is acquired not the full thing, and $t_1$ should be equal to an integer number of rotor periods in solids.

Phase cycling is required in the first instance, to remove any imperfections in the instrumentation, but more importantly phase cycling is used in the excitation and selection of different coherences, for a pulse sequence this is often shown in a coherence pathway diagram (see Figure 3.8). An *rf* pulse can change the order of a coherence level, so returning to the example of the spin echo, the entire pulse sequence can

be understood in terms of changes to coherence order. The first pulse creates a $\pm 1$ coherence (transverse magnetisation) which then evolves during time $t_1$, the second pulse then reverses the coherence order of the spins. This reversal of the coherence order is seen as the build up and decay of the spin echo.
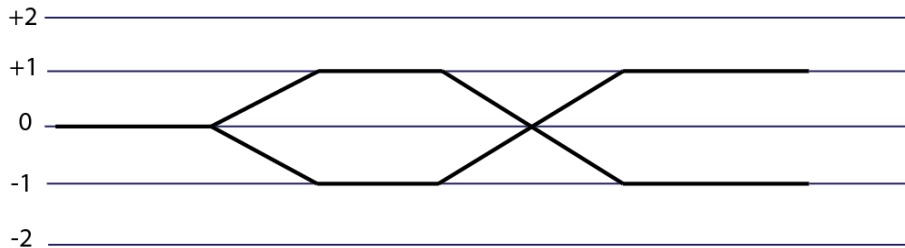


Figure 3.8: The spin echo experiment as a coherence digram, the first pulse creates a $\pm 1$ coherence, the coherence order is then reversed with a $180°$ pulse, the $+1$ pathway has no effect as only the -1 coherence is detected.

Table 3.1: Phase table for the spin echo experiment (see Figures 3.7 and 3.9)

| Step number | Pulse 1 $\phi$ | Pulse 2 $\phi$ | Receiver $\phi$ |
|---|---|---|---|
| 0 | 0 | 0 | 0 |
| 1 | 0 | 90 | 180 |
| 2 | 0 | 180 | 0 |
| 3 | 0 | 270 | 180 |

After the application of an *rf* pulse it is possible that many orders of coherence are created, for isolated spin $I = \frac{1}{2}$ nuclei it only possible to create the $\pm 1$ coherences, and the system only detects the -1 coherence. However, in systems of coupled spins such as in dipolar coupling it is possible to create higher order coherences such as a double quantum coherence which is the $\pm 2$ level. In reality a pulse excites many orders of coherence in coupled systems, but it is possible to be selective with which coherences are excited during successive pulses and which are filtered out. As an *rf* pulse changes the coherence order $\Delta$P (P $= \pm$ 1, 2, 3 ...) a pulse undergoing a change of phase $\phi°$ will cause a phase change in the coherence order of -$\Delta$P.$\phi$. If the experiment is repeated N times, where the phase is iterated after each acquisition in steps of $360°$/N, then after the complete cycle the signals from the desired pathway will add up constructively, and those undesired coherences will add up in a destructive fashion over the course of the phase cycle and cancel out. However, it is not possible to get rid of all coherence

pathways when phase cycling, as other coherence pathways are also created with order $\Delta P \pm nN$ where n is an integer. Higher order pathways can often be ignored, but sometimes only a single pathway is desired, this then requires more steps in the phase cycle. [44, 45, 61, 62].

The pulses that are to be phase cycled, and if the phases of the receiver also need to be cycled, depends on the desired coherence pathway or pathways to be selected. An example of phase cycling for the spin echo experiment is shown in Table 3.1, with an example of a $\pm 2$ coherence pathway selection using two pulses shown in Figure 3.9 along with the phase cycling in Table 3.2. Both phase cycling examples use a four step phase cycle, but by changing which pulse is cycled can give different results.
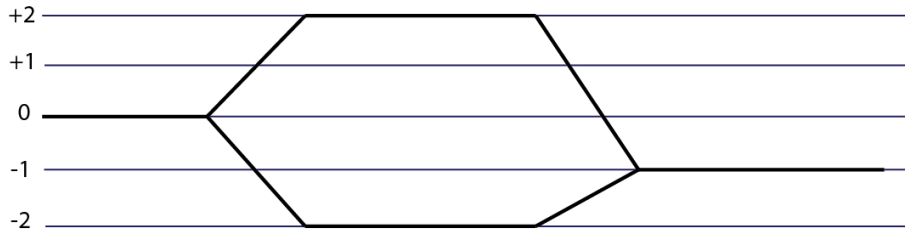


Figure 3.9: Example of a $\pm 2$ coherence pathway, coherence order is selected by a four step phase cycle on the first pulse and the receiver, all other coherence orders less than $\pm 4$ are blocked. There is no reason to phase cycle the last pulse as it will select the -1 coherence anyway.

Table 3.2: Phase table for selecting a $\pm 2$ coherence pathway (see Figure 3.9) by changing the phase ($\phi$) of the first pulse and the receiver

| Step number | Pulse 1 $\phi$ | Pulse 2 $\phi$ | Receiver $\phi$ |
|---|---|---|---|
| 0 | 0 | 0 | 0 |
| 1 | 90 | 0 | 180 |
| 2 | 180 | 0 | 0 |
| 3 | 270 | 0 | 180 |

## 3.4.2 The 1D NMR Signal

As was shown in Section 3.1.5 the signal from the probe detected in the receiver has the form

$$S \approx cos(\omega_0 t)exp^{(\frac{-t}{T_2})} \tag{3.9}$$

and contains all the frequency information contained in the NMR experiment, unless it only contains one frequency component Equation 3.9 is better described as

$$S(t) = \sum_n S_n(t) \tag{3.10}$$

where the $n^{th}$ component is given by

$$S_n(t) = C_n cos(\omega_n t) exp^{(\frac{-t}{T_2})n} \tag{3.11}$$

Each signal component consists of an amplitude term $C_n$ a frequency term $\omega_n$ and a decaying term $(\frac{-t}{T_2})_n$. The signal is then mixed down to the spectrometer reference frequency and split into two, so that it can be detected in quadrature, and is then passed to the computer in digitized form consisting of a real and imaginary part, where these consist of the sum of the real components and the sum of the imaginary components of the signal, respectively. However, for simplicity the discussion will be continued with the signal consisting of just one frequency component , so that the real and imaginary parts are

$$S_{real} = cos(\omega_r t) exp^{(\frac{-t}{T_2})} \tag{3.12}$$

$$S_{imag} = sin(\omega_r t) exp^{(\frac{-t}{T_2})} \tag{3.13}$$

The signal is then Fourier transformed at the computer from the time domain into the frequency domain, as this makes it easier to differentiate between the different frequency components. The mathematical definition of the Fourier transform from time domain to frequency domain is

$$F(\omega) = \int_0^\infty f(t) exp^{-i\omega t} dt \tag{3.14}$$

The Fourier transform is applied to both the real (Equation 3.12) and imaginary (Equation 3.13) components, as there is no way of differentiating between the sign of the frequencies then the Fourier transform will give two peaks one at $+\omega$ and one at $-\omega$ (see Figure 3.10). It is also seen that as the Fourier transform of $exp(-t/T_2)$ also has a real and imaginary component, this means that each signal component (real and imag-

57

inary) will have two frequency spectra associated with it, the real part consists of an absorption line shape and the imaginary will have a dispersive lineshape. Thus, Fourier transform of the quadrature signal gives four frequency spectra (see Figure 3.10). If the two absorption lineshapes are added together this produces another absorption spectra but this time with a single definite frequency. Likewise, if the dispersive spectra are added together, this produces a dispersive lineshape with definite frequency. It can now be seen how quadrature detection has resolved any ambiguity in the spectrum as the reflected features have opposite symmetries and are now removed.
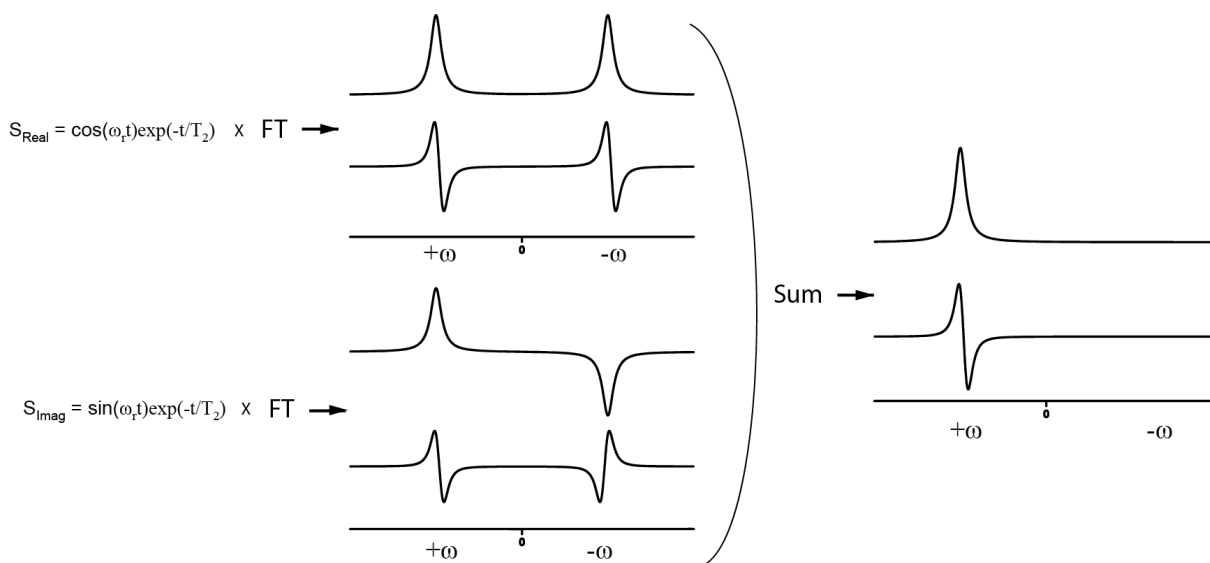


Figure 3.10: The Fourier transform of the real and imaginary parts of the signal will result in both parts being further split into another real and imaginary part due to the decaying exponential term $\exp(-t/T_2)$, As can be seen quadrature detection of the signal removes any ambiguity from the $\pm\omega$ frequency components once they have been summed, the final Fourier transformed NMR signal gives a real (absorption) and imaginary (dispersive) lineshape for the frequency in the signal.

The assignment of which component from the quadrature signal detection is real and which is imaginary is quite arbitrary, as the resulting spectral components will often be a mixture of dispersive and absorption components, and therefore will require post acquisition phasing. This is done manually at the computer, so that all the components in the spectrum are in phase and produce an absorption spectrum. The dispersion spectrum is now forgotten about as the absorption spectrum is the one of interest, however this is only because it has better resolution and is easier to analyse.

The width of the spectral line is a function of $T_2$ and will tend be a Lorentzian

shape in liquids or under MAS. However, in solids due to disorder, or lots of closely related frequencies from residual dipolar coupling the line shape will tend to be more Gaussian in nature or a mixture of the two, and as seen in Chapter 2.5.2 if the solids experiment is a static one, the line will be made up of many frequency components and its shape will reflect this.

### 3.4.3   The 2D NMR Signal

The information given by a 1D experiment is limited to two things, the amplitudes of particular resonances relative to each other and the chemical environment that the frequencies correspond to. Therefore, it is possible to determine what kind of molecular environments are in a sample and to a certain extent how much of it there is. It is also possible in some cases, that in samples that contain a limited number of resonances the 1D experiment can help in determining what a structure looks like. However in many cases it is not possible to specify which signals belong to specific parts of a material, such as specific locations in a crystal lattice for chemically inequivalent sites and which sites are close in space or bonded together. Likewise in order to determine accurately the constants $T_1$ and $T_2$ the 1D experiment is insufficient. In order to determine information beyond the chemical environment, requires the use of arrayed or 2D experiments.

The simplest of these arrayed experiments are still displayed as 1D experiments, such as determining the $T_1$, or the necessary duration of pulse required in an experiment. These types of experiment involve acquiring $n$ scans and then storing them. Then a particular parameter in the experiment is changed (e.g. pulse duration or time between successive scans) the experiment is then repeated, again for $n$ scans but with the changed parameter. This process is repeated for as many increments in the variable parameter as desired. The result of this is that all the stored experiments will give a matrix of data on how the amplitude of the signal changes with the duration of the pulse or in the case of delays between successive scans increasing intensity.

More complicated arrayed experiments are constructed so that the system evolves over a period of time between pulses, in Figure 3.11 a simple form of a two pulse
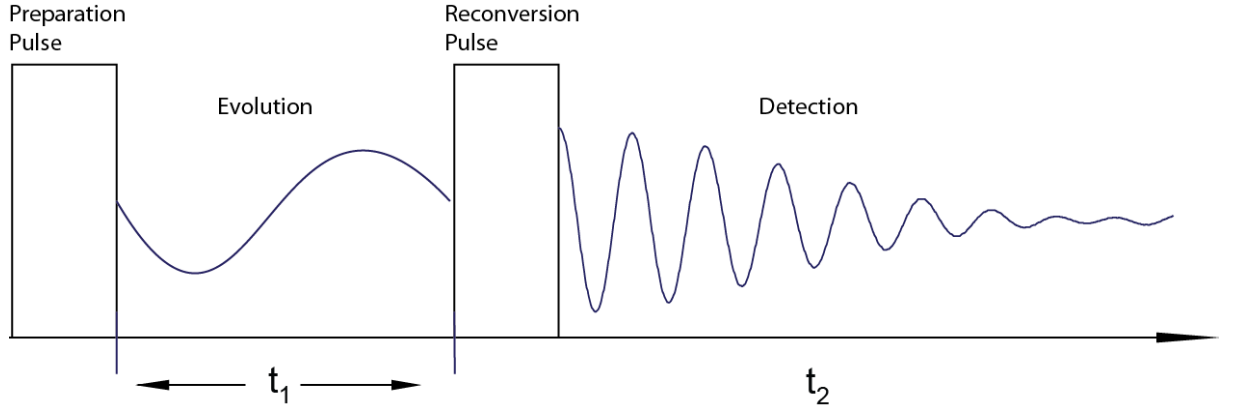
Figure 3.11: Example of a simple 2D experiment, the preparation pulse changes the state of the system which then evolves during $t_1$ and is then reconverted to a -1 coherence for detection during $t_2$, $t_1$ is then incremented after each successive batch of data acquisitions to make a 2D data set.

experiment is illustrated. The two pulses can be simply characterised as pulse one and pulse two for this discussion, but are often a collection of pulses rather than just one. Pulse one is a called a preparation pulse and puts the spin system into a particular state (i.e a particular coherence level), pulse two is a called the reconversion pulse, and converts the signal that has evolved after pulse one to the -1 coherence for detection. The two pulses are separated by $t_1$ and the acquisition occurs during $t_2$. Like in the example above for pulse length, a set of data is collected with a specific value of $t_1$, the acquisition is then run again keeping all the parameters the same, except for an increase in $t_1$, this process is repeated until the required number of data sets are recorded each time incrementing $t_1$. By repeating the experiment in this way, allows the observation of how the state of the system evolves over time, this is because any frequencies that are involved during the evolution are then encoded into the final signal along with any changes in amplitude and phase. The 2D data set then contains signals of the form

$$S(t_1, t_2) = \sum_i S_i(t_1, t_2) \tag{3.15}$$

where the $i^{th}$ component is given by

$$S_i(t) = C_i(cos(\omega_{i1}t_1)exp^{(\frac{-t}{T_2})_{i1}} + cos(\omega_{i2}t_2)exp^{(\frac{-t}{T_2})_{i2}}) \tag{3.16}$$

60

This data set is then Fourier transformed from the time domain to the frequency domain using the two dimensional Fourier transform

$$F(\omega_1\omega_2) = \int_0^\infty dt_1 \int_0^\infty dt_2 f(t_1, t_2) exp^{-i(\omega_1 t_1 + \omega_2 t_2)} \qquad (3.17)$$

the part of the signal with $\omega_2 t_2$ contains the usual information regarding chemical shift, whereas the frequencies from during the evolution period are contained in the $\omega_1 t_1$ part of the signal. The resulting Fourier transform gives a 2D correlation map (see Figure 3.12) where the $f_2$ axis corresponds to the chemical shift frequencies and $f_1$ contains the frequency information for the interaction being observed. Correlations will appear on the plot where there is an interaction between the frequencies $\omega_2$ and $\omega_1$.
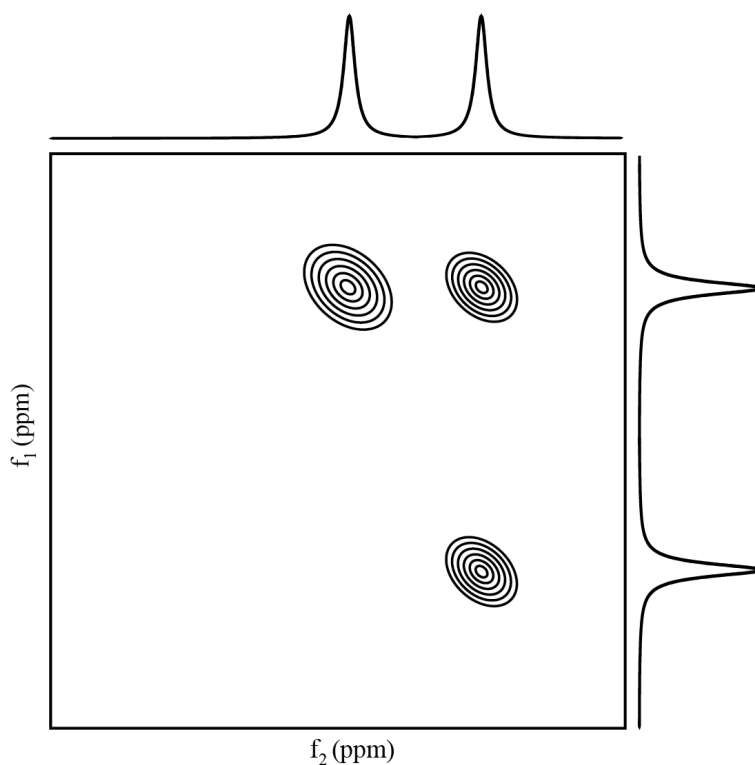


Figure 3.12: A simple illustration of a hypothetical 2D experiment after it has been Fourier transformed, the final spectrum will only contain data for those frequencies that have some interaction, and peaks will therefore appear where the particular $f_1$ and $f_2$ frequencies intersect on the plot. $f_2$ contains those frequencies of the chemical shift as in the 1D experiment, whereas the $f_1$ dimension contains those frequencies that were involved in the evolution period $t_1$

.

## 3.5 Solid State NMR Experiments

### 3.5.1 Saturation Comb

Primarily the saturation comb [63,64] (see Figure 3.13) is used as a method to determine the $T_1$ of a sample, whereby a series of 90° pulses separated by time, $t_1 \approx T_2$ destroys any magnetisation, then the experiment waits a time $t_2$ before a final pulse and detection. The wait period allows the build up of longitudinal magnetisation and is normally arrayed so that it gets incrementally longer for each data set. However there are other instances where it might be desirable to saturate the signal, in two of the experiments performed in this thesis, it has been used to pre-saturate the signal before each experimental acquisition. In order to do this, the saturation comb was modified so that the last pulse in the comb was replaced by the experiment pulse sequence, so that it would saturate, then wait, then perform the required experiment.
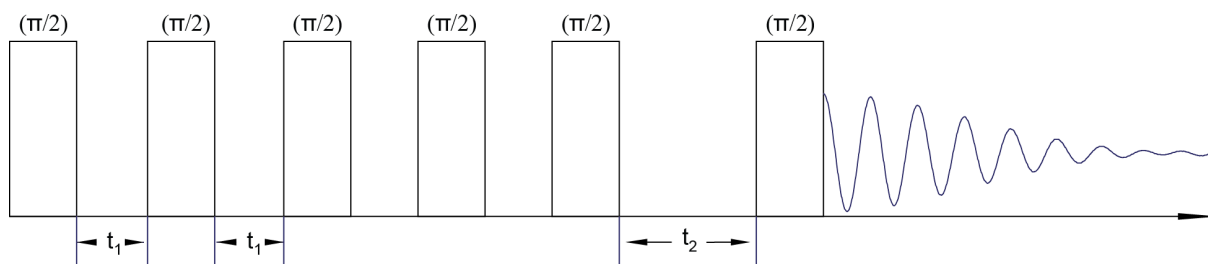


Figure 3.13: Saturation comb pulse sequence, n $\pi/2$ pulses separated by $t_1$ destroys the transverse magnetisation, $t_2$ can then be arrayed between successive acquisitions, before a final $\pi/2$ pulse to observe the build up of longitudinal magnetisation.

There are two reasons that it has be included, in the first instance it has been used because $T_1$ of the samples in question are long, greater than eight minutes and therefore a much shorter pulse delay has been used so experimental time is shortened, this has been implemented by using the saturation comb to ensure that the longitudinal magnetisation is the same for each sequential acquisition. The saturation comb was also found to remove problems with the phasing in some of the 2D experiments that make up this thesis. Phasing problems were found in the second dimension of 2D spectra when using pulse delays shorter than the relaxation time of the system, causing possibly what is called $t_1$ noise [65]. Therefore, by using a preceding saturation comb before each implementation of the pulse sequence this was found to prevent any problems

with the phasing from happening.

## 3.5.2  Dipolar Re-coupling R12$_2^5$ Experiment

Two dimensional correlation experiments can give valuable information to the proximity of what spins from different chemical shifts are associated with each other through homonuclear dipolar coupling [66] and therefore close in space, allowing a picture of the underlying structure to be determined. However, in solids as dipolar coupling broadens the signal the resolution is not good enough to do this kind of correlation. As discussed in Section 3.2 removal of dipolar coupling is achieved through MAS, this however, causes problems if it is desired to measure the coupling or do a correlation experiment. Therefore it is necessary to reintroduce it in some way, this can be achieved through the application of specific pulse sequences and phasing [67]. However, this can cause many problems with resolution due to reintroducing all dipole couplings, furthermore, it might also reintroduce the CSA causing more problems with resolution [45]. The solution to this is to use double quantum (DQ) filtered experiments [68], these experiments exploit the ability to create DQ coherences between coupled spin pairs in a network. This means that it is possible to be more selective and only interacting pairs will appear in the final spectrum. As the frequency of the coherence is related to the distance, then it is possible to determine the distance between the spin pairs, or in the case where there are many homonuclear spins in different chemical environments, it is possible to build up a picture of what chemical shifts are close in space and therefore can be related to specific positions within a structure [69]

The pulse sequence outlined in Figure 3.14 is the R12$_2^5$ pulse sequence and is part of the R$_n^N$ family of pulse sequences [70] n is the number of $\pi$ $\pi$ pulse sets in N rotor periods. For the experiments conducted within this thesis, the sequence was modified to include a saturation comb for the reasons discussed above in Section 3.5.1. This type of re-coupling pulse sequence allows excitation of the DQ coherence between dipole coupled spin pairs to the exclusion of undesired components, so that isolated uncoupled spins will not appear in the spectrum. The R12$_2^5$ pulse sequence consists of back to back $\pi$ pulses, with four $\pi$ pulses for every five rotor periods to excite the DQ coherence.
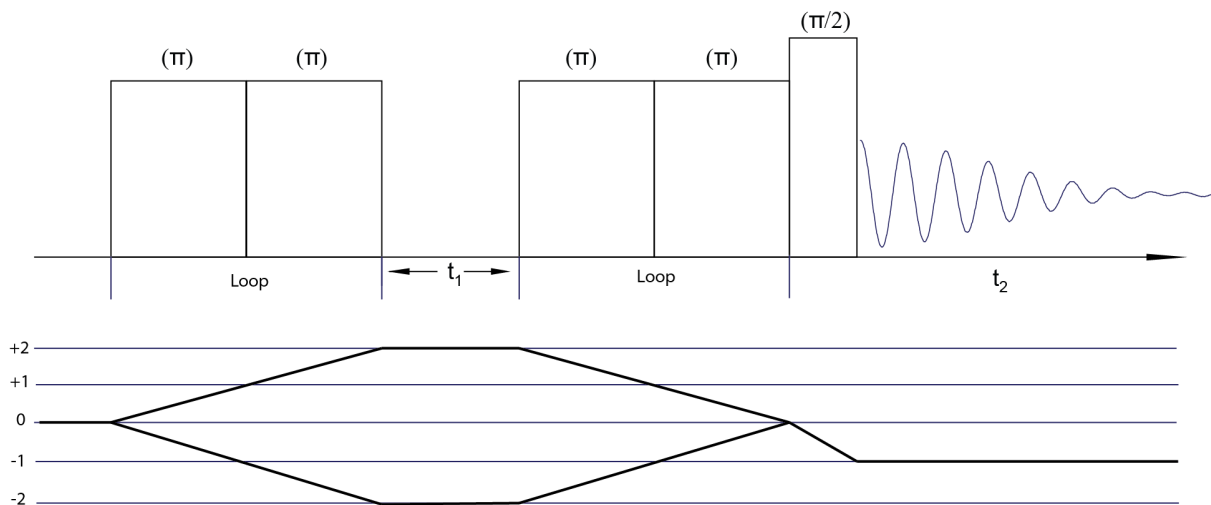
Figure 3.14: The R12$_2^5$ pulse sequence with coherence pathway, loops of n back to back $\pi$, $\pi$ pulses for every five rotor periods excite a DQ coherence that evolves during $t_1$, a second set of n $\pi$ $\pi$ pulses then reconverts the DQ coherence to a zero quantum coherence, before a final $\pi/2$ pulse converts the signal to the -1 coherence for detection.

The number of $\pi$ $\pi$ sets can be varied depending on the system being studied, the system then evolves during the period $t_1$, a four step phase cycle is then used along side the repeated series of $\pi$ $\pi$ sets to reconvert the DQ coherence to a zero quantum coherence before it is converted to a -1 coherence for detection by a $\pi/2$ pulse and a four step phase cycle.

The only information that is left in the signal is that corresponding to spin pairs, the final 2D Fourier transform plot will contain the original chemical shift information along $f_2$ axis, however as the DQ frequency is a combination of two frequencies $f_{2a}$ and $f_{2b}$, the resonances will appear on the $f_1$ axis at the sum of the two chemical shifts that are coupled together ($f_{2a}$ + $f_{2b}$).

### 3.5.3 Refocused-INADEQUATE

Another DQ filtered experiment is the refocused incredible natural abundance double quantum transfer experiment (Ref-INADEQUATE) [71]. However it is even more selective than the dipolar coupling experiments. This time the DQ coherence is created between those sites that are directly bonded together through the scalar or J-coupling between spins. Observation of the J-coupling in solids is difficult, even under MAS, as the J splitting is usually narrower than the residual line width due to dipole couplings.

64

As with the dipolar re-coupling experiment, DQ filtering is used to remove the signal from isolated spins while the dipolar coupling is removed through fast MAS, and the only signal left will be that from the J-coupled spins. The original experiments like this were designed to be performed on liquids [72] and were adopted sometime later for the use in solids [73], the solids pulse sequence is shown in Figure 3.15. The solids sequence is modified from the liquids experiment by having a refocusing echo at the end of the sequence in order to create an in phase -1 coherence for detection signal instead of a single 90° pulse
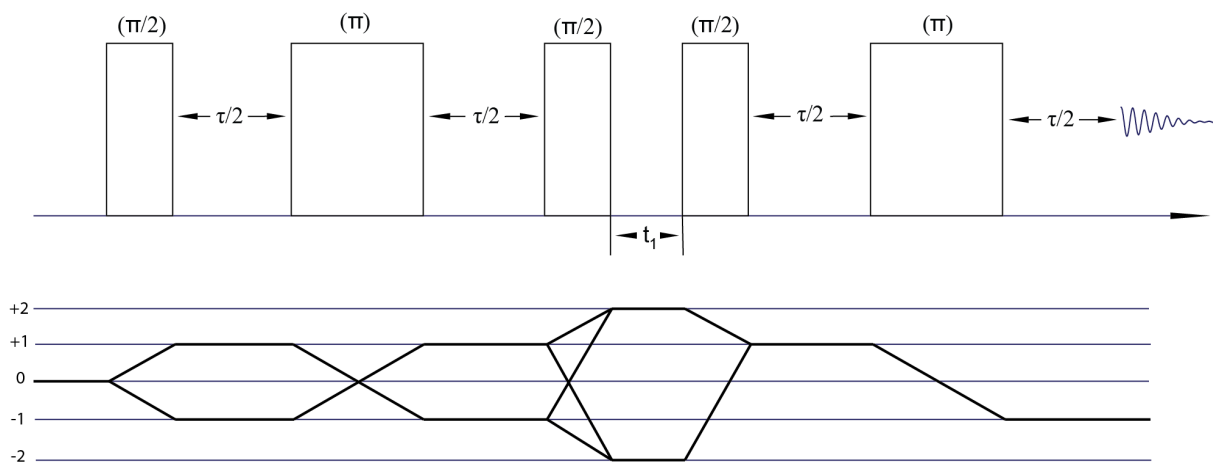


Figure 3.15: Refocused-Inadequate experiment with coherence pathway, the first spin echo creates a ±1 coherence that is then converted to a ±2 by a $\pi/2$ pulse that evolves through $t_1$. The DQ coherence is then converted to a +1 coherence before the final $\pi$ pulse refocuses the coherence to -1.

The pulse sequence consists of a spin echo followed by a 90° degree pulse that converts the ±1 coherences to DQ coherences of ±2 then after the evolution time $t_1$ the DQ coherences are converted to a +1 coherence then a 180° pulse is used to convert the signal back to the -1 coherence for detection. A sixteen step nested phase cycle is used to convert to the DQ coherence and back again. The process for the 2D experiment is the same as that from before and with the Fourier transform in both dimensions will give a plot with chemical shift on the $f_2$ dimension and with corresponding peaks at $f_{2a} + f_{2b}$ on the $f_1$ dimension.

There are problems associated with this type of experiment, determining the echo

spacing can be problematic, as it is related to the J-coupling by

$$\tau = \frac{1}{2J_{IS}} \tag{3.18}$$

if the signal is weak it is not possible to refine this value very easily and estimations may have to be used. Likewise, if there are many different sites, the J-coupling can vary quite a bit, and the various sites will be excited differently, so excitation of the various sites might be uneven [44]. However in the work presented in this thesis the experiment was not used to determine the value of J-couplings or what signals corresponded to what J-coupling. The experiment was used as a means to prove the existence of through bond connectivity in the sample, hence the experiment was done as a one dimensional experiment and $t_1$ was fixed, and the end result would be determined through the existence of signal or not.

### 3.5.4   Cross Polarisation and CP HETCOR

While cross polarisation (CP) experiments have not been performed as 1D experiments in this thesis, as is their more common use, where CP is used to enhance more diluted spins [74]. Cross polarisation is however, the basis of the heteronuclear correlation experiment (HETCOR) experiment [75], and therefore requires an explanation of the process involved.

Cross polarisation is a widely used technique in magnetic resonance to enhance the signal of dilute or low natural abundance spins, by transferring the magnetisation from a more abundant spin in the network. This is most commonly done by transferring from protons, which have a large magnetic moment, but can be done with any abundant nuclei [51]. However the experiment can have varying degrees of difficulty for nuclei with spin $I > \frac{1}{2}$ [45]. In the work within CP was form the $^{31}$P nuclei to the less abundant $^{29}$Si nuclei, while not impossible, it is not really a standard technique due to the weak dipole coupling between the nuclei. In general the signal enhancement that is achievable in a CP experiment can be considered to be a ratio of $\gamma_I/\gamma_S$ for the two nuclei involved, where $\gamma_I$ is that of the more abundant spin. As the transfer mechanism is related to the dipolar coupling, sites that are close are going to be enhanced more

than those further away, therefore it is possible to tell which sites are closer in space than others, it can also be used to exclude sites that don't take part in the process as those are phase cycled out.
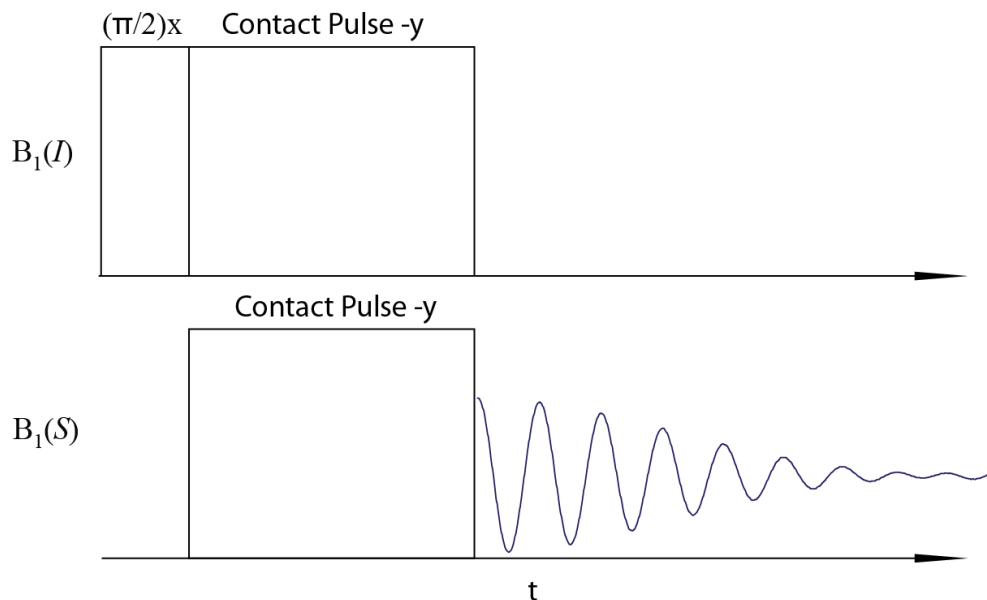


Figure 3.16: Pulse sequence for cross polarisation, an initial $\pi/2(x)$ pulse rotates the $I$ spins to the $x$-$y$ plane, a successive $y$ pulse locks the magnetisation from the $I$ spins, the $S$ spins are then brought into contact for the Hartmann-Hahn match condition, before detection on the $S$ channel.

The theory behind the technique is reasonably complicated [45,50,51,76], especially when MAS is involved, so only a basic explanation is given here. The CP pulse sequence (see Figure 3.16) uses what is called spin locking, spin locking involves an initial $x$ pulse $\mathbf{B}_1(\text{I})$ to rotate the magnetisation of the more abundant spin $I$ onto the $y'$ axis of the rotating frame, if a second $\mathbf{B}_1(\text{I})$ pulse is immediately applied so that it points along the $y'$ direction and is sufficiently strong enough the magnetisation will remain along $y'$ as it is not free to precess around $z$ and will only precess around the effective field $\text{B}_{eff}$ which is along $y'$ and is therefore said to be locked, and the magnetisation will stay locked for how long the pulse is applied for. However, the magnetisation will eventually decay, as the $\mathbf{B}_0$ field being much stronger will still cause the magnetisation to relax back along $z$ this is given the time constant $\text{T}_{1\rho}$. If a pulse $\mathbf{B}_1(\text{S})$ is applied to the dilute spins at the same time as the spin lock pulse so that the separate spins are brought into thermal contact, this is done by using what is called the Hartmann-Hahn

(H-H) match condition [76]

$$\gamma_I B_1(I) = \gamma_S B_1(S) \qquad (3.19)$$

It can be seen from Equation 3.19 that the energy transition between the upper and lower levels of the Zeeman splitting for the two spins is now the same, and as the energy of the magnetisation for spin $I$ was created by the $\mathbf{B}_0$ spin system then it is too large to be sustained by the $\mathbf{B}_1(I)$ field and will decay. However as the spin system is now coupled to the $S$ spins, energy is conserved, as the $I$ spin system decays it redistributes energy and the $S$ spin system will now also adjust its energy, and as there is no net loss in the system, the $S$ spins gain a large polarisation along the direction $\mathbf{B}_1(S)$.

There are other advantages to using the CP process, as the $T_1$ of many dilute spins can often be long, the whole cross polarisation process can use the $T_1$ of the more abundant spin system. Furthermore, it is not always necessary to use a completely relaxed system for the $I$ spins, as the magnetisation can still be enhanced as long as there is sufficient build up of longitudinal magnetisation before the transfer takes place. The length of time there needs to be contact between the pulses varies due to the distances and the nuclei involved, and hence the strength of the dipolar coupling. In different systems the contact time can vary from milliseconds to tens of milliseconds, the former are not a problem, however when long contact times are involved, this puts a large amount of stress on the $rf$ circuit, $T_{1\rho}$ can also become a factor and the polarisation transfer might be insufficient, due to the magnetisation not staying locked long enough for the spins to come into contact. Spinning fast can also complicate matters as dipolar coupling is removed or certainly reduced by rapid spinning, this leads to a loss of efficiency in the CP process. [45, 51]

The CP HETCOR [75] experiment is essentially an extension of the 1D experiment (see Figure 3.17). As with the R12$_2^5$ pulse sequence a saturation comb was used to make sure that the $^{31}$P longitudinal magnetisation was the same before each acquisition. The difference between the HETCOR and the CP is fairly straight forward, and it can be seen that instead of having the initial $\mathbf{B}_1(I)$ pulse immediately before the lock pulse, it is incremented in steps away from the lock pulse over each subsequent data set as
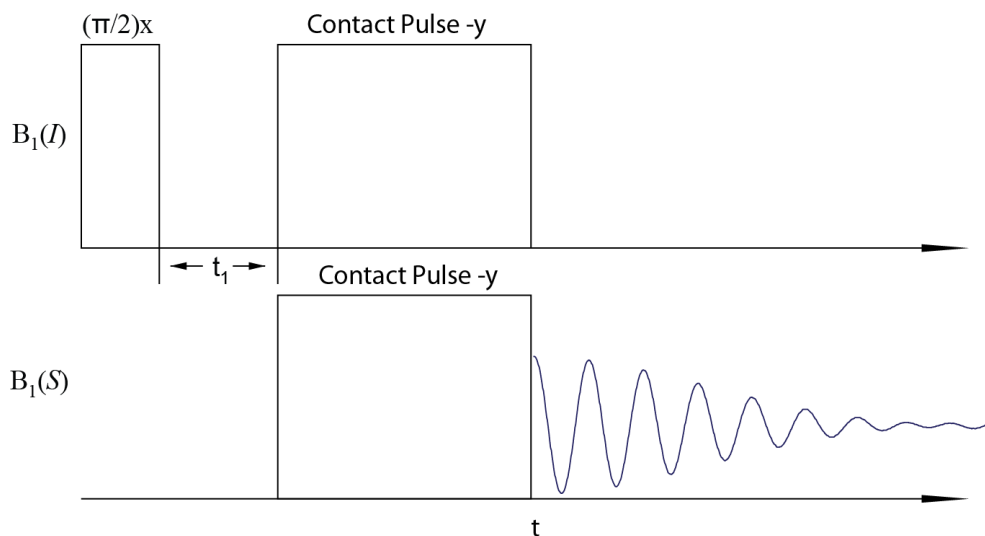
Figure 3.17: The CP HETCOR experiment is very similar to the CP experiment except that the time $t_1$ between the initial $I$ pulse and the lock pulse is incremented between each successive data set.

with the other 2D sequences, so that the $I$ spin frequencies are allowed to evolve before the CP transfer takes place, if no increment takes place it is just the 1D one pulse. In addition to this the pulse that is used on the $\mathbf{B}_1(S)$ channel has a variable amplitude contact pulse [77] in order to improve the efficiency of the H-H match. The first pulse has a phase cycle of two, whereas the $S$ contact pulse has a phase cycle of eight steps, ensuring that isolated peaks are not visible in the final spectrum. The final Fourier transformed 2D spectrum gives chemical shift information for the observed nucleus in the $f_2$ dimension, and the chemical shift of those spins where the magnetisation was transferred from is along the $f_2$ axis.

# Chapter 4

# $^{31}$P MAS NMR Studies of $\alpha$-TCP, with First Principles Calculations

## 4.1 Introduction

Synthetic calcium phosphate materials generate significant interest in the field of biomaterial research [23]. They exhibit both chemical and structural similarities with the calcium apatite like phase that makes up the mineral component of bone, this mineral phase accounts for approximately 75 % of the bone structure with the other 25 % making up an organic phase [10]. This calcium apatite phase is best described as a form of hydroxyapatite (Ha, $Ca_{10}(PO_4)_6(OH)_2$) [21], though it is not"pure"and is found to contain many elements in various quantities [11]. Some elements are only found in trace amounts such as $Sr^{2+}$,$Cu^{2+}$, $Pb^{2+}$ [11], while other elements make up a more substantial part of the phase $Mg^{2+}$, $Na^{2+}$ [12]. Bone is not inert and continuously grows just like any other tissue in the body, it does this by undergoing what is called 'remodelling', this is where bone is continuously broken down by the body through a process known as resorption, whilst new bone grows in its place [13].

Amongst other materials many calcium phosphates are used as biomedical implants, for as well as being similar in chemical composition and structure they are also bioactive; this means they interact in a positive way with surrounding tissue when implanted in the body [78]. They are also potentially resorbable, where they are broken down over

time through dissolution or through resorption [2]. These implants can take the form of dense materials, used as coatings for metal implants, where the coating helps fix the metal implant, such as fixing a replacement hip joint in place allowing the existing bone and implant to grow together [79, 80]. Calcium phosphates are also used as bone cements, to help repair extensively damaged bone by filling cavities or defects, these materials are generally highly porous and existing bone grows through the implant, and the implant may eventually be replaced by natural tissue [5].

In recent years tricalcium phosphate (TCP, $Ca_3(PO_4)_2$) has shown increasing interest as a biomaterial, as it demonstrates both good bioactive and resorbable characteristics [17]. There are three poly-morphs of TCP, namely $\beta$ [81], $\alpha$ [1] and $\alpha$' [82], though the $\alpha$' phase is of little practical interest and only forms at temperatures over 1430° C, and reverts back to the $\alpha$ phase when cooled below the transition temperature [82]. While $\alpha$ and $\beta$ TCP share the same chemical composition they differ considerably in structure, density and solubility [31], leading to quite different biological properties and applications. The $\alpha$-TCP structure contains a lot of channels and as such is a much more open and less dense material. Both $\beta$-TCP and $\alpha$-TCP find clinical use in dentistry and orthopaedics and come in the form of dense blocks, granules and fine powders for bone cements though $\alpha$-TCP is more likely to be found as the later since it is the more soluble and reactive of the two polymorphs [17]

As mentioned above $\beta$, and $\alpha$-TCP share the same chemical composition, though there is where the similarities end as they posses very different structures. $\beta$-TCP can be considered to be the low temperature phase and $\alpha$-TCP its high temperature analogue. $\beta$-TCP is the more extensively studied of the two phases, however this is more likely due to its ease of synthesis compared to that of the $\alpha$ phase, rather than because of any perceived relative importance. $\beta$-TCP is found to be stable at room temperature up to 1125° C and crystallizes in the rhombohedral space group R3c with lattice parameters $a = 10.439(1)$, $c = 37.375(6)$ Å and Z = 21 [81]. In contrast the $\alpha$ phase is only metastable at room temperature, and if TCP is annealed above 1125° C it transforms into the $\alpha$ phase , and special measures have to be taken for cooling, as the structure can revert back to the $\beta$ phase when returning back through this phase transition temperature [83]. Either the sample has to be cooled carefully, or more

often, quenched quickly to freeze the $\alpha$ phase in place [84]. $\alpha$-TCP crystallises in the monoclinic space group P2$_1$/a with lattice parameters $a = 12.887(2)$, $b = 27.280(4)$, $c = 15.219(2)$ Å, $\beta = 126.20(1)°$ and Z = 24 [1].

A more detailed look at the results from the literature show that the studies are limited to unit cell parameters and refinements with fixed atomic positions, and so conjecture does exist [85, 86], nevertheless Rietveld refinements of these parameters from X-ray diffraction data are in good agreement with the single crystal structure determined by Mathew $et$ $al$ [1] as is the computational study of $\alpha$-TCP [87]. There exists only one $^{31}$P MAS NMR study on $\alpha$-TCP [34] and is not so satisfying, they claim evidence of fifteen $^{31}$P resonances from $\alpha$-TCP, and attribute these to the structure by Mackay [88] which has sixteen independent phosphorous sites. However the structure proposed by Mackay was found to be incomplete, and was shown by Mathew $et$ $al$ [1] that what Mackay had found was only a third of the actual unit cell with $b = b/3$, and that the full structure has twelve crystallographic independent phosphorous sites. Therefore it is expected that only a maximum of twelve resonances should be observed and reducing the unit cell to that of the incomplete one found by Mackay would not change this, so undoubtedly some other factor has to explain the extra three peaks, such as impurities or some kind of error.

## 4.2    Crystal Structure $\alpha$-TCP

The crystal structure of $\alpha$-TCP was first proposed by Mackay [88] with the structure being a monoclinic unit cell with $a = 12.86$, $b = 9.11$, $c = 15.23$ Å, $\beta = 125.2°$ and space group P2$_1$/a. Further investigations by Mathew $et$ $al$ [1] found the solution by Mackay to be incomplete. Showing that what Mackay had found, was actually a sub cell of the complete structure with $b = b/3$ and that the structure determined by Mathew $et$ $al$ had $a = 12.88$, $b = 27.28$, $c = 15.21$ Å and $\beta = 126.2°$ and space group P2$_1$/a.

The packing of the atoms in the unit cell is quite complex (see Figure 4.1), each unit cell consists of eighteen distinct calcium sites, twelve phosphorous and forty eight oxygen sites, each site has a multiplicity of four making up a total of twenty four Ca$_3$(PO$_4$)$_2$
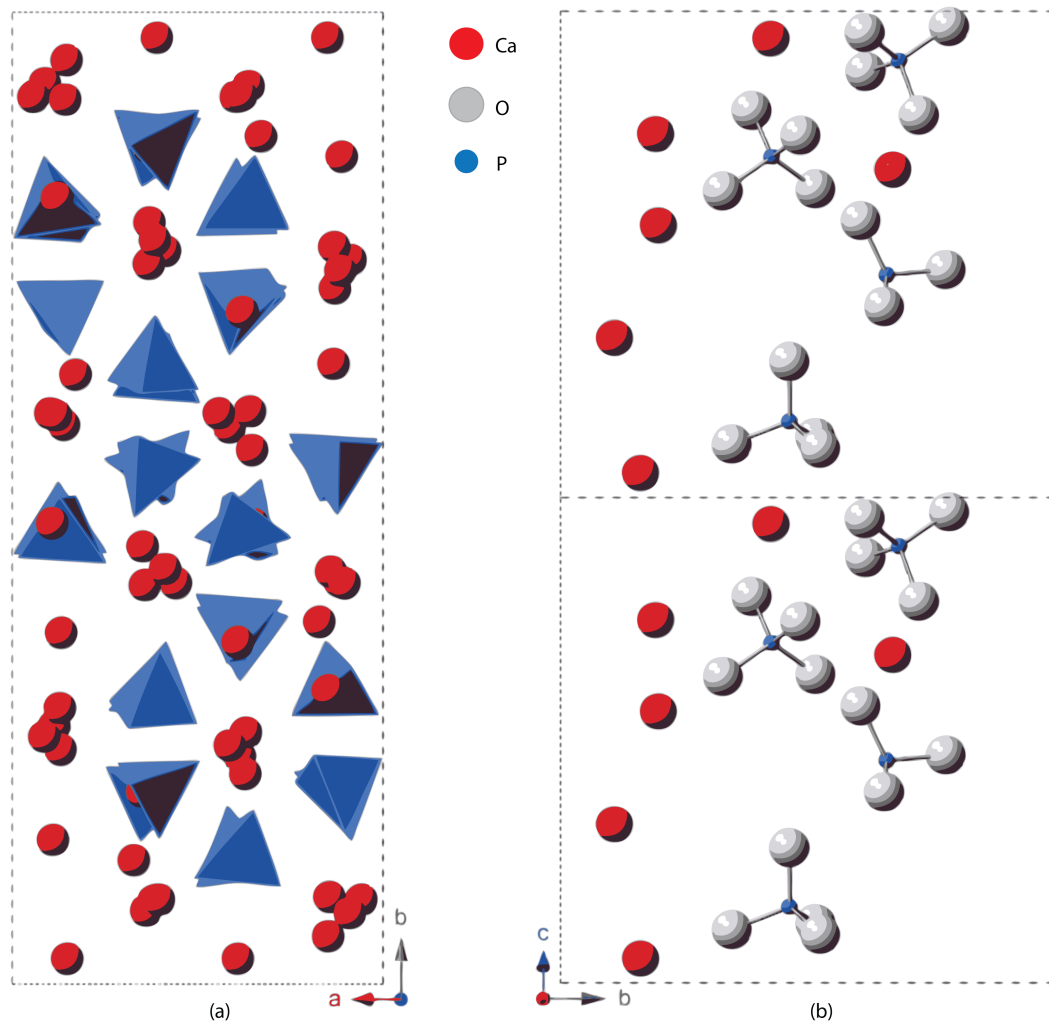
Figure 4.1: Shows the unit cell arrangement for $\alpha$-TCP from Mathew *et al* [1] (a) viewed along the $c$ axis showing the arrangement of cation and cation-anion columns and (b) showing the distorted nature of the cation columns and the vacancies that occur in the cation-anion columns.

units per cell. The structure is best described as being arranged as columns lying along the direction of the $c$ axis. These columns take two forms, namely cation–cation columns and cation-anion columns, where each cation-cation column is surrounded by six cation-anion columns, and the cation-anion columns are surrounded by alternating cation-anion columns and cation-cation columns giving a total of six columns, forming a pseudo-hexagonal pattern (see Figure 4.1a)

There are three distinct cation-cation columns consisting of the repeat units Ca3-Ca2-Ca4-Ca5, Ca9-Ca8-Ca10-Ca11, and Ca15-Ca14-Ca16-Ca17. Likewise there are six independent Cation-anion columns, P12-Ca1-P11, P10-Ca18-P9, P8-Ca13-P7, P6-

Ca12-P5, P4-Ca7-P3 and P2-Ca6-P1 each cation-anion column has a missing cation ']' between the anions of each repeat unit to form moieties such as P12-Ca1-P11-[]-P12, Mathew *et al* [1] called this missing site a vacancy (see Figure 4.1b) due to the similarity with the structure of Glaserite [89], where this vacancy is occupied by a cation. The cation columns are quite distorted from a straight line and the distortion is generally in the direction of one of the vacant sites, in one of the surrounding cation-anion columns, (see Figure 4.1b). In addition to these vacant sites in the unit cell there also exists some quite large channels running through the structure, which explains the lower density and the high rate of solubility of this material in comparison with the beta form (see Figure 4.2).
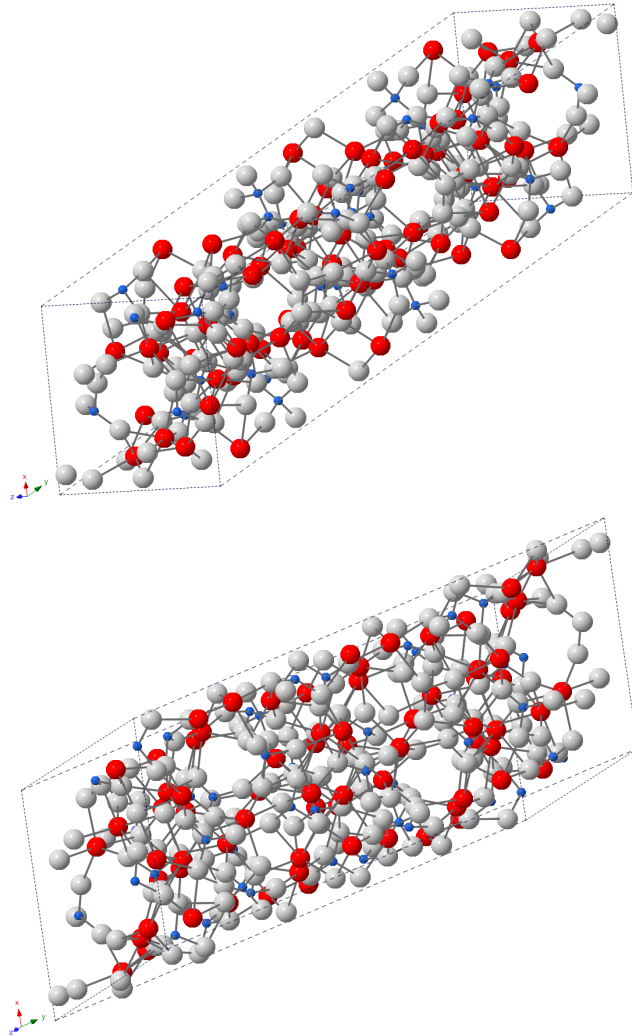


Figure 4.2: Two different orientations of the $\alpha$-TCP unit cell, demonstrating the large channels that are found throughout the structure.

## 4.3 Experimental

### 4.3.1 Sample preparation

The solid-state synthesis of the $\alpha$-TCP samples was undertaken by Dr. Jo Duncan from the University of Aberdeen using similar routes to those previously accomplished in the literature [1, 90, 91]. $\alpha$-TCP synthesis involved the thermal decomposition and subsequent solid-state reaction between a homogenised 1 : 2 molar mixture of $CaCO_3$ and $CaHPO_4$. The $CaCO_3$ was reagent grade (99%+ Sigma Aldrich, UK ) and the $CaHPO_4$ (monetite) was synthesised in-house to ensure chemical purity and the true identity of this product. Powders were homogenised in acetone using a mortar and pestle until a homogeneous paste was formed; this paste was then dried at 80°C to remove excess acetone prior to high temperature heat treatment. The mixed powders were then put into platinum crucibles and heated to 1300°C in a muffle furnace (Carbolite, UK) for a period of 8 hours which was followed by a rapid quenching in air. These samples were then re-ground and re-heated to 1300°C for another 8 hour period followed by another quenching step in order to retain the $\alpha$-polymorph. This step was found to be less important for chemically pure samples. The overall phase purity was checked using a Bruker D8 Advance diffractometer, against ICDD card No. 09-348.

### 4.3.2 Calculations

. The theoretical density functional theory (DFT) studies of the $\alpha$-TCP and Si-$\alpha$-TCP systems were undertaken by Dr. David Quigley from the University of Warwick. This involved programs from Accelrys Software, implemented in the Materials Studio 5.5 suite. [92] The periodic plane-wave, pseudopotential-based CASTEP code [93] was employed in this study, which employed a generalized gradient approximation (GGA) treatment of electronic exchange and correlation. Specifically, the functional of Perdew, Burke and Ernzerhof (PBE functional) was employed. [94] Energy minimisation and geometry optimisation tasks were performed on both $\alpha$-TCP and Si-$\alpha$-TCP using unmodified ultrasoft pseudopotentials generated directly from the Materials Studio package, with the exception of that used for Ca. This employed an ad-hoc 3.2

eV shift in the energy of the 3d orbitals in order to be consistent with the calcium oxide (CaO) calculations of Profeta et al [95]. A basis set convergence of 0.04 mH per atom (total energy) was achieved with a plane-wave cut-off energy of 670 eV and a sampling of two k-points within the 1st Brillouin zone. At this level of representation, atomic forces were found to be converged to 0.0001 eV/Angstrom. A resulting estimate of basis set truncation error in optimized structural parameters is less than 0.01 Angstrom. GIPAW-DFT calculations [96,97] based on these optimized structures were subsequently invoked to compute the $^{31}$P, $^{29}$Si and $^{43}$Ca chemical shielding and quadrupolar NMR tensors and thus establish a direct link between the P and Ca structure (cif) file positions and the high resolution solid state NMR data characterising the $\alpha$-TCP structure, and to elucidate the precise position of the Si incorporation in the Si-$\alpha$-TCP structure. All plane-wave CASTEP calculations were performed using the HECToR high-performance computing cluster.

### 4.3.3   Solid State NMR Experiments

All $^{31}$P MAS experiments were performed at 11.7 T ($\nu_0$ = 202.4 MHz ) on a Bruker Advance III, 500 MHz spectrometer. These $^{31}$P experiments were enabled using a Bruker 4mm HXY probe (shimmed to 2 Hz). Single pulse $^{31}$P data were acquired using a tip angle of $\pi/2 = 4\mu$s, a recycle delay of 480 s (4 acquisitions) spinning at 12 kHz.

$^{31}$P-$^{31}$P R12$_2^5$ data were undertaken using a Bruker 4 mm HXY probe with $\pi/2 = 7\mu$s, The B$_1$ field was rotor synchronized to three times the MAS frequency of 11900 kHz and using an X nucleus amplifier level of 13.6 db; a recycle delay of 60 seconds, 256 F1 increments and 32 scans per increment were used in conjunction with a re–coupling loop $l_0 = 50$. A preceding saturation comb was also employed using 35 $\pi/2$ pulses and a 50 ms delay between them. This experiment was repeated using the same parameters except the recycle delay was reduced to 30 seconds and the loop counter shortened to $l_0$ = 20. Short recycle delays were required to give the optimum signal per unit time and experimental performance as the acquisition time per slice was long and truncation in the f$_1$ dimension had to be avoided.

All $^{31}$P chemical shifts were calibrated to the secondary solid $NH_4H_2PO_4$ reference material which is measured at 0.9 ppm with respect to the primary IUPAC standard of 85% $H_3PO_4$ ($\delta$ 0 ppm). The deconvolution of 1D spectra was performed using the DMFit [98] software and the analysis of all 2D data was undertaken using Bruker Topsin 2.1.

## 4.4 Results and Discussion

### 4.4.1 $^{31}P$ MAS NMR Studies of $\alpha$-TCP

The $^{31}$P solid state MAS NMR spectrum for $\alpha$-TCP is shown in Figure 4.3a. This data consists of twelve resonances approximately 0.08 ppm full width half height (FWHH), which span a small chemical shift range of $\approx$ 4.5 ppm, and can be classified as isolated $Q^0$ phosphate tetrahedra lying within the expected range for calcium phosphates [99]. There is no evidence of any phosphorous moiety sharing a bridging oxygen, and this description is in full agreement with the crystal structure of Mathew *et al.* [1]. The spectrum of Figure 4.3a can be simulated and deconvoluted (see Figure 4.3b and 4.3c), into twelve resonances of approximately equal integrated intensity (see Table 4.1) , thus corroborating the model by Mathew *et al* [1] that proposes twelve equally occupied phosphorous sites; given that all twelve sites can be observed with such resolution in the solid state, and despite the size and given complexity of the $\alpha$–TCP unit cell, it demonstrates that a very high degree of short and long range order characterises the system.

The dispersion of the $^{31}$P chemical shifts shows that, while most of the P positions expectedly are similar due to the nature of the compound, there are significant observable differences for some of the sites. Other $^{31}$P MAS NMR studies have reported that there is no detectable relationship between the chemical shift , the $PO_4{}^{3-}$ tetrahedral distortion, the number of next nearest neighbours and the average bond length [99]. It is known, however, that what influences each $^{31}$P chemical shift is the identity of the next nearest neighbour. Elements such as Na, Ca, or B for example, are known to affect the range in which the various $^{31}$P chemical shifts will appear [99], however
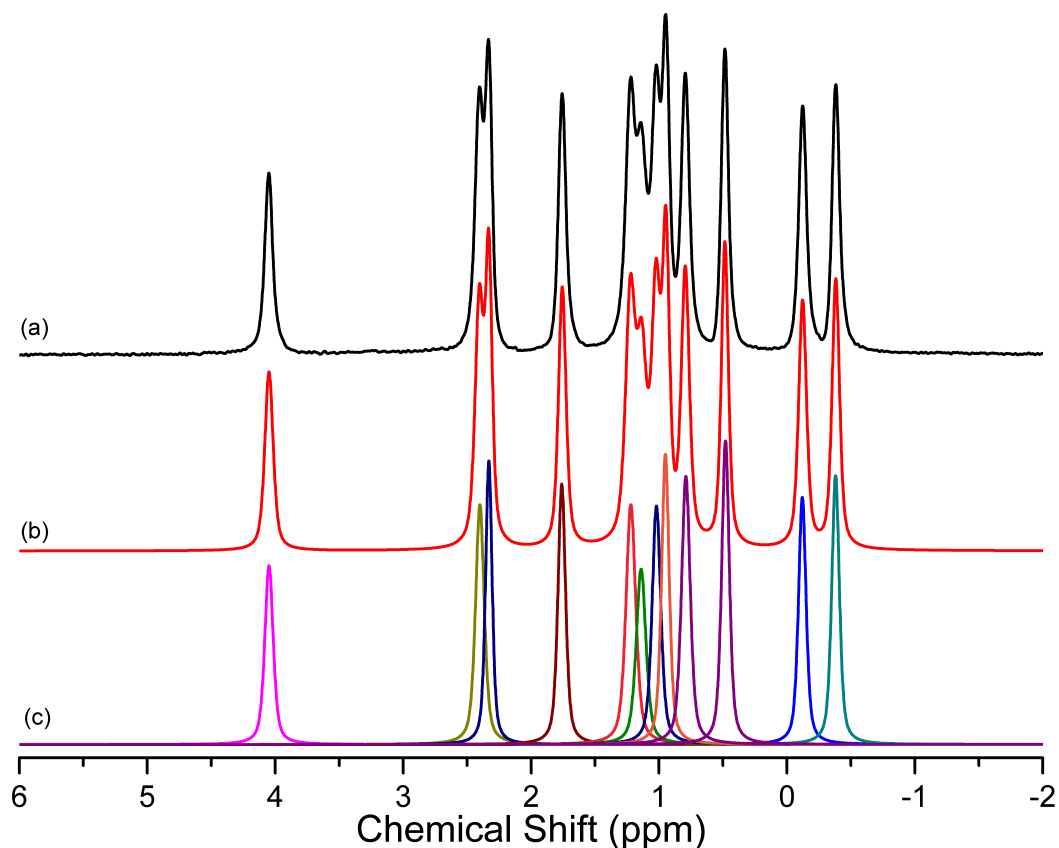
Figure 4.3: Shows the (a) $^{31}$P spectrum for $\alpha$-TCP (b) the fitted spectrum (c) and model consisting of twelve peaks.

.

this does not account for the significant differences within a particular range. It has been postulated that this phenomenon is influenced by the actual strength of each bond [100], while this is an ideal compound to test this hypothesis due to the twelve chemically similar but distinct sites, it is beyond the remit of this particular study and has not been attempted as yet.

The data shown in Figure 4.3a showing twelve P sites, disagrees markedly with the spectrum published by Bohner *et al* [34]. They assigned their $^{31}$P MAS NMR data to fifteen P sites, arguing that it was close to the expected number of sites from the crystal structure proposed by MacKay [88]. However their interpretation is questionable, as they claim that the reduction of the unit cell proposed by Mathew et al [1] (which has forty eight P sites) to that of Mackay [88] by constraining a 1/3 unit cell (i.e. $b = b/3$) will invoke a description of sixteen sites; hence sixteen $^{31}$P chemical shifts are expected. However as the sixteen site sub cell was shown to be incomplete by

Table 4.1: Results for $^{31}$P MAS NMR of $\alpha$-TCP and calculations

| $\delta_{iso}$ Expt | FWHH | Integrated intensity | $\delta_{iso}$ Calc | Crystal Site |
|---|---|---|---|---|
| 4.05 | 0.08 | 58.13 | 5.57 | P8 |
| 2.4 | 0.08 | 78.27 | 2.69 | P4 |
| 2.33 | 0.06 | 73.8 | 2.59 | P10 |
| 1.76 | 0.07 | 77.15 | 2.31 | P12 |
| 1.22 | 0.09 | 89.76 | 2.12 | P5 |
| 1.14 | 0.09 | 67.48 | 1.99 | P1 |
| 1.02 | 0.08 | 80.4 | 1.72 | P3 |
| 0.95 | 0.07 | 79.95 | 1.09 | P7 |
| 0.79 | 0.08 | 85.05 | 0.77 | P2 |
| 0.48 | 0.07 | 83.25 | 0.13 | P11 |
| -0.12 | 0.07 | 76.13 | -0.07 | P9 |
| -0.38 | 0.07 | 77.79 | -0.57 | P6 |

Mathew *et al* [1] only twelve resonances are to be expected, as each crystal site has a multiplicity of four then this will give forty eight phosphorous sites in full agreement with the crystal structure. This lack of understanding is likely to have been influenced by the poor quality of their $^{31}$P MAS NMR data. There are several possibilities for this, as instrumental effects (poor shims, miss set magic angle etc.) and/or sample purity considerations are likely to have been involved. The more probable scenario involves the presence of sample impurities, as their $^{31}$P MAS NMR data looks very similar to what is reported in Figure 4.4b.

While very good resolution is obtained in the $^{31}$P MAS NMR experiment, it is worth mentioning that this is not always the case. The high degree of short and long range order giving rise to the resolution in the solid state NMR spectrum is very much dependant on the purity of the sample. Figure 4.4 compares the spectra of high purity $\alpha$-TCP with that of other $\alpha$-TCP samples synthesised in exactly the same way but which are known to contain impurities. These impurities are often unavoidable if commercial reagents are used, especially in the monatite precursor. These impurities consist of MgO and $Al_2O_3$ for one sample(see Figure 4.4b), and another contains MgO, $Al_2O_3$ and $Fe_2O_3$, (see Figure 4.4c). While these impurities are of a low concentration, totalling less than 0.5 wt%, little effect is seen in the long range order (XRD not shown). However the short range order is somewhat more affected, with the pronounced loss of resolution attributed to localised disorder. Notably, this loss of resolution is

considerably less in the sample that does not contain Fe, and the overall manifold of resonances is preserved throughout. The spectrum in Figure 4.4b is very similar to the one reported by Bohner *et al* [101], and the presence of impurities is likely to be the reason why they report such poorly resolved data. In contrast, the sample that contains the Fe impurity has lost a significant amount of the overall resolution. Whether this is due to increased disorder is not clear, however it is well known that the presence of Fe in a sample can have significant detrimental effects on the resolution of solid state NMR data due to the occurrence of unpaired electrons in the structure, thus resulting in what is called paramagnetic broadening [102].
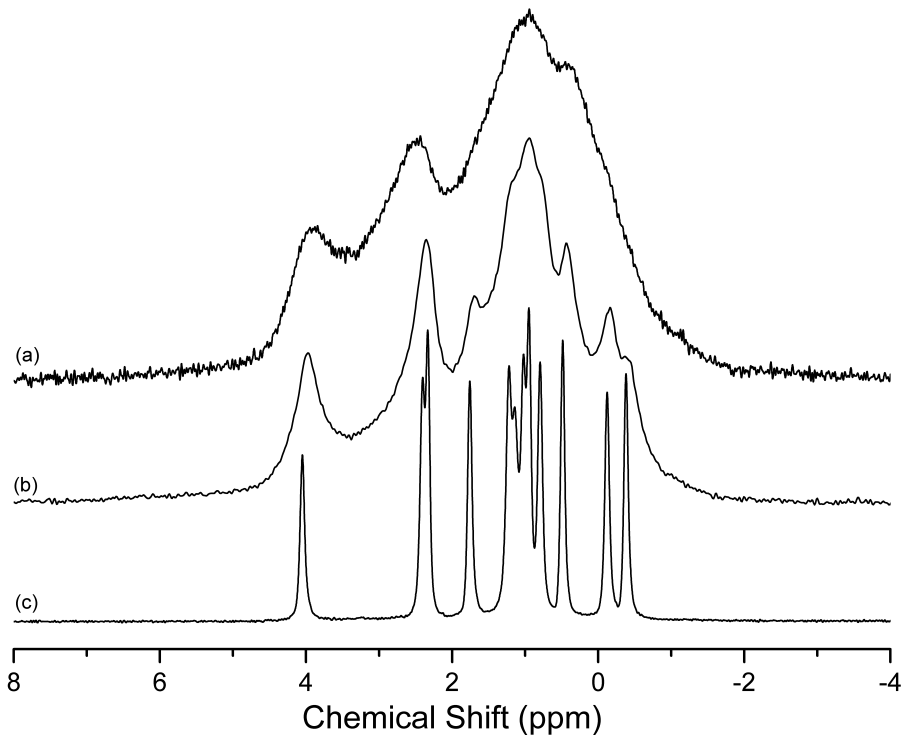


Figure 4.4: $^{31}$P spectra for $\alpha$-TCP preparations with different levels of impurities. (a) containing MgO, Al$_2$O$_3$ and Fe$_2$O$_3$ (b) containing MgO and Al$_2$O$_3$ and (c) no detectable impurities

A comparison of the experimental data acquired from the pure $\alpha$-TCP with the data from the corresponding GIPAW DFT calculation (see Figure 4.5a), shows that a reasonably good agreement exists. The calculated data was referenced to the experimental data by plotting shielding ($\sigma$) against shift ($\delta$) ( see Figure 4.5 b), similar to

the method described by Johnston *et al* [103]. Then using the equation

$$\delta_{iso} = -1(\sigma_{cal} - \sigma_{ref}) \qquad (4.1)$$

where $\sigma_{iso}$ is the calculated isotropic chemical shift, $\sigma_{cal}$ is the nuclear shielding value given from the calculations for each site and $\sigma_{ref}$ is the nuclear shielding value given by the slope.

While the calculated shifts are not in exact agreement with the experimental data, and the calculated chemical shift range is slightly larger than the observed distribution of the resonances, the central theme of eleven of the lines constituting the group with one explicit outlier is preserved. The advantage these calculations is that they facilitate the assignment of the various resonances to the different P positional sites in the structure. However, these calculations exhibit only a broad agreement with the experimental data and it is not possible to use this method on its own to state with certainty that this method necessarily predicts the correct assignments. In particular, there is no way of knowing if some of the sites have had their order switched around by the calculations. The predominant problem is that the high resolution experimental data which exhibits chemical shifts less than 0.1 ppm apart is truly testing the accuracy of the GIPAW DFT approach, and the large yet highly ordered $\alpha$-TCP structure is providing the most difficult test relating to computation of $^{31}$P NMR interaction parameters as yet reported. As will be demonstrated in Section 4.4.2 below not all of them are correct, but this approach does provide this study with a useful and reliable starting point. Specifically the outlying shift at 4.05 ppm which can be stated to correspond to crystallographic site number P8, and the subsequent ordering of the peaks predicted by the calculations are summarised in table 4.1.
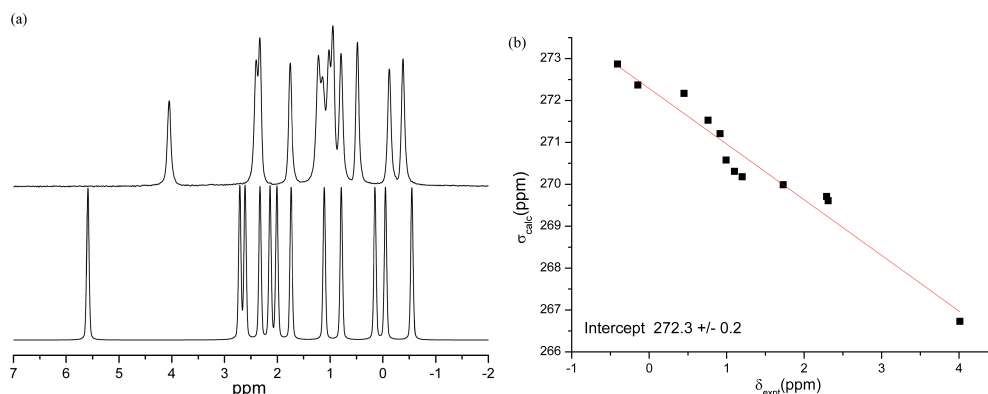
Figure 4.5: (a) $^{31}$P MAS NMR comparison of $\alpha$-TCP experiment and first principles GIPAW DFT calculations, showing a reasonable agreement between the two (b) plot showing calculated shielding against measured chemical shift to determine a reference shielding for the calculations

## 4.4.2  $^{31}$P DQ NMR Experiments of $\alpha$-TCP

While 1D MAS NMR provides information about the different structural species and the nature of the chemical environments in a material, more complicated techniques are required to determine things like atomic distances and connectivity within those materials. In order to be able to interpret and understand the connectivity between the P and Si in the substituted Si-$\alpha$-TCP structure presented in Chapter 5.3.6, it is necessary to understand how the different chemical environments relating to P manifest themselves in the underlying crystal structure of un-substituted $\alpha$-TCP. By understanding the *connectivity* between the various P sites it is possible to precisely determine which $^{31}$P chemical shifts are attributed to each crystallographic position, and hence this information can be used to rationalise which P sites interact with nearby Si in the Si-$\alpha$-TCP structure. While the DFT calculations in Section 4.4.1 did assign resonances to shifts, there was no way of knowing if they were correct, and they have to be subsequently proved/disproved by further experiment. In order to look at the $^{31}$P–$^{31}$P connectivity in $\alpha$-TCP, 2D double quantum dipolar re-coupling experiments were performed using the R12$_2^5$ pulse sequence (see Section 3.5.2). Under MAS conditions the homonuclear dipolar coupling is removed, however by using specific pulse sequences it is possible to selectively reintroduce it. This allows a 2D spectrum to be constructed describing how the P sites are interacting with each other, and thus describing their

82
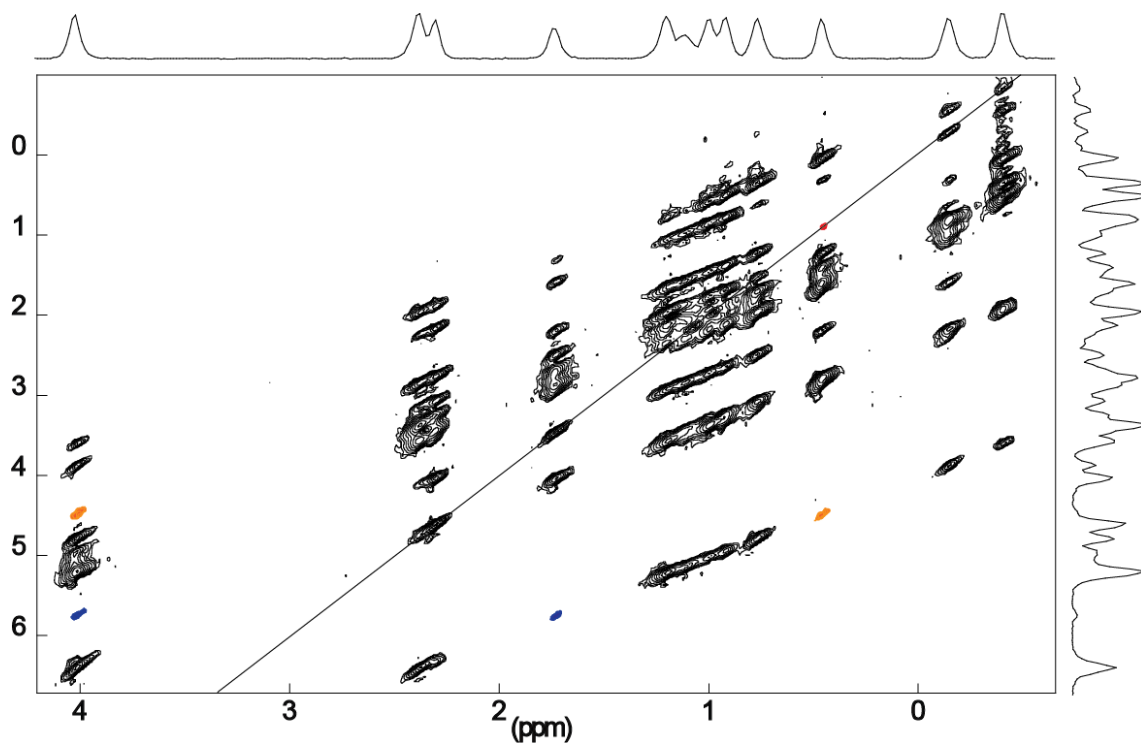
Figure 4.6: R12$_2^5$ $^{31}$P–$^{31}$P correlation with 50 re-coupling loops for $\alpha$-TCP, resonances appear between coupled spins at f$_1$ = f$_2$a + f$_2$b where f$_2$a and f$_2$b are non equivalent sites (blue or orange peaks) and are found at an equal distance either side of the spectrum diagonal (black line) any site on the diagonal (red peak) is a coupling between equivalent spins such that f$_2$a = f$_2$b.

spatial proximity to each other. This information can then be compared to the crystal structure, to determine what resonances are related to each crystal site.

The results for $\alpha$-TCP are shown in Figure 4.6. The normal $^{31}$P chemical shift information is contained in the f$_2$ dimension ($x$ or ppm axis), while the f$_1$ dimension contains the information about the connectivity ($y$ axis). A DQ resonance will only appear in the spectrum amongst those spins that have a dipole connection between them. Thus, a resonance will appear at f$_1$ when there are corresponding resonances at f$_2$a and f$_2$b from non-equivalent sites a and b such that f$_2$a + f$_2$b = f$_1$. Two examples of this phenomenon have been marked in orange and blue on Figure 4.6 to illustrate this connectivity. These resonances will be equidistant from what is called the spectrum diagonal, represented by the yellow line on this spectrum. Any resonances that lie on the diagonal will only represent one resonance on the f$_2$ axis, as these signals are due to correlations between equivalent sites and have equal frequencies f$_2$(a,b) [104]. From
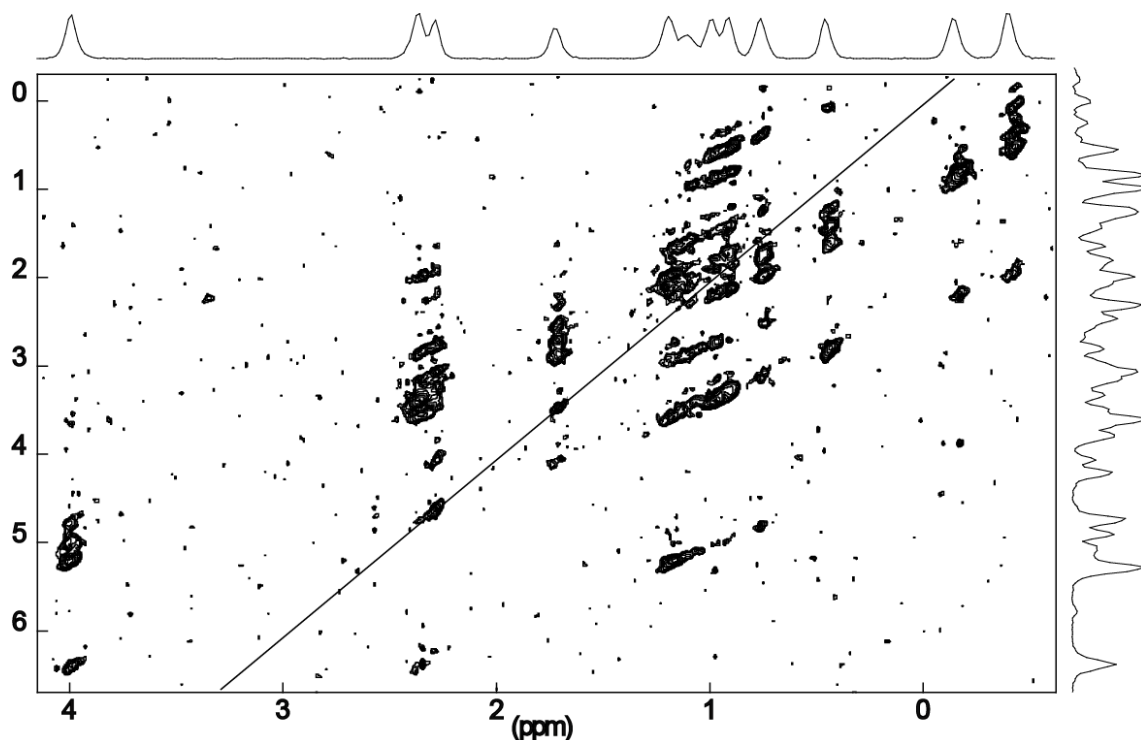
Figure 4.7: The R12$_2^5$ $^{31}$P–$^{31}$P DQ experiment repeated with 20 re-coupling loops, the lower signal-to-noise is caused by a reduced pulse delay to shorten experimental time, however it can be seen that there are significantly less correlations, making assignment of the crystal sites an easier task

the results of Figure 4.6 a large number of correlations for each site can be observed. Assigning the different resonances to the different crystal sites, though far from a trivial process, is just a case of matching up the connectivity with the relation to the nearest neighbours in the crystal structure.

The 2D double quantum R12$_2^5$ dipolar re-coupling experiment employed in this study was implemented with both long (50) and shorter (20) re-coupling periods. From the long re-coupling time experiment (see Figure 4.6) correlations between sites as far away as 6.9 Å (blue correlations) and 6.7Å (yellow correlations) can be observed. In addition dipolar couplings between atoms that were separated by up to 8.9 Å or more can also be observed; this is confirmed by signals appearing on the diagonal that correspond to crystal sites 8.9Å apart, and is illustrated by the red resonance on the diagonal in Figure 4.6 This version of the experiment resulted in all twelve P sites being coupled to just about every other P site in the $\alpha$-TCP structure, making it impossible to differentiate the connectivity between various sites. At a radius of $\sim$ 7Å from most

P positions, most other crystal sites are encompassed within this distance and $^{31}$P–$^{31}$P coupling extending to ten or twelve other sites would be experienced. The problem was further compounded by two or three of the same P crystal position being located within this radius, albeit at different distances. When these multiple equivalent sites were excited they would distort the intensities, making it impossible to determine the spatial proximity of some sites to others in space, or determine if the intensity was due to only one correlation, or if in fact the intensity was due to two or three equivalent sites interacting. Subsequent attempts at this experiment with a significantly reduced re-coupling time, has resulted in selectively eliminating some-long range correlations and thus produced a more useful result(see Figure 4.7). Although the signal-to-noise is reduced due to pulse delay and re-coupling time considerations, a comparison of the two different experiments now demonstrates it was possible to deduce what 2D correlations are associated with each 1D $^{31}$P chemical shift. At the shorter contact time it was found that not only were there a lot less correlations, but the intensities were found to be more indicative of the distance between the corresponding sites. Very weak intensities were found to correspond to P-P distances just over 5 Å, and the strongest intensities corresponded to those around 4.1 Å.

By using the intensities from the second experiment as a starting point and expecting that most resonances only have 4-5 correlations, and by a direct comparison to the first experiment, it was possible to determine the total connectivity within the α-TCP structure. The closest correlating peaks in the structure are outlined in Table 4.2 and are illustrated in Figure 4.8. Figure 4.8 however is an adapted version of figure 4.6 generated by the first experiment, and is used for illustrative purposes only. It makes for a clearer picture of the connectivity and the intensities do not reflect the actual distances. By using the four red correlations in Figure 4.8 associated with the $^{31}$P shift at 4.05 ppm as an absolute starting position it can be observed that the resonances horizontally across from them at 2.4, 1.22 1.14 and 0.79 ppm in the $f_2$ dimension are the sites that have a dipolar coupling with the 4.05 ppm position. The 4.05 ppm resonance corresponds to site number P8 in the crystal structure, the site at 1.22 ppm is the most intense and corresponds to the nearest neighbour which is site P5 at 4.118 Å. The next nearest site P4 is at 4.421 Å and corresponds to the resonance at 2.4 ppm,

Table 4.2: Comparison of α-TCP crystal sites from calculated and determined by experiment, showing all correlations and distances for those sites that are less than 5Å, P-P distance, from [1]

| Crystal sites from calc | P8 | P4 | P10 | P12 | P5 | P1 | P3 | P7 | P2 | P11 | P9 | P6 |
|---|---|---|---|---|---|---|---|---|---|---|---|---|
| Crystal sites from expt | P8 | P4 | P10 | P12 | P5 | P9 | P1 | P2 | P3 | P7 | P11 | P6 |
| $\delta_{iso}$ | 4.05 | 2.4 | 2.33 | 1.76 | 1.22 | 1.14 | 1.02 | 0.95 | 0.79 | 0.48 | -0.12 | -0.38 |
| 4.05 | | 4.4207 | | | 4.1179 | 4.8227 | | | 4.935 | | | |
| 2.4 | 4.4207 | | | | | | 4.1855 | | | | | |
| 2.33 | | | 4.4705 | 4.9746 | 4.7005 | 4.8773 | | | | 4.6129 | | |
| 1.76 | | | 4.9746 | 4.418 | | 4.3009 | 4.7644 | | 4.9926 | | | |
| 1.22 | 4.1179 | | 4.7005 | | | | | | 4.2918 | | | |
| 1.14 | 4.8227 | | 4.8773 | 4.3009 | | | | 4.6671 | | 4.2498 | 4.9629 | |
| 1.02 | | 4.1855 | | 4.7644 | | | | | | | 4.2597 | 4.6314 |
| 0.95 | | | | | | 4.6671 | | | | | 4.5422 | 4.5578 |
| 0.79 | 4.935 | | | 4.9926 | 4.2918 | | | | | | | 4.7691 |
| 0.48 | | | 4.6129 | | | 4.2498 | | | | | | |
| -0.12 | | | | | | 4.9629 | 4.2597 | 4.5422 | | | | |
| -0.38 | | | | | | | 4.6314 | 4.5578 | 4.7691 | | | |

Figure 4.8: An adapted version of Figure4.6 the first R12$_2^5$ $^{31}$P–$^{31}$P DQ experiment to illustrate the connectivity between the various sites, as such the intensities do not reflect that of the experiment used to determine the actual connectivity

and the positions P9 at 1.14 ppm and P3 at 0.79 ppm relate to distances of 4.823 Å and 4.935 Å respectively. After the second experiment only two resonances lie on the spectrum diagonal and these correspond to site P10 at 2.33 ppm and P12 at 1.76 ppm which both reside at approximately 4.4 Å from themselves. In addition, it is observed that the 2.33 ppm signal correlates with the 1.79 ppm resonance thus confirming again that these two sites are P10 and P12 and lie 4.9 Å apart. P12 also connects to P9 at 1.14 ppm, P1 at 1.02 ppm and P3 at 0.79 ppm. Completion of this analysis for all correlations subsequently maps all connectivity in the α-TCP unit cell and confirms an absolute assignment of the 1D $^{31}$P MAS NMR spectrum which will be consistent with the α-TCP structure file nomenclature.

If the assignments of the resonances from the 1D $^{31}$P experimental data are compared to that of the DFT calculations reported in table 4.2, then this suggests that the calculations are only partially correct. A good correlation between experiment and calculation is shown for first five and the last resonances. Of the six resonances in question, five exhibit minor order swapping while the other (P9) is displaced by a shift

distance of $\sim$ 1.3 ppm. It appears that the calculations are not sensitive enough to distinguish between these small chemical shift differences, as some of these resonance are separated by less than 0.1 ppm in the experiment and have been mis-assigned.

## 4.5   Conclusions

As can be observed from the $^{31}$P MAS and $^{31}$P DQ NMR experiments $\alpha$-TCP is a highly ordered structure, and that it possible to relate the $^{31}$P solid state MAS NMR results to the crystal structure proposed by Mathew *et al* [1] with good accuracy. However it is found that the high resolution required to be able to access this data requires samples of extremely high purity. First principle calculations are in reasonable agreement with the NMR data, however the complexity and the high order of the $\alpha$-TCP structure is pushing the limits of the GIPAW DFT method and it is not possible to match the resolution of the solid state MAS NMR experiment. therefore the calculations can not be relied upon one hundred percent when such high resolution is required. When dealing with such a small chemical shift range the calculated chemical shift and crystallographic site are not assigned properly. However, the calculated data still contributes to the overall analysis of the experimental data.

# Chapter 5

# $^{31}$P and $^{29}$Si MAS NMR Studies of Silicon Substituted $\alpha$-TCP, with First Principles Calculations

## 5.1 Introduction

While calcium phosphates are of great interest as biomaterials, it is common to practice to incorporate ionic substitutions with the aim of improving the material by modifying its properties in order to tailor it to more specific applications. Like other calcium phosphates such as hyroxyapatite, the structure of TCP is accepts various ionic substitutions. These are found to have a variety of effects; from changing thermodynamic properties, altering the structural properties and rate of dissolution, along with other substitutions aimed at enhancing the bioactivity [6, 37, 87, 105]. Substitution of $Mg^{2+}$ is found to increase the thermal stability of the $\beta$ phase [106] meaning that it is stable to higher temperatures pushing up the temperature of phase transformation and can promote further densification. This is also found to a certain extent with $Zn^{2+}$ and $Sr^{2+}$ substitution [17]. On the other hand substitution of $SiO_4{}^{4-}$ for $PO_4{}^{3-}$ in TCP is found to lower the temperature of the $\alpha$ phase formation and to help stabilize the structure [86], and the inclusion of silicon in the structure is thought to have the potential to enhance bioactivity. The benefits of silicon in promoting enhanced biological

activity for bone regrowth are well known [24]. It is thought that when silicon is substituted into calcium phosphates they show enhanced biological activity. Recent studies have demonstrated that this is indeed the case and that Si-substituted materials have enhanced biological activity compared to their pure analogues [24]. This has been attributed to silicon species being released to stimulate bone regeneration. However, there is no experimental evidence to support that any silicon is being released and it remains unproven at this time [101].

Characterisation of substituted calcium phosphates is often done using a variety of techniques; the crystalline phases are identified using powder X-ray diffraction, and further characterisation of the material and composition can employ techniques such as powder X-ray and neutron diffraction structure refinements, Fourier Transform Infrared spectroscopy (FTIR), Raman spectroscopy and X-ray fluorescence (XRF) and to a lesser extent solid-state NMR(SSNMR). Despite this, there are very few studies in the literature on the crystal structure of $\alpha$-TCP or its silicon doped analogues Si-$\alpha$-TCP and the changes that take place between them. As stated before, is more probable that this is due to difficulties in synthesis of the material and while it is also true that diffraction techniques are the norm for determining crystal structures, the $\alpha$-TCP structure is very large and the interpretation of this structure when low levels of dopant are present is extremely difficult and time consuming. The location of silicon in the substituted structure is unknown and the mechanism of charge balance is poorly understood, when $SiO_4^{4-}$ nominally substitutes for $PO_4^{3-}$ the extra negative charge from the silicate unit has to be accommodated. Notionally there are only two ways that this can occur; either by the production of $O^{2-}$ vacancies or by having $Ca^{2+}$ excess in the structure as charge compensation. To date no direct experimental evidence exists for either of these mechanisms.

There are a very limited number of analytical studies on the changes to the crystal structure and mostly through X-ray diffraction techniques [85,86,107] , while this is an established method for looking at the long range order of samples it is difficult to specify the precise location of substituted silicon ions due to the large parent structure and similar X-ray scattering factors for phosphorous and silicon. Likewise, there seems to be a lack of published neutron diffraction studies on these type of systems [29]. Again,

difficulties are to be expected in finding the location/locations of the substituted silicon ions due to the number of feasible possibilities that exits. This would present a more time consuming measurement and analysis. However the results should be superior to that of X-ray diffraction due to the greater resolution between the Si and P scattering wavelengths. While diffraction techniques are suitable for looking at changes to the long range order, the ideal technique of choice in this situation would be to use solid state NMR, which is very powerful for looking at small changes to the short range order of materials. Only very limited solid state NMR studies have been reported to date; there exists only one $^{31}$P MAS NMR study on $\alpha$-TCP [34] and one on $^{29}$Si MAS NMR for Si-$\alpha$-TCP [38]. A couple of computational DFT studies exist for both structures [30, 87].

The studies that look at Si-$\alpha$-TCP show that Reitveld refinements from X-ray powder diffraction and neutron diffraction are again limited to lattice parameters and unit cells with fixed atomic positions, and they show that the overall structure remains the same (i.e monoclinic P2$_1$/a), although there are some changes to the lattice parameters upon silicon substitution. The first study by Sayer *et al* [86] based on the structure by Mathew *et al* [1] but taking an average cell with b/3 due to low quality data, showed a decrease in $a$ and an increase in the $b$ and $c$ lattice parameters, with an overall increase in cell volume. This study also suggested that the Si-$\alpha$-TCP cell becomes saturated at around 1.8 wt% silicon. The second study by Reid *et al* [85], also starts with the model by Mathew *et al* [1] and demonstrates that between 0.59 wt% and 1.14 wt% silicon incorporation, an initial decrease in the $a$ lattice parameter is observed in comparison to $\alpha$-TCP, however it starts to increase again with further increased silicon content. They also report an increase in $c$ but no overall trend with silicon content, while $b$ shows increasing length with Si content and there is an increase in volume with Si content. However there are differences between the studies, the second study shows a greater overall increase in the lattice parameters when comparing equal levels of silicon substitution, compared to those in the first study, this is put down to differences in the preparation method between the samples, it is worth noting that these differences could also arise from the quality of the data between the two studies, as that in the second study is of considerably higher quality than that in the first study. Unfortu-

nately out of the nine samples looked at in their second study, they only have three data points below 1.14 wt%, when everything plateaus, they put this plateau down to an increasing hydroxyapatite phase that is forming, and that no more silicon is being incorporated into the Si-$\alpha$-TCP phase. A refinement of one sample from neutron data by Gomes *et al* [29] was in agreement with the other studies, as far as changes to lattice parameters are concerned, however they take the study no further than this.

Studies by Duncan *et al* [107], show that for a range of phase pure samples between 0wt% and 0.8wt%, the *a* lattice parameter shows a decrease once silicon is present. Though there is no specific trend, there is an overall increase in *a* when the level of silicon is increased. The *c* lattice parameter shows no overall trend with silicon content, *b* shows a clear trend with silicon content across the range, increasing continuously and appears to be starting to plateau for the higher concentrations. Again there is an overall increase in the unit cell volume with silicon content and an increase in the angle $\beta$, though this change in angle was not reported by the other studies.

Very limited solid state NMR studies on these materials have been reported in the literature. A $^{29}$Si solid state NMR study by Gillespie *et al* [38] of several silicon substituted calcium phosphates using isotropically enriched silica, found evidence for $Q^1$ species in Si-$\alpha$-TCP similar to a rankinite type ($Ca_3Si_2O_7$) formation [108]. While not a phase pure sample, they claim one resonance is attributable to the $\alpha$-TCP structure while the other resonance is assigned to a combination of the TCP structure and the hydroxyapatite phase that is present. However, it should be noted that the signal-to-noise of their result is very poor despite using a sample enriched with $^{29}$Si, this poor signal-to-noise is therefore most probably by the use of inadequate (too short) pulse delays, which makes anything but a generalisation about the results impossible. A similar study done by Gasquères *et al* [36] performed on a bi-phasic hydroxyapatite containing both $\alpha$ and $\beta$-TCP observe several species of silicon and attribute them to $Q^0$ and $Q^2$ moieties. The $Q^0$ species is attributed to the Ha and the TCP phases, while they assign the $Q^2$ resonance to a pseudowollastonite type ($Ca_3Si_3O_9$) structure [109]. However, they were unable to determine if this $Q^2$ resonance was attributable to changes within the structure or existed as a separate phase.

Computational DFT studies by Yin *et al* [30, 87] show good agreement with the

$\alpha$-TCP structure, and go some way to explaining the mechanism of charge balance in substituted TCP, either by $O^{2-}$ vacancy or $Ca^{2+}$ excess. While these studies are purely computational, the overall results are that they show that silicon complexes can be formed in Si-$\alpha$-TCP in the form of $Si_2O_7^{6-}$ to create a charge compensating oxygen vacancy. Though when increased beyond one $Si_2O_7^{6-}$ complex per unit cell, this leads to a significant loss in stability. On the other hand, adding excess calcium for every two $SiO_4^{4-}$ units present is found to generate a more stable structure, and when increased beyond two $SiO_4^{4-}$ tetrahedra per unit cell, the stability is enhanced even further. However, no experimental evidence has been presented as yet for a structure that is charge balanced through a $Ca^{2+}$ excess, likewise apart from one solid state NMR spectrum that claims to support $O^{2-}$ vacancies for charge neutrality, there is nothing conclusive for either mechanism.

More recent studies by Martínez $et$ $al$ [110, 111] show evidence for the inclusion of silicon into the $\alpha$-TCP structure by doping with dicalcium silicate, $Ca_2SiO_4$ ($C_2S$) [112]. Dicalcium silicate is known to exist as a solid solution with TCP [83]. The samples made and characterised by Martínez $et$ $al$ showed that the inclusion of $C_2S$ into TCP had a direct effect on the $\beta$ $\alpha$ transition temperature, just as other methods of silicon substitution. They also point out that at low levels, the $C_2S$ is undetectable with XRD and only a homogeneous phase of $\alpha$-TCP is present, the $C_2S$ only becomes apparent at higher levels of doping, when silicocarnatite ($Ca_5(PO_4)_2$ ($SiO_4$)) [113] starts to form. Their evidence for the formation of a solid solution was generated by scanning electron microscopy-wavelength dispersive spectroscopy(SEM-WDS), where they were able to determine levels of between 1.5 wt % and 3 wt % $C_2S$.

## 5.2  Experimental

### 5.2.1  Sample preparation

The solid-state synthesis of the Si-$\alpha$-TCP (Ca$_3$(PO$_4$)$_{2-x}$(SiO$_4$)$_x$) samples was undertaken by Dr. Jo Duncan from the University of Aberdeen using the same method as that reported in Chapter 4.3.1, however, the following changes were introduced. For silicon-substituted samples Si-TCP (x = 0.10 / Si = 0.91 wt%) isotopically enriched $^{29}$SiO$_2$ (99.33% $^{29}$Si, Cortecnet, France) was used as the source of silicon, and for sample Si-TCP (x = 0.20 / Si = 1.82 wt%) fumed SiO$_2$ (BDH Laboratories, UK) was used as the source of silicon. SiO$_2$ was used in the synthesis at the expense of the phosphorus-containing CaHPO$_4$phase with the reduction in calcium compensated for by the addition of more CaCO$_3$ to maintain the bulk Ca/(P+Si) ratio at 1.5. The overall phase purity was checked using a Bruker D8 Advance diffractometer, against ICDD card No. 09-348.

### 5.2.2  calculations

. The methods involved for the GIPAW DFT calculations preformed by Dr. David Quigley from the University of Warwick, for Si-$\alpha$-TCP are outlined in Chapter 4.3.2.

### 5.2.3  Solid State NMR Experiments

. All $^{31}$P and $^{29}$Si MAS experiments were performed at 11.7 T ($\nu_0$ = 202.4 MHz and 99.34 MHz respectively) on a Bruker Advance III, 500 MHz spectrometer. These $^{31}$P and $^{29}$Si experiments were enabled using a Bruker 4mm HXY probe (shimmed to 2 Hz) and a Doty Scientific 7 mm HX probe (shimmed 8 Hz). Single pulse $^{31}$P data were acquired using a tip angle of $\pi/2 = 4$ $\mu$s, a recycle delay of 480 s (4 acquisitions) spinning at 12 kHz, while single pulse $^{29}$Si data were acquired using both probes calibrated to a $\pi/4 = 3.5$ $\mu$s, and using a recycle delay of 480 s (240 acquisitions) spinning at 6 kHz.

$^{31}$P-$^{31}$P R12$_2^5$ data were undertaken using a Bruker 4 mm HXY probe with $\pi/2 = 7\mu$s. The B$_1$ field was rotor synchronized to three times the MAS frequency of 11900 KHz and using an X nucleus amplifier level of 13.6 db; a recycle delay of 60 seconds, 24

$f_1$ increments and 32 scans per increment were used in conjunction with a re–coupling loop $l_0 = 50$. A preceding saturation comb was also employed using 35 $\pi/2$ pulses and a 50 ms delay between them. Short recycle delays were required to give the optimum signal per unit time and experimental performance.

Additional $^{29}$Si experiments were performed at a lower field of 7.05 T ($\nu_0 = 59.56$ MHz) on a Varian Infinity Plus 300 MHz spectrometer using a Bruker 7 mm HX probe. Single pulse $^{29}$Si data were acquired with a $\pi/4 = 3.5\mu$s, using a recycle delay of 480 s with 128 acquisitions required for sample x = 0.1 and 896 acquisitions for sample x = 0.2. These experiments used an MAS rate of 6 kHz.

$^{31}$P-$^{29}$Si HETCOR data was acquired at 11.7 T on a Bruker Advance III, 500 MHz using a Bruker 4 mm HXY probe which operated with $^{31}$P(X) and $^{29}$Si(Y) channels both calibrated for $\pi/2$ pulse times of 7 $\mu$s to establish a Hartmann-Hahn match condition. The optimal signal-to-noise and overall spectral result acquired within a reasonable time was achieved with 24 F1 increments with 800 scans per slice and was collected using a contact time of 40 $\mu$s as previously reported in [114], and a recycle delay of 30 seconds.

A $^{29}$Si refocused-INADEQUATE was performed on a Bruker Advance III 500 MHz spectrometer using a Doty 7 mm MAS probe, spinning at 6 kHz. The $\pi/4$ pulse was calibrated to 7 $\mu$s, the recycle delay (while heavily saturating the signal) was found to be adequate at 8 s to give the best signal per unit time, the $\tau$ refocus delay was 80 ms and 540000 transients scans were acquired.

All $^{31}$P and $^{29}$Si chemical shifts were calibrated to secondary solid $NH_4H_2PO_4$ and kaolinite reference materials which are measured at 0.9 ppm and -92 ppm, respectively, with respect to the primary IUPAC standards of 85% $H_3PO_4$ ($\delta$ 0 ppm)and TMS($\delta$ 0 ppm). The deconvolution of 1D spectra was performed using the DMFit [98] software and the analysis of all 2D data was undertaken using Bruker Topsin 2.1.

## 5.3    Results and Discussion

### 5.3.1    $^{31}$P MAS NMR Results of Si-$\alpha$-TCP

While the $^{31}$P MAS NMR results for $\alpha$-TCP discussed in Chapter 4.4.1 gave different degrees of resolution depending on level and type of impurities, it was still possible to resolve a significant number of resonances. In contrast, if we observe the effects of Si substitution on the corresponding $^{31}$P MAS NMR spectra for Si-$\alpha$-TCP in Figure 5.1a, a *complete* loss of short range order and associated resolution has been induced by less than 1 wt% of Si substitution; this is similar to the impurity levels discussed above but it presents far greater consequences as far as short range order of the $\alpha$-TCP structure is concerned. In analogous fashion to the pure $\alpha$-TCP case, the observed $^{31}$P chemical shift range indicates that after Si substitution the remaining P speciation is still found to be isolated tetrahedra, and there is no evidence of any condensation of the orthophosphate $PO_4{}^{3-}$ units, to make pyrophosphate $P_2O_7{}^{4-}$, nor is there any evidence of Si-O-P bonding.

From Figure 5.1 very few features are discernible and the spectrum is dominated by two broad resonances, with other shoulders and inflexions also being observable. The $^{31}$P MAS NMR study of various Si-$\alpha$-TCP preparations (not shown) consistently verify that this broadening is purely due to Si incorporation into the structure. This lineshape is a feature of all synthesised samples, whether or not they include additional impurities; even paramagnetic Fe-bearing preparations are characterised by the broadening induced by Si doping. This suggests that when Si is substituted into the $\alpha$-TCP structure, there is considerable disruption to the local shortrange structure, even though there is little apparent change to the unit cell and long range order. Upon direct comparison of the $^{31}$P MAS NMR data obtained from samples of $\alpha$-TCP and Si-$\alpha$-TCP (see Figure 5.1b). It can be observed that the overall envelopes governing both data are quite similar and that the broadened peaks and shoulders of the Si-$\alpha$-TCP correspond with elements of the original $\alpha$-TCP spectrum. The outlying resonance at 4.05 ppm is still clearly visible in the substituted sample as a prominent shoulder, and the intensity and distribution of the broad resonances largely correspond to that of the original sample. There is a noticeable lack of intensity on the highfield side of the
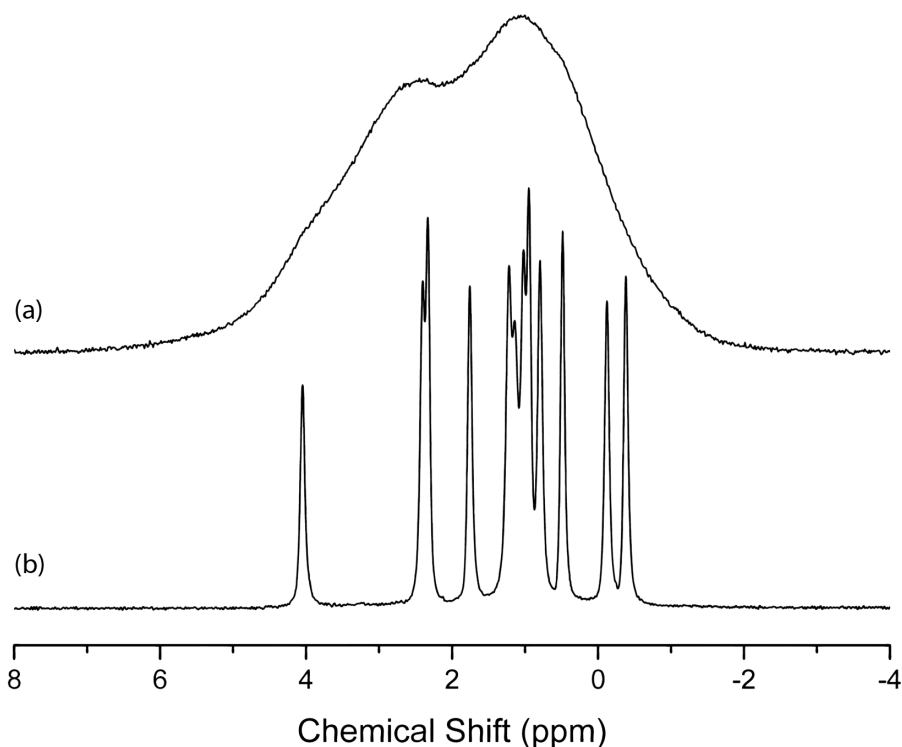
Figure 5.1: $^{31}$P NMR comparison between(a) Si-$\alpha$-TCP x = 0.1 and (b) $\alpha$-TCP, clearly showing the significant amount of disorder introduced to the structure with even low levels of silicon substitution.

spectrum $\sim$ 0 - −1 ppm, indicating the possible occurrence of sites that are involved in the Si substitution process. However, it is also possible that these resonances have been severely broadened due to disorder.

While it has been established that there is little apparent change to the long range order of the $\alpha$-TCP structure with Si incorporation [85, 86, 107], and that spectral features can be observed at the same shift as the original structure, this would suggest that while considerable disorder has been introduced into the lattice at the local level by the substitution of $SiO_4{}^{4-}$ for $PO_4{}^{3-}$, all this evidence indicates that the underlying structure remains similar, and it is not possible to probe these changes using 1D $^{31}$P MAS NMR. Even though there are only approximately 2.5 Si atoms per $\alpha$-TCP cell in these preparations, out of a possible 48 P positions, it is entirely possible that the Si can reside in very different positions in some unit cells. Furthermore the average Si-O bond length (ideally $\sim$ 1.6 Å) is slightly longer than its P-O counterpart (ideally

$\sim 1.5$Å), hence the structure needs to expand and contract locally to accommodate this incorporation. Thus, a large distribution of chemical shifts (in comparison to the original $^{31}$P linewidths from $\alpha$-TCP) results from this phenomenon, as evidenced by the $^{31}$P MAS NMR data of Figure 5.1

## 5.3.2  $^{31}$P DQ NMR Experiments of Si-$\alpha$-TCP

As in Chapter 4.4.2 R12$_2^5$ $^{31}$P–$^{31}$P dipolar re-coupling experiments were also performed on Si-$\alpha$-TCP. In contrast, while the 2D experiment for $\alpha$-TCP exhibits very good resolution like that of the $^{31}$P MAS NMR counterparts in Figure 4.3, it can be seen from Figure 5.2 that the 2D double quantum R12 dipolar re-coupling experiment does not improve the resolution of the 1D $^{31}$P MAS NMR data (Figure 5.1a) from the Si-$\alpha$-TCP system. The disorder that has been introduced into the $\alpha$-TCP structure by the Si substitution is also translated directly into the 2D spectrum, and unfortunately it is impossible to improve the resolution. This demonstrates the limitations of looking directly at the $^{31}$P nucleus in order to gain structural information for substituted $\alpha$-TCP samples, as little information is forthcoming apart from the observed disorder is which is very apparent.
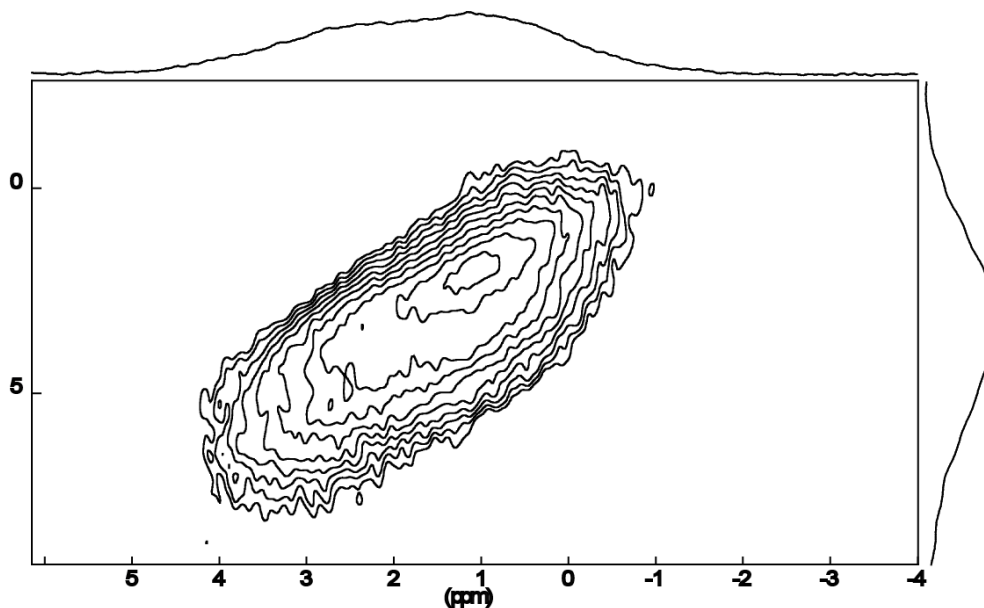


Figure 5.2: $^{31}$P–$^{31}$P R12 DQ spectrum for Si-$\alpha$-TCP x = 0.1, the disorder that was observed in the $^3$1P MAS NMR spectrum (Figure 5.1a) is also very apparent in the 2D spectrum

### 5.3.3 $^{29}$Si MAS NMR Results of Si-$\alpha$-TCP

The $^{29}$Si MAS NMR spectrum for Si-$\alpha$-TCP (x = 0.1) is shown in Figure 5.3. The resolution is very good, considering the disorder effects that were observed for the corresponding $^{31}$P data. It is apparent from initial observations that there are multiple resonances present. The resonance at -62.5 ppm can be disregarded, as it is a background signal from the Doty Scientific probe which has a stator block and rotor made from silicon nitride ($Si_3N_4$) and this resonance corresponds to $SiN_3O$ [115]. Further evidence for this assignment is provided when the same data is acquired using a Bruker probe (not shown) which has a Boron nitride stator block and zirconium rotors, and this resonance is subsequently no longer present in the data.
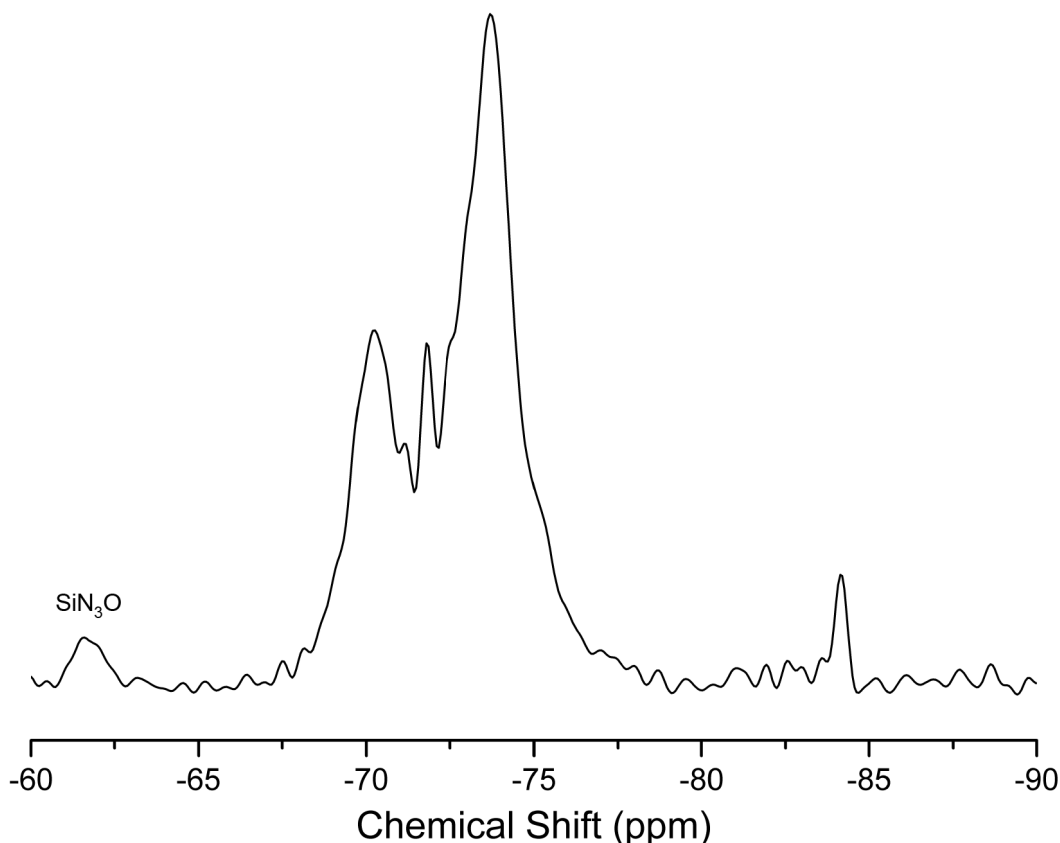


Figure 5.3: $^{29}$Si MAS NMR spectrum of Si-$\alpha$-TCP x = 0.1, showing multiple resonances corresponding to multiple silicon species, - 68 to -74 ppm ($Q^0$) units -74 to -76 ppm ($Q^1$) and -84 ppm ($Q^2$). The resonance at -62.5 ppm is a background signal from the probe.

Silicon is a widely studied nucleus and is reasonably well understood in terms of structure and chemical shift, and it exhibits a well defined chemical shift range for four coordinated silicon ($\sim$ –60 - $\sim$ –120 ppm) and six coordinated ($\sim$ –180 - $\sim$ –200 ppm ) [51] The four coordinate Si range starts at –60 ppm for Si with no bridging oxygens, and progresses upfield (i.e. more negative chemical shifts) when the number of bridging oxygens are increased [116]. These Si species with variable numbers of bridging oxygens are usually denoted as $Q^n$ species where n = 1–4. Complications can arise when assigning $^{29}$Si data, as various $Q^n$ chemical shift ranges often overlap as it is important to take into account next nearest atomic neighbours which will also influence the $^{29}$Si shifts. Calcium silicates start at $\sim$ –70 ppm and go more negative as the number of bridging oxygens increase, compared to lithium silicates which start around $\sim$ –60 ppm and again move upfield as the number of bridging oxygens increases [51]; the shift is usually of the order of a 10 ppm shift in the negative direction for every extra bridging oxygen [116] Furthermore, not only is the overall shift range sensitive to the next nearest neighbour element it will also be influenced by the number of next nearest neighbours [117].

As can be seen in the spectrum for Si-$\alpha$-TCP Figure (5.3), the bulk of the $^{29}$Si resonances are in the region -68 ppm to -76 ppm, most can thus be assigned as isolated $Q^0$ tetrahedra. This is in complete agreement with studies of calcium silicates in the literature [118]. The only chemical shift region that poses any ambiguity is the region around -75 ppm, as this is now in an overlap region between $Q^0$ and $Q^1$. $Q^1$ calcium silicate resonances in this region, can be associated with the mineral rankinite ($Ca_3Si_2O_7$) [108] [118] which exhibits shifts of -74 ppm and -75 ppm. This peak does agree somewhat with the study by Gillespie *et al* [38] who reported resonances at –75 and –78 ppm, and they attribute both of these to $Q^1$ species in the $\alpha$-TCP structure, though it should be noted that their data is very poor considering they are studying a $^{29}$Si enriched sample. Gasquères *et al* [36] attribute a resonance observed at -76 ppm as a $^{29}$Si resonance associated with TCP but give no information for which phase, and they report this as a $Q^0$ species.

The small resonance at -84 ppm observed in Figure 5.3 can be readily assigned to a $Q^2$ species and is in a similar position to that of pseudowollastonite ($Ca_3Si_3O_9$) [109],

which has been previously reported at a shift of –83.5 ppm [118]. Pseudowollastonite is also a high temperature phase, and this assignment is tentatively supported by a phase characterisation using XRD (not shown), while the phase characterisation of the overall structure was in agreement with that already published for Si-$\alpha$-TCP [86], a detailed search found that there were some low intensity reflections in the diffraction pattern that were unassigned. The best match for these unassigned peaks was $CaSiO_3$ or $SiO_2$. However, as there is no evidence from the $^{29}Si$ MAS NMR supporting the assignment of $SiO_2$, it is more likely to be $CaSiO_3$ which is supported by the NMR data. Unfortunately, there is no indication whether this is a separate phase, or makes up part of the structure. Furthermore this resonance at –84 ppm is by no means unique to this sample. A comparison the $^{29}Si$ data from the enriched sample shown in Figure 5.3 with a non-enriched preparation is shown in Figure 5.4(x = 0.1 and 0.2) The overall shape and distribution of these spectra are quite similar. The resolution of the x = 0.2 sample has been reduced, and this is most likely due to the increased level of silicon (i.e. increased disorder) and a worse S/N level due to the sample being natural abundance. Interestingly, Gasquères *et al* [36] studying a biphasic sample of hydroxyapatite containing both $\alpha$ and $\beta$-TCP report a similar resonance at –84 ppm and attribute it also to a pseudowollastonite-type structure, but were unable to determine its relationship to the structure.

In order to ascertain how much of the sample was $Q^2$ in each case, both spectra in Figure 5.4 were simulated with the minimum number of resonances; for the main manifold of resonance, three resonances were required to describe the labelled and non labelled samples and a single fitted resonance was needed for the signal at –84 ppm. This analysis demonstrates that the amount of the structural moiety represented by the $Q^2$ resonance in the x = 0.2 sample constitutes about 5-6 % of the overall total, whereas in the x = 0.1 sample it constitutes less than 3 %. This would imply that the presence of the $Q^2$ species is not a random occurrence related to the formation of impurities, but is a necessary result directly related to the final structure. However, at this stage there is no way of defining if this structural moiety is actually part of the overall Si-$\alpha$-TCP structure. This formation of $Q^2$ species could be related to limitations in the structure, as it has been noted by Reid *et al* [85] that above 1.14 wt% they observed
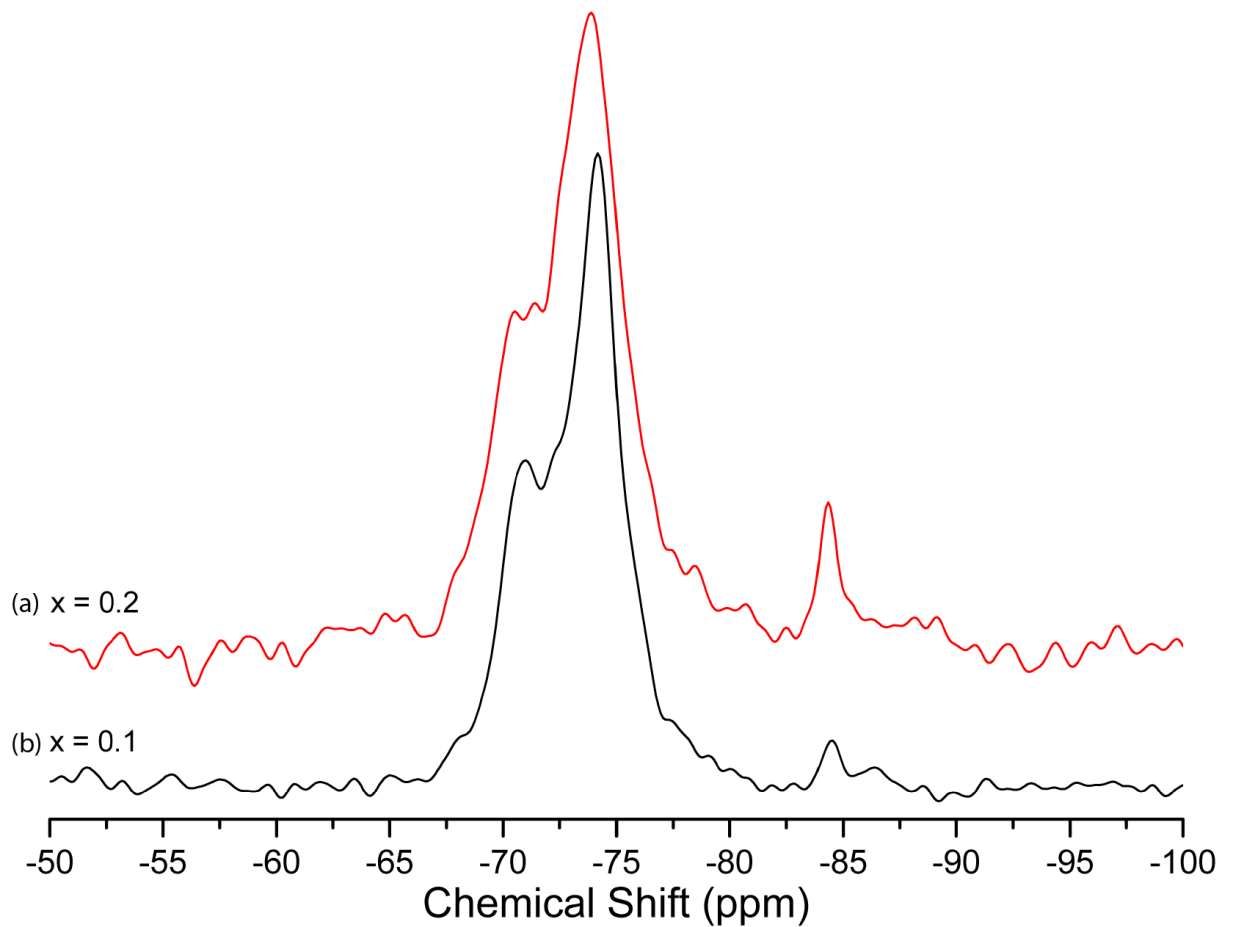
Figure 5.4: Comparison of $^{29}$Si MAS NMR for samples of (a) Si-$\alpha$-TCP with x = 0.2 (b) and x = 0.1. While the overall shape is similar, a degradation in the resolution is observed at the higher level of silicon content. However, there is a clear difference in the intensity of the $Q^2$ peak at -84 ppm showing its apparent dependence on silicon levels.

the formation of separate phases, and there does appear to be an upper limit on the amount of the Si that can be taken up by the structure. The new results reported above show no evidence of different calcium phosphate phases with higher levels of silicon content, though this could be down to differences in sample preparation, Reid *et al* use a precipitate method [85], whereas the samples in this study are made by a solid state synthesis route; this intrinsic difference could present the opportunity for different mechanisms of charge balance and the formation of different phases. Nevertheless, it has been observed that pseudowollastonite can exist as a solid solution with $\alpha$-TCP (and vice-versa) [119], hence there is compelling evidence that suggests the $Q^2$ species could be within the main $\alpha$-TCP structure.

Beyond establishing the approximate amount of $Q^2$ species present, a detailed deconvolution of any of the $^{29}$Si MAS NMR spectra is not possible. As is evident in Figure 5.3 the main resonance between $-68$ - $-76$ ppm is built up of many overlapping peaks, thus any attempt at modelling such a spectrum would involve a significant amount of assumption, allowing for a lot of misinterpretation. Therefore to avoid any ambiguity a detailed deconvolution has been omitted, and a different approach was taken to try and resolve this issue (see Section 5.3.6 below).

### 5.3.4   DFT Calculations on Si-$\alpha$-TCP

DFT calculations were performed on a Si substituted unit cell of $\alpha$-TCP. A series of calculations were performed for each different charge balance mechanism that involved $Ca^{2+}$ excess and $O^{2-}$ vacancies. In the case of the $Ca^{2+}$ excess, if charge neutrality is to be maintained then an extra $Ca^{2+}$ would have to be included for every two $SiO_4^{4-}$ units, and this will have to be located near the $SiO_4^{4-}$ position. Indeed, the structure has plenty excess space to accommodate this, as there are cation vacancies in the cation-anion columns (see Figure 5.5c). By substituting the two $PO_4^{3-}$ units either side of the vacancy for $SiO_4^{4-}$ and filling the vacancy with a $Ca^{2+}$, charge neutrality is maintained. This was attempted for two different locations in the unit cell and the resultant structure in each case was stable and exhibited similar increases to the unit cell (b, $\beta$, overall volume) as did the crystal structure refinements. The second method prescribed the inclusion of oxygen vacancies in the structure where two adjacent $PO_4^{3-}$ units substitute for two $SiO_4^{4-}$ ions, and these two $SiO_4^{4-}$ ions condense to form a $Si_2O_7^{6-}$ moiety by losing an oxygen to retain charge neutrality (Figure 5.5b). These calculations are much less energetically favourable in comparison as the resultant structure was very unstable and would never promote the formation of $Si_2O_7^{6-}$ unless forced. Furthermore, the lattice parameters were observed to decrease, thus contradicting the observations from the XRD analysis. Based on these results alone it appears that the preferred method of charge balancing the Si incorporation into the $\alpha$-TCP structure is via additional $Ca^{2+}$ excess.

This agrees somewhat with the study by Yin *et al* [30], who did a very extensive

theoretical study of silicon substitution into $\alpha$-TCP looking at both charge balance mechanisms. They also found that the $Ca^{2+}$ excess was energetically more favourable than $O^{2-}$ vacancies, though unlike this study they do not report any difficulties with the structure being unstable and they postulated several different possibilities in the unit cell where $O^{2-}$ vacancies can form. However, they do report that the structure becomes less stable if more than one $Si_2O_7{}^{6-}$ unit is present within the unit cell. Conversely when $Ca^{2+}$ was calculated as the charge balance mechanism, increasing the amount $Ca^{2+}$ was found to further stabilise the structure. The unit cell predictions by their calculations are again in agreement with the study done here, they show a shrinking unit cell for the $O^{2-}$ vacancy incorporation and an increase in the unit cell for a charge balance mechanism involving $Ca^{2+}$, which is in agreement with crystal lattice refinement data [85, 86, 107].

However there are several problems with the computational results, while the study by Yin *et al* was purely theoretical it was not correlated with any form of synthesis. In the study performed in this work a $Ca^{2+}$ charge mechanism is contradicted by two things. Firstly the sample was made with no calcium excess; $\alpha$-TCP has a Ca/P ratio of 1.5 and the synthesis involving Si substitution took this into account so that the Si-$\alpha$-TCP has a ratio of Ca/P+Si of 1.5. This is confirmed by X-ray fluorescence [107], where the Ca/P+Si ratio was found to be less than 1.51, whereas for a $Ca^{2+}$ excess the required ratio would need to be closer to 1.55. Secondly, it is impossible to interpret the data below (See Section 5.3.6) in terms of a $Ca^{2+}$ excess, and as can be seen from the experiments in the next Section 5.3.5, the data is more readily interpreted in terms of $O^{2-}$ vacancies.
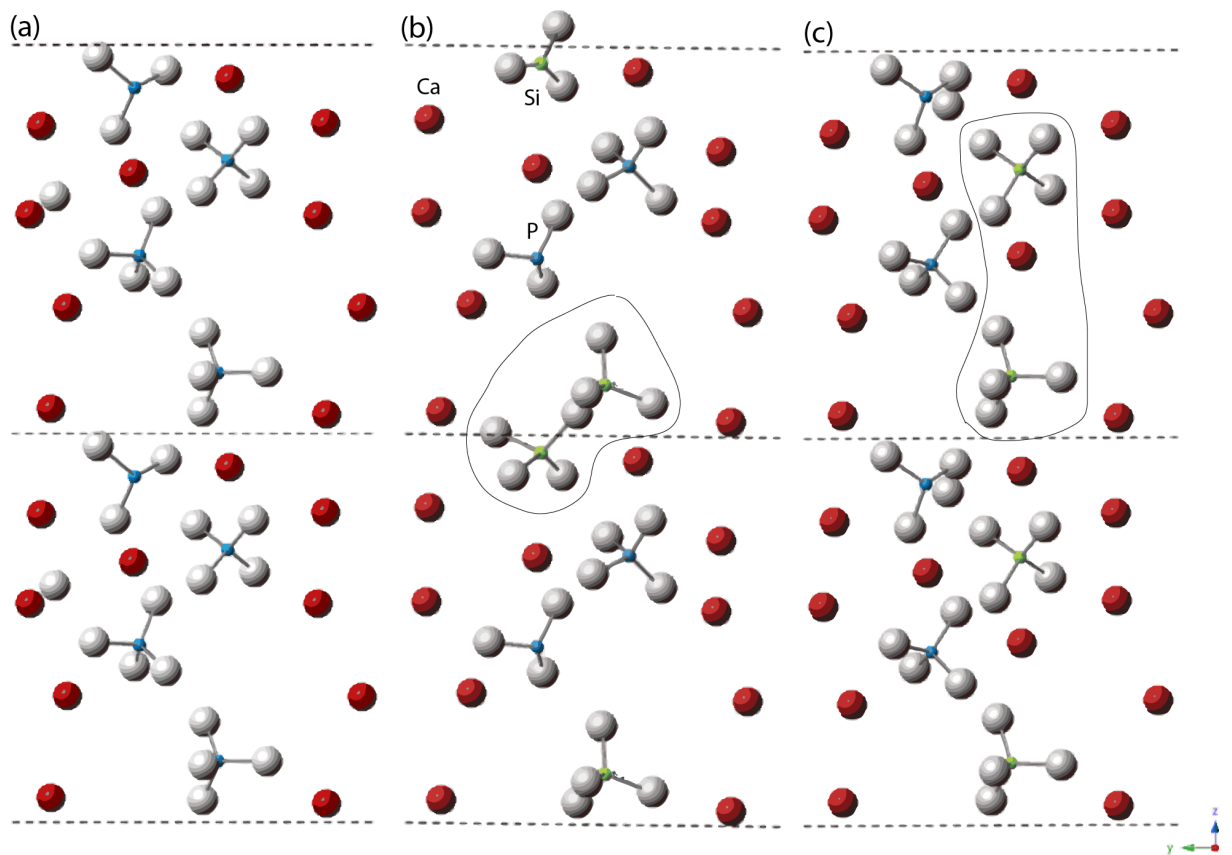
Figure 5.5: A pictorial representation of the different charge balance mechanisms and locations of Si in the $\alpha$-TCP lattice as predicted by the DFT calculations (a) the $\alpha$-TCP structure for comparison (b) the $O^{2-}$ vacancy mechanism, a bridge is made between two adjacent cation-anion columns by the formation of $Si_2O_7^{6-}$ when replacing two $PO_4^{3-}$ units (c) involving $Ca^{2+}$ excess, the $Ca^{2+}$ goes into an existing vacancy in the cation-anion column and the two adjoining $PO_4^{3-}$ are replaced by $SiO_4^{4-}$.

### 5.3.5 $^{29}$Si Refocused-Inadequate

Due to anomalies with the predictions of the calculations and the inability to interpret the results in section 5.3.6 below in terms of outcomes favouring $Ca^{2+}$ excess , an experiment was undertaken to determine the true nature of the species that appear in the $^{29}$Si MAS silicon spectrum 5.3.3. This data does present some ambiguity as the –74 ppm to –76 ppm region has been established where $Q^1$ species can appear [118], and furthermore the isolated $Q^0$ species associated with calcium silicates have been reported in the –68 ppm to –75 ppm [118]. There is very limited literature for $^{29}$Si NMR of silicon substituted calcium phosphates, though this is not surprising due to the low natural abundance of $^{29}$Si and low levels of substitution. As discussed earlier the only previous $^{29}$Si MAS NMR study of Si-$\alpha$-TCP exhibits only marginal disagreement with this work, where their resonances are reported at –75 and –78 ppm [38]. There are two further studies of bi-phasic materials, one containing a mixture of hydroxyapatite and $\beta$-TCP [120] reporting resonances at -69, -73 and -78 ppm, and the other containing hydroxyapatite, $\alpha$ and $\beta$-TCP [36] with resonances at -72 and -76 ppm, however they attribute all of them to $Q^0$ species. In the study by Gillespie *et al* (using the method by Sherriff *et al* [121], that relates structure to $^{29}$Si chemical shift), they give some predicted $^{29}$Si chemical shifts based on the work of Yin *et al* [30] and Astala *et al* [122]. These predictions show that in Si substituted hydroxyapatite and $\alpha$-TCP both charge balance mechanisms are supported and that resonances from $Q^0$ and $Q^1$ species will appear in the region –69 ppm to –81 ppm. However, what it does demonstrate, is that the calculations indicate that the $Q^1$ shift region starts at around –70 ppm. It is known that $^{29}$Si calculations differ by a few ppm in most cases, from experimental results [123], but overall good agreement has been demonstrated. However, the only way to be able to effectively distinguish between $Q^0$ and $Q^1$ species in this region is through experiment.

In order to clarify if $Q^1$ species are present along side $Q^0$ species, a $^{29}$Si refocused-INADEQUATE (see Section 3.5.3) experiment was performed on Si-$\alpha$-TCP. In the refocused-INADEQUATE experiment, the only $^{29}$Si signal that should appear would emanate from Si positions that are scalar or (J-coupled) together; i.e. only those

Si species that share a common bond to a next nearest Si neighbour will survive the double quantum selection process, and isolated Si tetrahedra $Q^0$ species will be eliminated. Any signal that is left will correspond to a bridged Si-O-Si unit only, as longer range connectivity is not probable and the experiment is not configured to detect it. This kind of experiment would not normally be performed on $^{29}$Si due to the low natural abundance ($\sim$ 5 %), as statistically there is not enough $^{29}$Si to comprise sufficient numbers of $^{29}$Si-O-$^{29}$Si units, however, it has been shown to work on enriched systems [124] where high levels of enrichment facilitate sufficient quantities of $^{29}$Si-O-$^{29}$Si formation.
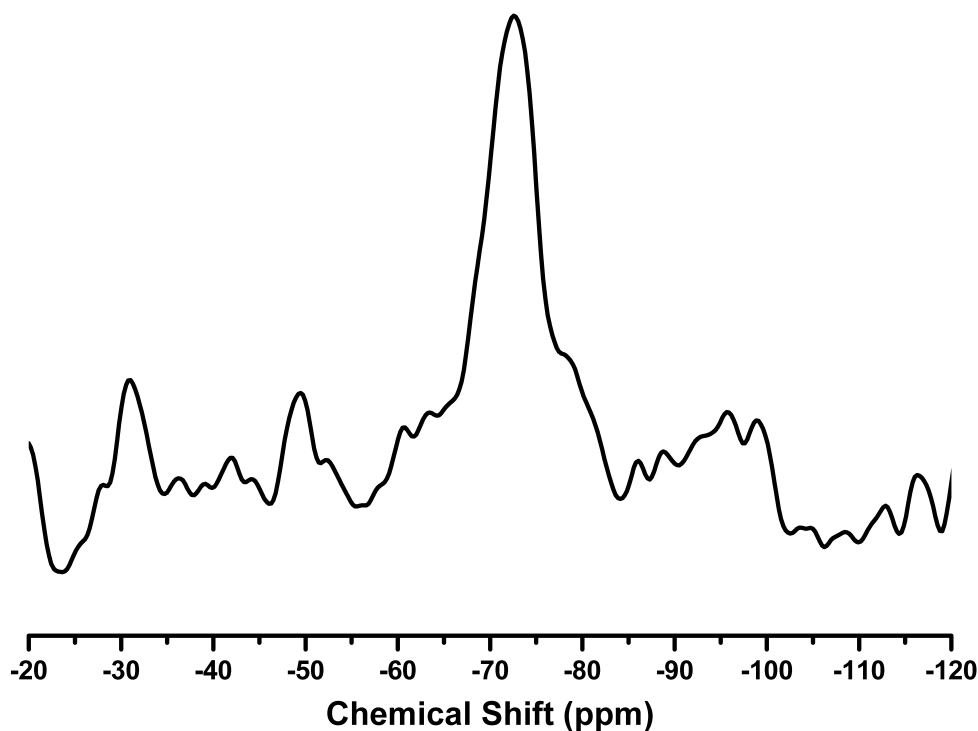


Figure 5.6: $^{29}$Si refocused-INADEQUATE experiment for Si-$\alpha$-TCP x = 0.1, showing a peak centred at -73 ppm, indicating that a significant part, if not all, of the sample between –69 - –76 ppm is $Q^1$ silicon species

The results of the $^{29}$Si refocused-INADEQUATE are shown in Figure 5.6. While high levels of $^{29}$Si enrichment do exist in this sample, concomitant low levels of Si incorporation exist in the Si-$\alpha$-TCP hence the very poor signal-to-noise obtained. The signal-to-noise level is further disadvantaged by the double quantum nature of the experiment. Furthermore, it was not possible to optimize the experiment in terms of the

evolution time; a short time of 20 ms was attempted first, but without success. Looking at some literature for this type of experiment in calcium silicates, it was found that the J-couplings range between 3.3 to 15 Hz having been reported, thus giving an evolution time in the range of 20 to 160 ms [125]. Therefore a mid point of 80 ms was chosen, and this produced the $^{29}$Si signal observed in Figure 5.6. The low signal-to-noise was further hampered by the long $^{29}$Si $T_1$ which is in excess of 10 minutes. What Figure 5.6 clearly shows is a resonance centred at –73 ppm unambiguously confirming the presence of $Q^1$ species. However, the resonance covers the entire of range –69 to –76 ppm, but due to the low signal to noise and poor resolution it is not possible to say that all of the silicon depicted in Figures 5.3 and 5.4 is $Q^1$. It is entirely possible that some of the species that we observe in the 1D data of Figures 5.3 and 5.4 is $Q^0$, however, these results do agree with the predictions of the $Q^1$ chemical shifts by Gillespie *et al* [38] with an estimated $^{29}$Si shift range of –70.4ppm to –81.1 ppm.

## 5.3.6   $^{31}$P-$^{29}$Si CP HETCOR of Si-$\alpha$-TCP x = 0.1

In similar fashion to the $^{31}$P-$^{31}$P correlation, a $^{31}$P-$^{29}$Si CP HETCOR experiment (see Section 3.5.4) can show the connectivity between different sites, although this experiment now probes heteronuclear couplings between $^{31}$P and $^{29}$Si that can be observed by transferring magnetisation from a higher $\gamma$ ($^{31}$P) nucleus to a lower $\gamma$ ($^{29}Si$) nucleus. The dipolar coupling between P and Si is small, even at short distances. The shortest P-P distance in this compound is 4.118 Å and if it is assumed to be the same for a P-Si distance, this gives a dipolar coupling of $\sim$ 155 Hz [126] and this reduces markedly with longer distances as a $1/r_{xy}^3$ dependence exists. Therefore, long contact times (on the order of tens of milliseconds) are required to transfer this magnetisation [114]. Very few $^{31}$P-$^{29}$Si cross polarisation experiments have been reported, successful studies focussed on systems with either direct P-Si bonds [127] or P-O-Si bonds [128] representing distances of around 2.2 and 3 Å, respectively. While these experiments are not trivial the small dipolar couplings are significantly larger at these shorter distances and efficient CP transfer will be selective for shorter range interactions only.

It is not possible to get a quantitative result from this type of experiment, as the intensity of each resonance is dependant on unique build-up characteristics governed by the distance and the number of different sites involved in the cross-polarisation. Nevertheless, it is possible to gain reliable qualitative information as to which Si sites are in close proximity to specific P positions. Due to the weak P-Si dipolar coupling, realistically only those sites that are spatially proximate will participate in this process. Sites distributed over 5 Å or more will have a dipolar coupling of $\leq$ 80 Hz, therefore requiring extremely long and prohibitive cross polarisation times.

The $^{31}$P-$^{29}$Si HETCOR for Si-$\alpha$-TCP is shown in Figure 5.7(top) along with a 1D $^{29}$Si MAS spectrum representing the $f_2$ projection. As observed from this data, there are multiple Si sites in close proximity to multiple P sites, proving beyond doubt that the Si substitutes directly into the structure. It is clear that the resonance centred at about -73 ppm in the 1D $^{29}$Si MAS spectrum on the $f_2$ projection, comprises the dominant interactions between the P and Si speciation. There are multiple $^{29}$Si chemical shifts interacting with only a small number of the $^{31}$P chemical shifts, indicating that there is some preference in the location of Si in the structure. This region around -73 ppm consists of >10 individual resonances. Looking at the other regions of the spectrum at this level, there are another eight resonances making a total of eighteen non-equivalent definite Si locations. The sharp feature at -71.9 ppm in the 1D $^{29}$Si MAS NMR spectrum, is also present in the corresponding 2D data, however the resonances at -71 and -72.5 ppm do not correspond to the other prominent features in this spectrum. In contrast they probably correspond to species that are not visible in the 1D data, while the two further protruding peaks in the 1D spectrum are of much weaker intensity in the 2D data and can be observed in Figure 5.7(bottom) close to the floor limit. The three resonances at approx -70 to -70.5 ppm correspond to the smaller of the features in the 1D spectrum. All the major correlations along with some of the tentative ones, are summarised in table 5.1.

If weaker resonances are to be considered by moving the plot closer to the floor (see Figure 5.7(bottom)), then there are thirty or more correlations in total. Problems are now being experienced as it is difficult to assign most of these with any certainty and differentiate them from spectral noise. With this in mind the main focus for this
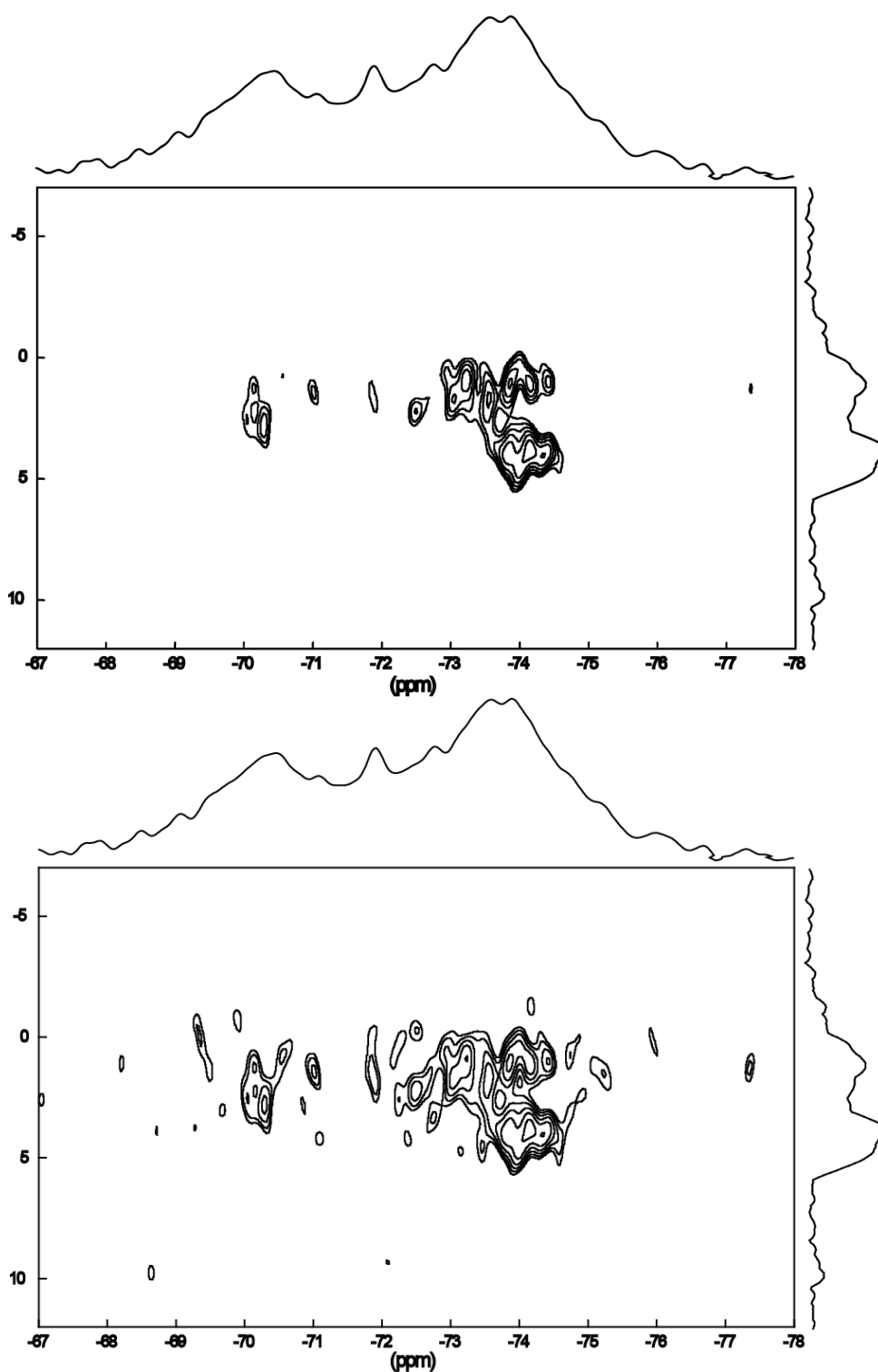
Figure 5.7: Shows the result of the $^{31}$P-$^{29}$Si HETCOR experiment for Si-$\alpha$-TCP x = 0.1, the f$_2$ projection is a 1D $^{29}$Si MAS spectrum taken with the same probe for illustrative purposes. (top) The spectrum clearly shows eighteen non-equivalent silicon sites corresponding to different $^{31}$P chemical shifts, where most of these $^{31}$P shifts agree with the original $\alpha$-TCP structure. (bottom) The same spectrum but shifted closer to the baseline, it is possible that there are upwards of thirty resonances, however it is difficult to be certain as there is now noise in the spectrum.

data is to treat the eighteen definite resonances to avoid any ambiguity, though where advantageous, some of the more tentative resonances will be included.

There was no evidence for any interaction between the $Q^2$ peak at -84 ppm and any of the P sites. This does not rule out that it lies within the bulk structure, as it is entirely possible that it is quite far from any P sites, or the signal-to-noise was too poor due to its low intensity. The vast majority of the correlations are to $^{31}$P chemical shifts that can be attributed to the chemical shifts for the original structure. This suggests that the bulk structure remains largely complete, but is only detectable indirectly. While some movement is to be expected to accommodate the slightly longer bonds of the Si-O unit, in most cases, the $^{31}$P resonances are within 0.05 - 0.1 ppm of their original position. Despite most $^{31}$P resonances being very close to the original $\alpha$-TCP chemical shifts, there are some $^{29}$Si resonances that correlate with $^{31}$P resonances which are shifted 0.3 - 0.5 ppm from any of the original positions, these appear in the region between 2.8 - 4 ppm, these are some of the most intense correlations in the structure. There is little to no interaction evident for sites P6 and P11, either these sites have been completely replaced by Si, hence no correlation is possible or there is no Si nearby these sites. A closer observation of site P6 shows that there are no other P sites closer than 4.5 Å, at this distance the P-Si dipolar coupling is very weak, so there would not necessarily be an observable correlation even if Si is nearby. P11 on the other hand, is reasonably close to P1 at 4.26 Å so if there is Si on either site some interaction is to be expected, as a correlation for P11 is not present, it can only be assumed that there is no Si nearby, however this does not rule out that there is Si on the P11 site itself.

On the other hand, some of the correlations that have the same $^{31}$P shift as the original structure, show a large association with the Si, suggesting that nearby P sites have been replaced. This is especially true for the case of $^{31}$P shifts around 1 and 4 ppm where it appears that the majority of the silicon is correlating, although it is difficult to say with certainty which P resonance is playing a part around the 1 ppm region as there are 3-4 $^{31}$P resonances all within 0.2 ppm of each other. There are also several $^{31}$P chemical shifts that have moved substantially from their original positions, this shift movement is typically 0.3-0.5 ppm and suggests that there have been significant

changes to some local environments, these are predominantly associated with the $^{31}$P chemical shifts around 3.8 and 4.3 ppm.

As mentioned in section 5.3.4 the more favourable method of charge balance was through a $Ca^{2+}$ excess, where this excess Ca occupies an existing vacancy in a cation-anion column and the two adjacent P (either side) are replaced. The calculations by Yin *et al* [30] give details for all six of these possible positions in the unit cell with corresponding energies, while the calculations in this study give the results for two locations. Hence, there are well defined positions for each substituted $SiO_4^{4-}$ unit. It was also mentioned in Section 5.3.4 that it was not possible to interpret the $^{31}$P-$^{29}$Si HETCOR with regards to this charge balance mechanism. The reason for this is all the $^{29}$Si chemical shifts only correspond to one $^{31}$P chemical shift, it is possible that some go to two $^{31}$P chemical shifts, but these are few in number and it is not certain that they are real as they exist where the noise is starting to appear. If the charge balance mechanism was through $Ca^{2+}$, then no matter which one of the six locations were involved in the substitution, at least one of the silicon pairs should have two Phosphorous sites that are less than 4.5 Å and in most case two within 4.3 or 4.4 Å, therefore plenty of $^{29}$Si chemical shifts should be observed that correlate to two or more $^{31}$P chemical shifts. However, this is not the case as the strongest eighteen correlations observed exhibit only a one-to-one correspondence between a $^{29}$Si and $^{31}$P chemical shift. This is especially highlighted by the silicon resonances that correspond to those phosphorous at chemical shift 4 ppm, as these correspond to site P8. P8 has two close neighbours P5 at 4.11 Å and P4 at 4.42 Å, P5 is in turn very close to P3 at 4.29 Å and P4 is very close to P1 at 4.185Å. Therefore, if either P4 or P5 had been replaced then either P3 or P1 should also correspond to the same $^{29}$Si chemical shift and they do not. As this can also be confirmed for other positions, it has to be concluded that there is little evidence to suggest that $Ca^{2+}$ excess is the charge balance mechanism.

The fact that there is only one $^{29}$Si shift in general corresponding to one P shift makes interpretation of the data in Figure 5.7 at first glance troublesome. For it looks like the contact time should have been substantially longer, as the sites that are picked out are the ones that are very close. The reasoning for this is that the peaks that correlate to the $^{31}$P shift at 4 ppm are associated with crystal site number P8, which

Table 5.1: Table of correlating $^{31}$P and $^{29}$Si chemical shifts in Si-$\alpha$-TCP and how they relate to the P sites in the original structure, along with corresponding locations in unit cell for the Si-O-Si units.

| $^{31}$P $\delta_{iso}$ | P site in $\alpha$-TCP | $^{29}$Si $\delta_{iso}$ | Si located at P site | Si-O-Si located at Px-O-Py |
|---|---|---|---|---|
| 3.78 | P8* | -74.15 | P5 | P5-O-P3 |
| 3.98 | P8 | -74.36 | P5 | P5-O-P3 |
| 4.22 | P8* | -74.07 | P5 | P5-O-P3 |
| 3.93 | P8 | -73.85 | P5 | P5-O-P3 |
| 1.06 | P9 | -73.87 | P7 or P12 | P12-O-P12 or P10-O-P7 |
| 0.88 | P3 | -73.24 | P5 | P8-O-P5 |
| 1.11 | P9 | -74.17 | P7 or P12 | P12-O-P12 or P10-O-P7 |
| 1.73 | P12 | -73.56 | P12 or P9 | P12-O-P9 or P9-O-P7 |
| 0.41 | P7 | -73.98 | P9 | P9-O-P12 |
| 1.68 | P12 | -73.07 | P12 or P9 | P12-O-P9 or P9-O-P7 |
| 2.81 | * | -70.3 | | |
| 1.01 | P1 | -74.43 | P4 | P8-O-P4 |
| 0.74 | P3 | -73 | P5 | |
| 2.22 | P4 or P10 | -72.51 | P8 or P10 | |
| 1.79 | P12 | -71.89 | P12 or P9 | P12-O-P9 or P9-O-P7 |
| 1.44 | P5* | -71.04 | P8 | P8-O-P4 |
| 1.21 | P5 | -70.21 | P8 | P8-O-P4 |
| 2.61 | * | -70.11 | | |
| 0.74 | P3# | -70.56 | P5 | P8-O-P5 |
| 3.28 | #* | -72.76 | | |
| 2.54 | #* | -72.25 | | |
| -0.27 | P11 or P6# | -72.54 | P1 or P2 | ** |
| 0.74 | P3# | -74.76 | P5 | |
| 1.63 | P12# | -75.27 | P12 or P9 | P12-O-P9 or P9-O-P7 |
| 1.21 | P5# | -75.16 | P8 | P8-O-P4 |
| 4.43 | #* | -73.47 | | |
| 4.17 | #* | -71.11 | | |
| 0.23 | P7# | -72.26 | P9 | P9-O-P12 |

* No corresponding shift in $\alpha$-TCP.
# Tentative assignment
** No corresponding Si-O-Si unit

lies 4.11 Å from its nearest neighbour in the original structure. In contrast, the sites corresponding to the $^{31}$P shifts at approximately 1.06 ppm can be loosely assigned to either site P1 or P9. P1's closest neighbour is 4.18Å and P9's is 4.24Å, as the CP intensity is partly a function of distance (though also depends on the number of spins in close proximity ). The large drop off in intensity even for sites that are only another 0.07 or 0.19 Å further away, suggests that the polarisation transfer is very inefficient.

If this indeed the case then it is unlikely that any polarisation transfer is observed for sites that are much greater than 4.5 Å and certainly not for sites that are greater than 5 Å. However by only correlating to a single P site, readily favours the interpretation of these results for the $O^{2-}$ vacancy mechanism, It shall be established that each P position should only have one very close neighbour or none at all.

According to the study performed by Yin $et$ $al$ [30], $Q^1$ silicon units only form when the substituted $PO_4$ groups were less than 4.769 Å apart. There are twenty four locations in the unit cell where this is the case. When symmetry is taken into account, then this is reduced to seven possible sites; these are P1-P4, P3-P5, P5-P8, P7-P10, P7-P9, P6-P3 and P9-P12. Yin $et$ $al$. found in their calculations that all sites condensed to $Si_2O_7^{6-}$ except P7-P10. Therefore if $Q^1$ units exist in the structure, then these positions in the unit cell are good candidates for having been replaced and the $^{29}Si$ chemical shift should correspond to the chemical shift for the $^{31}P$ next nearest neighbour for these sites.

A detailed survey of the various correlations can start to create a picture of what is emerging structurally, and a summary of the resonances involved and the potential sites are given in Table 5.1 and are marked on Figure 5.8. The most common association is with what was P12 in the original $\alpha$-TCP structure with a $^{31}P$ shift of 1.74 ppm. This correlates to three different Si sites represented by $^{29}Si$ shifts at -71.98, -73.06 and -73.58 ppm, these Si sites are those that have most probably replaced site P9 and/or P12 and they represent a P-Si distances of 4.3 Å and 4.418 Å, respectively. There is nothing else closer than 4.7 Å to P12 and therefore it is unlikely that another correlation would be observed in this experiment. The next region of interest possesses the most dominant correlation (in terms of absolute intensity) which is associated with P8 at 4 ppm. Depending on how this is interpreted there are two to four correlations present; as there are $^{31}P$ chemical shifts slightly shifted at 3.8 ppm and 4.3 ppm, it is possible that these are site P8 that has shifted slightly. For simplicity it is assumed for now that they represent site P8 which has two closest neighbours P5 at 4.118 Å and P4 at 4.42 Å. Hence nothing else is closer than 4.8 Å so Si substitution could target either site(or both), but considering the very strong intensity of this correlation it is likely to be the former.
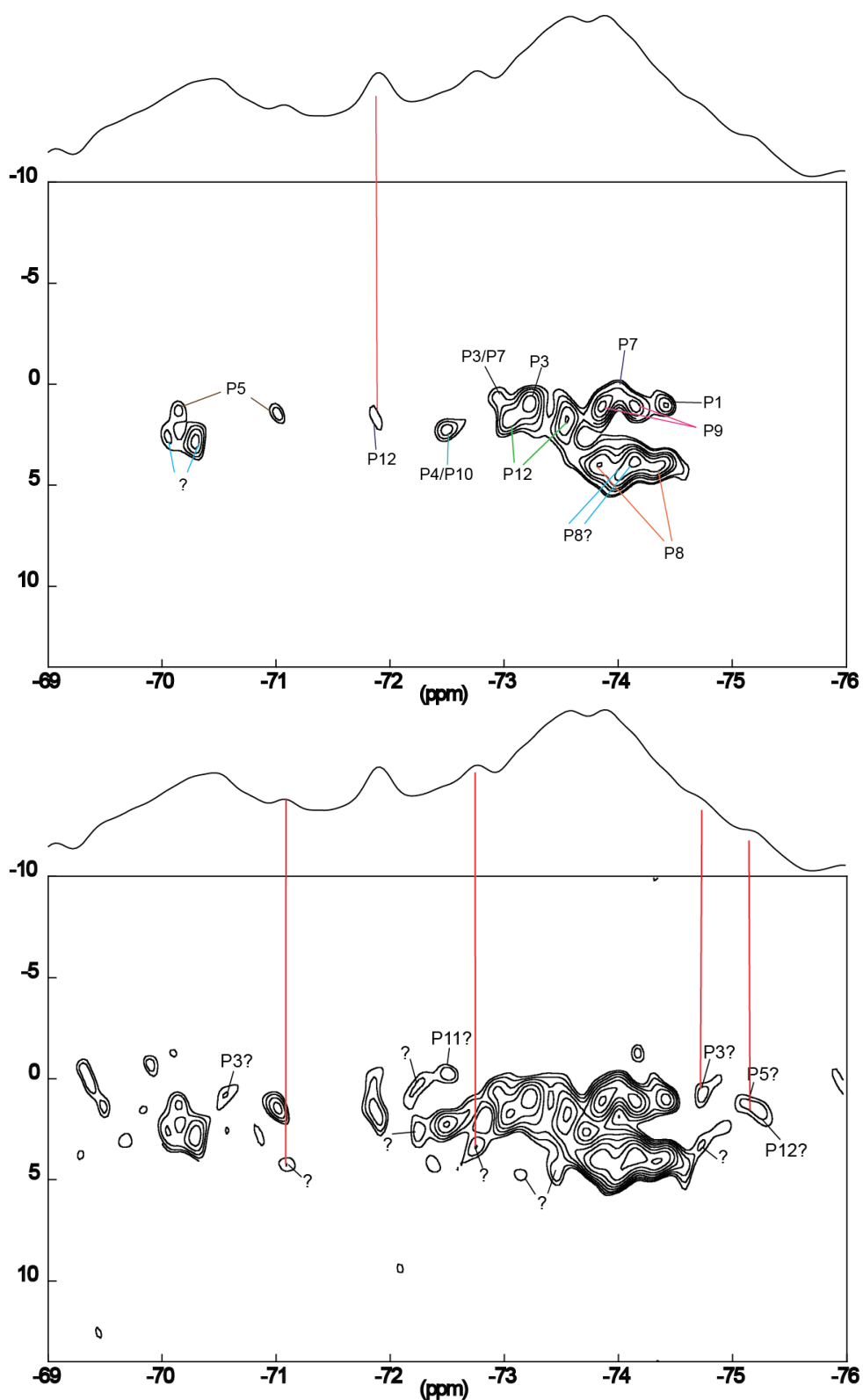
Figure 5.8: (top) A detailed plot of the $^{31}$P-$^{29}$Si HETCOR experiment showing the most likely P sites in the structure that are correlating to the individual $^{29}$Si shifts, those marked by a ? are uncertain as their $^{31}$P chemical shifts are no longer related to that of $\alpha$-TCP (bottom) The same spectrum but shown nearer the baseline, sites are tentatively assigned due to their similarity in intensity to the noise, again those with a ? are uncertain

The next regions considered are the three resonances with $^{31}$P chemical shifts between 1.01 ppm and 1.12 ppm. This area is a more complicated region to interpret as these resonances could belong to sites P1 or P9, or both. Again both sites have two nearest neighbours, P1 is close to P4 and P11 at 4.185 Å and 4.259 Å, respectively, while P9 is close to P7 at 4.249 Å and P12 at 4.3 Å. The $^{31}$P resonances at 0.44 ppm and 0.57 ppm, are associated with site P7 with closest neighbours P9 at 4.249 Å and P10 at 4.612 Å, associations with P10 would likely be very low in intensity, so this is probably P9. There are two $^{29}$Si resonances that correlate with site P5 at 1.2 ppm; these are -70.16 and -71.02 ppm and while the latter is slightly shifted from the actual P5 shift it is still closer than anything else. The closest sites to P5 are P8 at 4.118 Å and P3 at 4.291 Å. The last two resonances associated with existing crystal sites have a slightly ambiguous relationship with the $^{29}$Si shift -72.5 ppm, these belong to sites P4 or P10 at 2.22 ppm, though as it is of reasonable intensity it is likely to be P4, which lies close P1 at 4.185 Å distance where the Si could possibly be located. Though if it was P10 its nearest neighbour is itself at 4.47 Å and it would be expected to be lower in intensity. Lastly the $^{29}$Si resonance at -73.23 ppm can be associated with two $^{31}$P chemical shifts P3 and P2, though as with the case for P4/P10, the resonance is quite intense and as the closest neighbour to P2 is over 4.5 Å away, this can probably be ruled out in favour of site P3 which is 4.23 Å away from P5.

The last two well defined resonances are associated with $^{31}$P chemical shifts that are quite different from the original $\alpha$-TCP structure. This especially pertains to the Si-P correlations at -70.3 ppm/2.84 ppm, and another at 2.54 ppm is possibly new as well, or could be another site such as P4 that has shifted. This can be included in with the two resonances that have been provisionally associated with site P8, however it is possible these three latter peaks are related to their original position, as they have only moved by approximately 0.3 ppm. The less well defined resonances can be associated to either new resonances in some cases or the ones listed above, most of the new ones lying in the range between 2.5 ppm to 3.5 ppm; some around 4.3 ppm could be correlating with site P8. Amongst the less defined peaks there are two that can be loosely associated with P11 and P6, although these are very weak. This is understandable for P6 as there is nothing closer than 4.5 Å but P11 is very close to

P1 so a strong signal would be expected. Likewise, there is little evidence for sites P10 and P2, again though, P2 has nothing closer than 4.5 Å and might to be too distant to observe, P10 is only close to itself at almost 4.4 Å so any signal would be relatively weak if there at all. The more tentative correlations are marked on figure 5.8b

Of the eighteen correlations that were represented figure 5.7, fourteen of these can be classified with some certainty to within two positions in the unit cell. There are another three correlations, but these have substantially shifted and their assignment is less certain. The final resonance is at a $^{31}$P shift 2.84 ppm and this will be addressed later. The pressing question is can these correlations that have been outlined be used to describe a structure where there exists two non equivalent $SiO_4$ units sharing a bridging oxygen? The answer is yes, however it is possible that some positions have been identified that were not listed as one of the seven possible positions for $Si_2O_7^{6-}$ to form, if this is the case they are no longer bound by the structure symmetry, the results are summarised in table 5.1 and the most likely phosphorous sites that have been replaced by silicon are marked on figure 5.9.

Firstly those sites that were constrained by symmetry are dealt with easily. It was observed that some sites correlated with P12; P12 has closest neighbours P12 and P9, there are three of these correlations, the one at $^{29}$Si shift -71.98 ppm is quite weak compared to the other two, this is more likely to be P12 correlating with P12. Therefore half of the unit P12-P9 exists, there is also at least one $^{29}$Si peak correlating to P7, which is closest to P9, hence the whole unit P12-P9 has been identified. Two P7 sites and three P12 sites have been recognised, so it is possible that there is more than one configuration of this type. It can be stated that at least one of the P12 sites correlates with P9 at -73.58 ppm, making half of the unit P9-P7. There is no connection for P7 observed in the data because P9 (which is closest), has been replaced with Si and P10 is 4.61Å away so it would not necessarily be detected, especially if the distance between that P and the Si is greater than that in the original structure. Likewise it is the same for the position P5-P3 which exhibit correlations with P8, which is close to P5, but as before, nothing correlates with P3 because P5 has been replaced, and the next nearest to P3 is P6 at 4.76Å. A correlation characterised by a distance like this is not expected to be observed, one extremely tenuous correlation to P6 could exist.
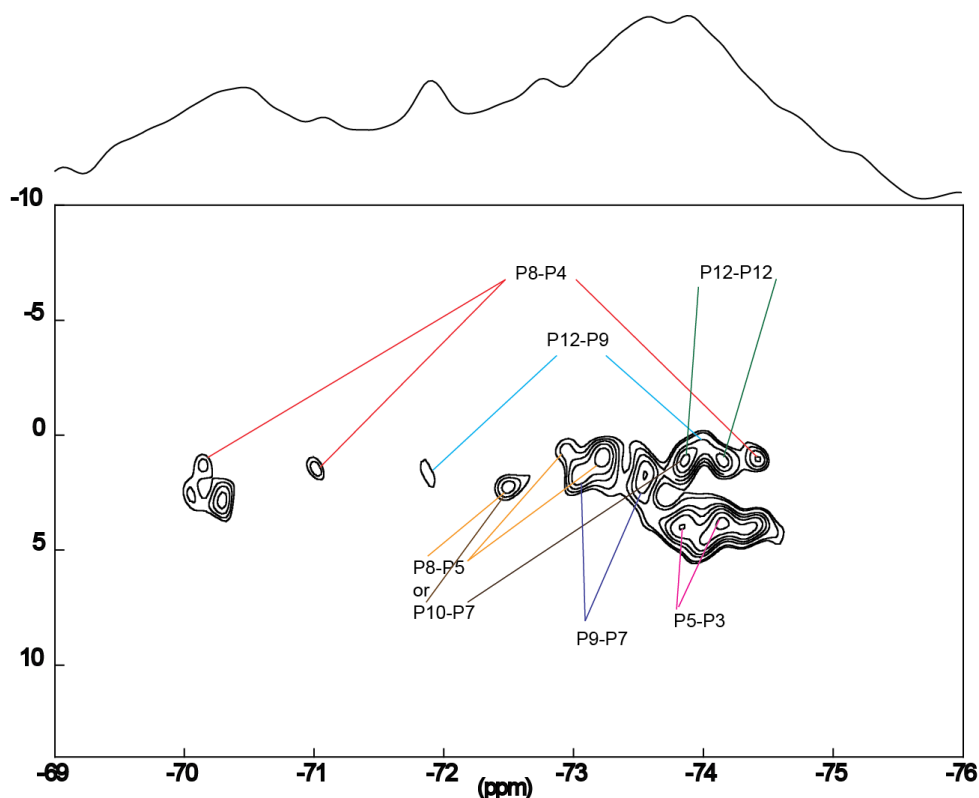
Figure 5.9: A detailed plot of the $^{31}$P-$^{29}$Si HETCOR, showing which phosphorous sites are most likely to have been replaced with a Si-O-Si unit and the corresponding resonances for each pair, in the case of P9-P7 and P5-P3 we do not expect a corresponding peak for either P7 or P3 as their next nearest neighbour is too far away for the experiment to detect

However, if that is the case P10 from the previous case should also be observed.

The next P site treated is represented by the resonance at 2.2 ppm, if this is site P4, then it should correlate with P8, forming the position P8-P5, where the $^{31}$P shift at site P3 correlates to the Si on position P5. If however, the 2.2 ppm resonance correlates to P10, then P10-P7 is obtained with P10 correlating to P10 and P9 at 1.12 ppm correlating with P7, though this is unlikely. Lastly, the two possible locations that are not constrained by symmetry, i.e. P8-P4 and P12-P12 are treated. The first one is quite simple as there is at least one correlation to P5 at 1.2 ppm observed which is nearest to P8, and P4 is closest to the correlation for the P1 shift at 1.05 ppm. Finally the resonances at 1.1 ppm could be considered to be P9 at 1.12 ppm, and if another at 1.1 ppm is also P9 then Si at P12-P12 is obtained as they would both correlate with a P9.

From this analysis four-five of the correlations discussed here were predicted by Yin *et al* , although P10-P7 was tentatively assigned this was not favoured by these authors and this result is more likely to be P8-P5. In this study no evidence for P4-P1 was observed, which was the $3^{rd}$ most energetically favourable correction given by Yin *et al.* In contrast, the two most energetically favourable correlations, P9-P7 and P5-P3 are observed. However, a correlation for one of the sites in both of these positions is not detected. In both cases P7's and P3's nearest neighbour has been replaced by Si and the next nearest site is probably too far away to be detected. The resonances that correspond to each of the positions in the unit cell are marked on Figure 5.9.

Although the majority of the major resonances associated to an $O^{2-}$ charge balance mechanism have been assigned, there are still correlations that remain unclassified. Firstly the $^{31}P$ resonance at $^{31}P$ 2.84 ppm has moved substantially from the shifts characterising the original structure, though perhaps what is more interesting is the Si shift that it corresponds to at -70.3 ppm [118], this shift corresponds to that of $\alpha$-dicalcium silicate ($C_2S$, $Ca_2SiO_4$). It has been reported in the literature that $C_2S$ forms a solid solution with $\alpha$-TCP at low levels of silicon incorporation [83], until it then separates into a separate silicocarnitite phase [110]. There have been no solid state NMR studies on such a compound, and below certain levels it is not detectable by XRD, (as the only phase that is seen is that of the $\alpha$-TCP). The solid solution was only detected indirectly through the use of SEM-WDS, so it is possible that it does exist within the sample studied here. In addition, while able to assign the $Q^2$ resonance to a pseudowollastonite type structure, the relationship of this peak to the structure was unable to be determined, it was observed to get more intense with increasing Si content. As mentioned in Section 5.3.3 the literature reports that psuedowollastonite can also exist as a solid solution with $\alpha$-TCP and vice-versa [119]

Previous research has found an apparent limit of 1.14 wt% for Si substitution in $\alpha$-TCP, before other phases start to form, (namely Ha) [85], The preparations in this study are characterised as Si-$\alpha$-TCP up to around 1.8 wt%, with the most studied possessing $\sim$ 1 wt%, Though substantial evidence for a charge balance mechanism involving $O^{2-}$ vacancies has been found, the calculations by Yin *et al.* suggests that this mechanism results in a less stable structure once the silicon goes above two $SiO_4$

units per unit cell. The calculations undertaken in this study indicated instability even for two units, however both series of calculations also demonstrated a shrinking of the lattice, in disagreement with the results from XRD obtained [107]. Both computational studies did show that $Ca^{2+}$ excess was the more stable mechanism, and the system became even more stable once the Si was introduced; furthermore it was also found that lattice parameter variations are similar to that observed from the XRD studies. Based on the experimental evidence presented within, we tentatively propose a solution where the charge balance mechanism consists of mostly $O^{2-}$ vacancy formation but a small amount of $Ca^{2+}$ excess is also present.

As discussed earlier, sample stoichiometry does not cater for $Ca^{2+}$ excess in these samples. However $Q^2$ units are present in the sample, albeit in small quantities and they appear composition dependant. The sample has a measured Ca/P+Si ratio of around 1.51 from XRF data, with the nominal ratio being 1.5. Therefore, the substitution of Si for P and subsequent charge balancing in Si-$\alpha$-TCP is thought to take place as

$$3Ca^{2+} + 2PO_4^{3-} \rightarrow 3Ca^{2+} + 2SiO_4^{4-} \rightarrow 3Ca^{2+} + Si_2O_7^{6-} + O^{2-} \qquad (5.1)$$
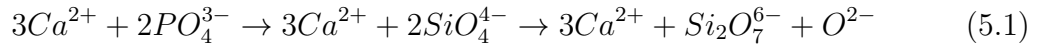
with the excess $O^{2-}$ lost during sintering. It is not possible to maintain this sample stoichiometry with the formation of $CaSiO_3$, as this results in an excess of $1.5Ca^{2+}$ for every three $CaSiO_3$ units formed

$$4.5Ca^{2+} + 3PO_4^{3-} \rightarrow 4.5Ca^{2+} + 3SiO_4^{4-} \rightarrow 3Ca^{2+} + Si_3O_9^{6-} + 1.5Ca^{2+} + 3O^{2-} \quad (5.2)$$
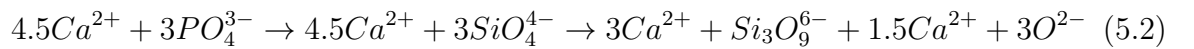
again with the $O^{2-}$ lost during sintering. There is no evidence of other calcium phosphate phases present in the sample to account for this excess calcium, as even at relatively low quantities these would be detectable in the $^{31}$P MAS NMR spectrum. There is however, tentative evidence for $C_2S$ in the sample, $C_2S$ is only able to form in these samples if there is extra $Ca^{2+}$ around, which by itself would not be normally be possible. As seen below when sample stoichiometry is taken into account there is a deficiency of $0.5Ca^{2+}$ per $C_2S$ unit

$$1.5Ca^{2+} + PO_4^{3-} \rightarrow 1.5Ca^{2+} + SiO_4^{4-} \qquad (5.3)$$
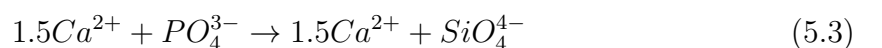
However, when both the formation of $CaSiO_3$ and $C_2S$ are considered together the sample stoichiometry is maintained. The formation of either $CaSiO_3$ or $C_2S$ will result in $Ca^{2+}$ excess or $Ca^{2+}$ deficiency respectively, in parts of the structure, and the formation of the other component is necessary to overcome this charge imbalance. The formation of every $Ca_3Si_3O_9$ unit gives enough $Ca^{2+}$ excess to form three units of $C_2S$. Therefore, when these above factors are taken into consideration, the formation of $CaSiO_3$ and $C_2S$ within the Si-$\alpha$-TCP preparation maintains the sample charge balance and the sample stoichiometry of Ca/P+Si at 1.5

It would appear that the solid state NMR evidence is suggesting that a component of the sample is $O^{2-}$ deficient as indicated by the presence of $Q^1$ and $Q^2$ species. There is also evidence for the two high temperature compounds $\alpha$-$C_2S$ and $\alpha$-$Ca_3Si_3O_9$ and they both can exist as a solid solution with $\alpha$-TCP. This points to a much more complex scenario occurring than first anticipated, and although no direct evidence for charge balancing $SiO_4^{4-}$ through $Ca^{2+}$ excess has been found, it can not be ruled out completely. If the formation of a $Ca_3Si_3O_9$ -type structures does occur then this will also create some calcium excess, resulting in the formation of $C_2S$ to maintain electroneutrality, therefore allowing for the possibility of a unit cell to have $O^{2-}$ vacancies *and* $Ca^{2+}$ excess. Therefore, if both of these mechanisms are contributing then a stable structure predicted by the $Ca^{2+}$ excess calculations and smaller unit cell expansion as determined by XRD refinement are simultaneously possible.

## 5.4   Conclusions

The $^{31}$P MAS NMR results for Si-$\alpha$-TCP show that even with relatively small levels of Si substitution significant localised disorder is introduced to the structure. It is found that this disorder due to Si incorporation has a markedly greater effect on the resolution than that of the various impurities that can be in the sample, and that the $^{31}$P nucleus has limited use as a probe into the nature of Si-$\alpha$-TCP.

It has been shown through the use of $^{29}$Si enriched samples that good quality MAS NMR data can be collected and good resolution gained. However, qualitative analysis is very difficult in this case due to there being so many overlapping silicon resonances.

It was found that despite the published data in the literature, it was impossible to distinguish between $Q^0$ and $Q^1$ species in the structure. However, through the use of the refocused-INADEQUATE experiment it was found that $Q^1$ species can exist in the range of -68 to -76 ppm and are previously unreported.

It has been shown that while time consuming, complex 2D experiments ($^{31}$P-$^{29}$Si HETCOR) are possible on the Si-$\alpha$-TCP structure and qualitative information about the distribution of silicon in the Si-$\alpha$-TCP structure is obtained. It is seen that the underlying structure of $\alpha$-TCP largely still exists, and it can be stated with some confidence that the silicon goes to specific places within the structure, and that the majority of these positions agree reasonably well with DFT calculations done on the same structure. Furthermore, the locations and arrangement of Si in the Si-$\alpha$-TCP structure reveal that the charge balance mechanism is through the formation of $O^{2-}$ vacancies by the creation of an $Si_2O_7^{6-}$ unit for the loss of every two $PO_4^{3-}$ units.

While major advances have been made in understanding the distribution of silicon in the Si-$\alpha$-TCP and the nature of the charge balance mechanism determined, there remain some contradictions and unanswered questions. Mainly in the nature of how the observed lattice parameters from XRD do not agree with those from the DFT calculations for the same charge balance mechanism, neither does the more energetically favourable charge balance mechanism of $Ca^{2+}$ excess present itself. However, the formation of a $Q^2$ psuedowollastonite type structure and possible evidence for a $C_2S$ type structure, existing as solid solutions within the $\alpha$-TCP structure, allows for the possibility that there is dual process of charge balancing present, consisting mostly $O^{2-}$ vacancies with some $Ca^{2+}$ excess. However, in order to clarify these points, further investigations need to be undertaken.

# Chapter 6

# $^{43}$Ca MAS and DOR NMR of $\alpha$-TCP and Silicon Substituted $\alpha$-TCP with First Principles Calculations

## 6.1 Introduction

Calcium is one of the most abundant elements on earth, and is found in various quantities in different forms of matter. Its most common form is a 2+ cation, it is found in large quantities in rock and soil, dissolved in sea water and it is used in the manufacture of cement and some types of glass [129–131]. Calcium is also found to be a significant component in biological systems, such as the inorganic phosphate phase of bones in mammals, which is predominantly a calcium phosphate phase [11]. Calcium and its surrounding environments are difficult to study, and these characteristics are largely limited to single crystal and powder X-ray diffraction, however as Ca is commonly found in glassy and amorphous materials these characterisation options no longer remain viable. Solid state NMR is the ideal tool of choice when studying such local chemical environments but in the case of looking at calcium there are large hurdles to overcome.

Of the stable isotopes of Ca, only $^{43}$Ca possesses a nuclear spin $I > 0$ which is observable by NMR. Unfortunately $^{43}$Ca is only 0.135% [51] abundant making the acquisition of spectra with a decent signal to noise difficult. This is hampered further by it being a quadrupolar nucleus with nuclear spin $I = 7/2$, which results in broadening of the spectrum due to the second order quadrupole interaction. Furthermore $^{43}$Ca belongs to a group of nuclei that are known as low gamma, and these nuclei have very small gyromagnetic moments resulting in very low sensitivity. At 14.1T $^{43}$Ca has a low resonance frequency of 40.34 MHz compared to that of $^{1}$H 600 MHz. Signal acquisition can also be limited by acoustic ringing, thus the study of low gamma nuclei often requires specialist probes that can be tuned to low frequencies. The nuclear quadrupole moment can be quite large for low gamma nuclei which can in turn significantly broaden the solid state NMR spectrum at lower magnetic fields, though in the case of $^{43}$Ca the nuclear quadrupole moment is fortunately quite small. In addition, due to the weak dipolar couplings with surrounding nuclei the MAS requirements for solid state NMR measurements on $^{43}$Ca are quite modest, and the main focus is larger volume rotors to maximise the signal-to-noise.

Over the last decade or so, substantial progress has be made in being able to acquire meaningful data from the $^{43}$Ca isotope. Initial studies were done on expensive enriched samples with $^{43}$Ca $> 50\%$ [132–134], but with the advent of higher field magnets which induce more favourable Boltzmann factors and high volume rotors, it is possible to record natural abundance spectra in a couple of days [135], this however is somewhat dependant on pulse delays as tens of thousands of repeat scans are often needed. It has been demonstrated that with very high fields and special pulse sequences, such as the rotor assisted population–transfer (RAPT) [136] sequence, that good quality data can be collected in 4 mm probes in 48 hours [39]. Other techniques have been used such as cross polarisation (CP) from protons, but due to weak dipole couplings this approach places significant stress on the hardware [40]. However, due to the line broadening caused by second order quadrupole interactions, these spectra can exhibit poor resolution due to overlapping resonances. Therefore the elucidation of isotropic chemical shifts ($\delta_{iso}$) and quadrupolar coupling constants ($C_Q$) can be difficult. However, in the case of multiple sites, experimental techniques such as multiple-quantum-magic-angle-

spinning (MQMAS) [137] have been used to resolve isotropic shifts and the $C_Q$ [138], though the use of this technique strictly demands the use of $^{43}$Ca enrichment techniques.

With the limitations on resolution of $^{43}$Ca NMR spectra, either through the difficulties of natural abundance experiments or with the expense of enriched samples, it has nevertheless been possible to show a relationship between the $^{43}$Ca isotropic chemical shift and the structure of the surrounding environment. Dupree *et al* [139] in a study of several calcium containing compounds at natural abundance, were able to determine a relationship between the average Ca-O distance of the first coordination sphere and the isotropic shift. The study showed that while there was a linear correlation of isotropic chemical shift with distance (of 280 ppm/Å), these data were also affected by next nearest neighbour interaction. While the gradient did not appear to change with chemical composition, a change in the intercept was detected that facilitated a range of chemical shifts to be observed between the different types of compound. A study by Lin *et al* [140] showed that there was also a correlation between the oxygen coordination number and the isotropic shift. While there was some overlap between regions, it was found that six coordinated would be at a more positive shift and moving to a more negative shift with increasing coordination number. They also confirmed a linear relationship between shift and average Ca-O distance of 262 ppm/Å. Again the slope would remain the same, but the intercept changed between different families of compounds, whether it was silicate/aluminates or oxides, again demonstrating that next nearest neighbour effects can influence the chemical shift range.

A large study by Gervais *et al* [41] using experimental and GIPAW DFT first principles calculations for a large range of borates, silicates, aluminates, phosphates and carbonates demonstrated a reasonable correlation between the calculated and experimental isotropic chemical shift and quadrupole parameters. They also established a linear relationship between isotropic chemical shift and average Ca-O bond length and that the shift values moved to a more negative value for increasing Ca-O distance. In addition to movement of the intercept the gradient was also found to be different for each group of compounds indicating values of 300 ppm/Å for silicates, 190 ppm/Å for phosphates, 310 ppm/Å for aluminates and 810 ppm/Å for borates Further studies by

Wong *et al* [141] again demonstrated this near linear relationship between shift and Ca-O bond distances for aluminates, and silicates as well as some organic and inorganic calcium containing compounds. Bryce *et al* [142] were also able to show that first principles DFT calculations of quadrupolar and chemical shift tensors (and associated anisotropies) on the $CaCO_3$ system were in good agreement with the available experimental data.

Despite advances in the acquisition of $^{43}Ca$ solid state NMR data, resolution still remains a problem in 1D experiments. The low $C_Q$ central transition resonance with low signal-to-noise often gives featureless lineshapes, this becomes extremely problematic when multiple sites are involved. However, in recent years MQMAS has shown promise in resolving multiple calcium sites in both crystalline and amorphous materials. For the first time it has been able to unambiguously resolve both sites in hexagonal hydroxyapatite [40]. Similarly 3MQMAS, 5MQMAS and 7MQMAS studies at very high fields has shown that the multiple sites in amorphous calcium silicate slags could be resolved, and it was possible to determine isotropic shifts and $C_Q$ values [143–145]. However due to the low sensitivity of the MQMAS experiment, these experiments required a significant amount of $^{43}Ca$ enrichment.

$^1H$–$^{43}Ca$ Correlation spectroscopy has also been performed by Wong *et al* [146] on an enriched sample using the 3Q-REDOR and $R^3$-HMQC experiments. This study showed the connectivity between the Ca and H in hydroxyapatite, and found that the $R^3$–HMQC was the more efficient experiment of the two in preference to the more conventional cross polarisation type experiment.

While some progress has been made, there are still limitations in the study of crystalline samples that contain many sites. Some materials such as $\alpha$-tricalcium phosphate [1] ($\alpha$-TCP), which contains eighteen unique calcium sites or some of the calcium silicate phases, such as the triclinic form of tricalcium silicate [147] which possess twenty nine unique calcium crystal sites, present major challenges. A study by Moudrakovski *et al* [148] illustrated this problem at natural abundance. However, even with $^{43}Ca$ enrichment, there is still going to be significant overlap of peaks. These types of structures quite often exhibit large unit cells and thus pose themselves as very large computational challenges due to the substantial computing resources required [135].

There is one technique, that has never been reported in the literature as having never been attempted on any $^{43}$Ca system, and that is double angle rotation or DOR [57] (see chapter). DOR has shown to be highly successful at removing the broadening due to second order quadrupole interactions. Essentially it is implemented as a 1D experiment but it has also been demonstrated to function in 2D experiments such as MQDOR [58]. Previous $^{17}$O studies have shown that DOR is capable of resolving up to eight overlapping sites [149]. As $^{17}$O is a spin $I = 5/2$ nucleus which potentially suffers from poor resolution due to multiple overlapping quadrpole broadened resonances. The removal of the second order quadrupole broadening reduces the linewidth so that it becomes comparable to that of spin $I = 1/2$ nuclei and it thus becomes possible to determine the isotropic shift and P$_Q$ values for the individual sites. The DOR sample volume is quite modest and is comparable to that of a 3.2 mm rotor, hence sample enrichment is still required, though, as reported within, the $^{43}$Ca enrichment levels do not need to be much greater than 10% $^{43}$Ca to obtain adequate signal-to-noise.

## 6.1.1   Calcium Environments in $\alpha$-TCP

As observed in Chapter 4.2, the structure of $\alpha$-tricalcium phosphate ($\alpha$-TCP, $Ca_3(PO_4)_2$) is large and quite complex [1]. There are eighteen distinct calcium crystallographic sites in the unit cell and these are found in two different types of environment, twelve of which lie in the cation columns and the remaining six lie in the cation-anion columns. The structure is also slightly unusual, as it has a large variation in the number of calcium-oxygen coordination numbers, with two five-coordinated sites, four six-coordinated sites, ten seven-coordinated sites, one eight-coordinated site and one nine-coordinated site.

As well as the large variation in Ca coordination numbers, the geometries of the Ca-O moieties are also found to be quite varied. The most commonly observed is a pentagonal bi-pyramid structure, with the equatorial plane lying approximately perpendicular to the direction of the column and the least observed is a hexagonal bi-pyramid. Each calcium geometry, is either edge or corner connected to five or six $PO_4$ tetrahedra, except for Ca14 which is only connected to four $PO_4$ tetrahedra. A sum-

mary of the coordination and geometries can be found in Table 6.1, with a graphical illustration of the geometries and $PO_4$ connectivity given in Figure 6.1.

Table 6.1: Details of the various calcium crystal sites, with average Ca-O distance and types of tetrahedral connections for each calcium coordination sphere

| Crystal site | Coordination number | Geometry from [1] | Number of $PO_4$ edges | Number of $PO_4$ corners | Average Ca-O distance(Å) from [1] | Average Ca-O distance(Å) calculated |
|---|---|---|---|---|---|---|
| Ca1 | 7 | a | 2 | 3 | 2.4554 | 2.4912 |
| Ca2 | 7 | c | 2 | 3 | 2.4630 | 2.5100 |
| Ca3 | 7 | a | 1 | 5 | 2.4369 | 2.4897 |
| Ca4 | 6 | d | - | 6 | 2.3484 | 2.4028 |
| Ca5 | 7 | d | 2 | 3 | 2.5190 | 2.5598 |
| Ca6 | 8 | a | 3 | 2 | 2.5194 | 2.5737 |
| Ca7 | 9 | b | 4 | 1 | 2.5814 | 2.6297 |
| Ca8 | 7 | c | 2 | 3 | 2.4802 | 2.5317 |
| Ca9 | 6 | d | - | 6 | 2.3731 | 2.4223 |
| Ca10 | 6 | d | - | 6 | 2.3428 | 2.3968 |
| Ca11 | 5 | e | - | 5 | 2.3482 | 2.3938 |
| Ca12 | 7 | a | 2 | 3 | 2.4538 | 2.4878 |
| Ca13 | 7 | a | 2 | 3 | 2.4404 | 2.4771 |
| Ca14 | 7 | c | 3 | 1 | 2.5160 | 2.5670 |
| Ca15 | 7 | a | 1 | 5 | 2.3925 | 2.4399 |
| Ca16 | 6 | d | - | 6 | 2.3400 | 2.3891 |
| Ca17 | 5 | e | - | 5 | 2.3801 | 2.4321 |
| Ca18 | 7 | a | 2 | 3 | 2.4242 | 2.4733 |

The Ca ions in the cation-anion columns of the $\alpha$-TCP structure have a Ca-O coordination number of at least seven. All of these sites are pentagonal bi-pyramidal except the nine coordinated site (Ca7), which is a hexagonal bi-pyramid. All of these calcium geometries connect to five different $PO_4$ tetrahedra and all involve at least two edge connections to a $PO_4$ tetrahedron, with the majority having two edge and three corner sharing arrangements, except the eight coordinated site which has three edge and two corner connections and the nine coordinated site which has four edge and one corner sharing arrangement to the $PO_4$ tetrahedra.

The Ca ions in the cation-cation columns have Ca-O coordination numbers between five and seven, and are found to exhibit much more varied geometries than those in the cation-anion columns. The most common geometry encountered is a distorted octa-
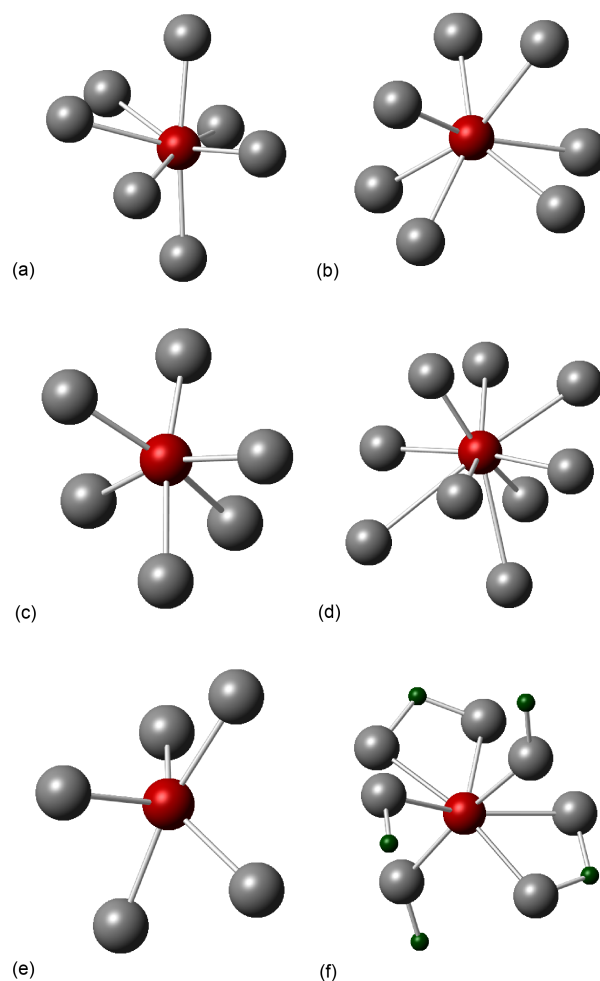
Figure 6.1: Graphical depiction of the different calcium-oxygen geometries and tetrahedral connectivity, (a) seven coordinated pentagonal bipyramid (b) seven coordinated irregular polyhedron (c) six coordinated distorted octahedron (d) nine coordinated hexagonal bipyramid (e) five coordinated trigonal bipyramid and (f) edge and corner connections to $PO_4$ tetrahedra.

hedron, then irregular polyhedron, pentagonal bi-pyramids and trigonal bi-pyramids. As with the more varied geometries in the cation-cation columns, the connections to the $PO_4$ tetrahedra are also more varied, and linkages to either four, five or six $PO_4$ tetrahedra are evident. The five and six coordinated Ca sites only corner share to the $PO_4$ units, with five and six connections respectively. The greatest variation in $PO_4$ connectivity is found to be associated with the seven coordinated Ca in cation columns. In these cases Ca3 and Ca15 connect to one edge and five corners, Ca2, Ca5 and Ca8 connect to two edges and three corners and Ca14 connects to three edges and one corner.

## 6.2  Experimental

### 6.2.1  Sample Preparation

Sample synthesis was undertaken by Dr. Jo Duncan from the University of Aberdeen as outlined in Chapter 4.3.1, the only differences being: For a stoichiometric, $^{43}$Ca isotopically enriched, $\alpha$-TCP sample, a mixture of $CaCO_3$ and 50% $^{43}$Ca enriched $CaCO_3$ were used in conjunction with $CaHPO_4$, so that $^{43}$Ca comprised 10% of the total calcium inventory in the end product and the Ca/P ratio of 1.5 was maintained throughout.For the Si-substituted $\alpha$-TCP preparation $(Ca_3(PO_4)_{2-x}(SiO_4)_x)$, $^{29}$Si and $^{43}$Ca isotopically enriched, Si-TCP (x = 0.10 / Si = 0.91 wt%) sample, solid-state, isotopically enriched $SiO_2$ (99.33% $^{29}$Si,) was used as the source of silicon at the expense of phosphorus-containing $CaHPO_4$ phase with the reduction in calcium compensated for by addition of more $CaCO_3$ to maintain the bulk Ca/(P+Si) ratio at 1.5. The $CaCO_3$ used was also a mixture of $CaCO_3$ and 50% $^{43}$Ca enriched $CaCO_3$ so that $^{43}$Ca comprised 4.1% of the total calcium in the product.

### 6.2.2  Calculations

The methods used in the GIPAW DFT calculations undertaken by Dr. David Quigley from the University of Warwick are outlined in Chapter 4.3.2

### 6.2.3  Solid State NMR Experiments

Natural abundance $^{43}$Ca MAS experiments were performed on a Bruker Advance II 600 MHz spectrometer, using a Varian 9.5 mm HX low gamma probe. The pulse width was calibrated to liquids pulse length of $\pi/4 = 7\mu s$ using a saturated solution of CaCl , a recycle delay of 2.5 s was used for 40000 repeat scans, with a MAS rate of 3.5 kHz, and referenced to 1 M solution of CaCl at 0 ppm.

$^{43}$Ca MAS experiments were performed on a Bruker Advance 3 850 MHz spectrometer with a Bruker 4 mm HX low gamma probe, using an MAS speed of 10 KHz, a liquids $\pi/4$ pulse giving a pulse length of 3 $\mu$s determined using a saturated solution of CaCl, a recycle delay of 2.5 s was used for 6000 repeat scans, and referenced to 1 M

solution of CaCl at 0 ppm.

$^{43}$Ca DOR experiments were performed at 20 T ($\nu_0 = 57.22$ MHz), 14.1 T ($\nu_0 = 40.33$ MHz), and 11.7 T($\nu_0 = 33.65$ MHz) using Bruker Advance III 850 MHz, Bruker Advance II 600 and Bruker Advance III 500 spectrometers. At each field the DOR measurements were undertaken using Samoson designed HX(double resonance) DOR probes. The spinning speed achieved on all experiments was 1300 Hz for the outer rotor and 6500 Hz for the inner rotor. A recycle delay of 2.5 s was used in conjunction with $\pi/6$ pulse lengths of 3 $\mu$s. And all experiments were referenced to 1M solution of CaCl at 0 ppm.

## 6.3   Results and Discussion

### 6.3.1   $^{43}$Ca MAS NMR of $\alpha$-TCP

Figure 6.2 shows the natural abundance $^{43}$Ca MAS NMR spectrum for $\alpha$-TCP recorded at 14.1 T. While it is clear that there is discernible signal which may be arranged into two separate groupings, no further specific features are evident. The signal-to-noise remains very poor even after a twenty four hour acquisition, and the use of a large 9.5 mm rotor. This is a prime example of the difficulties associated with natural abundance $^{43}$Ca solid state MAS NMR, and while the $\alpha$-TCP represents a more extreme case, it perfectly illustrates the problem of studying samples that have multiple sites. Of course performing this measurement at a higher field presents many benefits as the signal strength would improve through a more favourable Boltzmann distribution, the chemical shift dispersion would be more favourable and second order quadrupole broadening would be reduced. However, Figure 6.2 shows a typical $^{43}$Ca example of a system that would not significantly benefit from these improved characteristics offered at a higher field, even if weeks of experimental averaging was possible.

Experiments have been done on natural abundance $^{43}$Ca systems that enhance the signal through attributes of the pulse sequences, such as CP type experiments [39] and the RAPT sequence [40]. In the $\alpha$-TCP case CP is not an option as there are no protons in the sample and it is not practical to use the $^{31}$P nucleus as the high $\gamma$
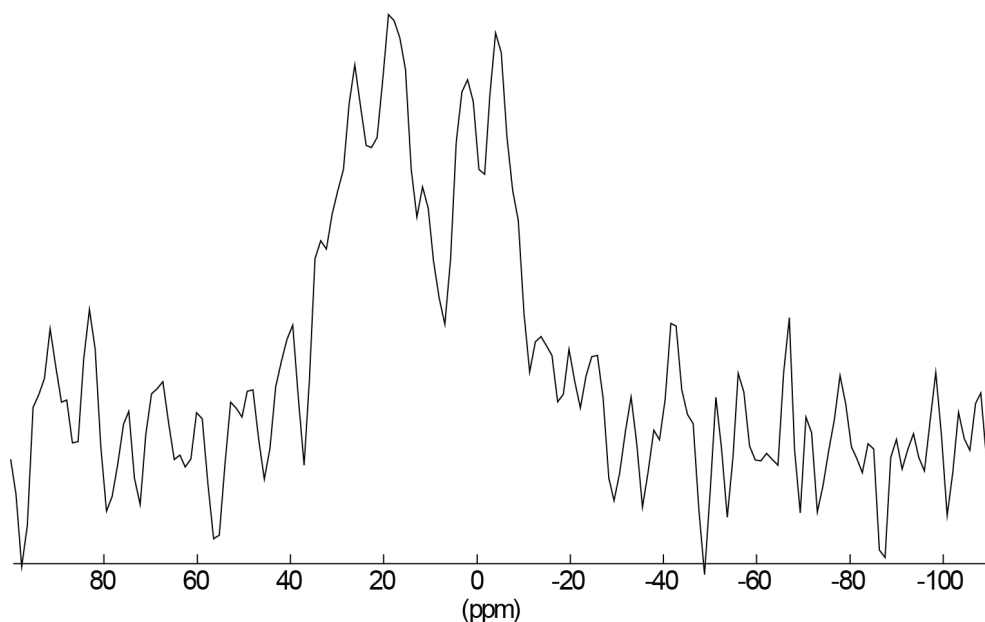
Figure 6.2: Natural abundance $^{43}$Ca MAS NMR of $\alpha$-TCP at 14.1 T in a 9.5 mm probe, demonstrates extremely poor resolution after 40000 scans

source in this instance, as there is only a very weak dipolar coupling between the two nuclei $^{31}$P and $^{43}$Ca. This is will put significant stress on hardware through the need for long contact times. The RAPT pulse sequence and high magnetic field strengths of 20 T, have demonstrated an ability to produce good results in terms of signal-to-noise for natural abundance $^{43}$Ca experiments on a monoclinic hydroxyapatite (not shown. Monoclinic hydroxyapatite has five independent Ca sites in its structure and very good signal to noise can be achieved in less than twenty four hours, though in this case the pulse delays of 0.2 s are considerably shorter than that of $\alpha$-TCP at around 2.5 s. However, there is still the problem of broadening due to second order quadrupole effects even though the C$_Q$s are generally quite low. The $^{43}$Ca resonances are generally featureless and cover a limited chemical shift range, making interpretation of the data impossible as it is not possible to separate the individual resonances form one another. As demonstrated below, this really is a limiting factor, as even for $^{43}$Ca enriched $\alpha$-TCP samples poor resolution/resonance overlap still remains a problem.

Figure 6.3a shows $^{43}$Ca MAS NMR data for $\alpha$-TCP at 20 T. The benefits of using $^{43}$Ca enrichment in this study become immediately clear when this data is compared to the 14.1T natural abundance data shown in Figure 6.2. The enriched sample (while

not heavily enriched), exhibits good signal-to-noise in a reasonable acquisition time of around six hours, even when studying a modest sample volume in a 4 mm rotor. While many features are now visible, the spectrum still suffers from poor resolution, primarily due to the sheer number of Ca sites involved and the second order quadrupolar broadening of each resonance. Despite the poor resolution in this $^{43}$Ca MAS spectrum there are two features in the spectrum that can be separated from the bulk. These are the resonances at the most downfield/highest ppm value and the most upfield/lowest ppm extremes of the spectrum, however unambiguous data such as $\delta_{iso}$, C$_Q$ and $\eta$ values are still not able to be extracted from these lineshapes.

The extensive resonance overlap demonstrated in the $^{43}$Ca MAS NMR of Figure 6.3a is corroborated by the simulated MAS spectrum generated from the GIPAW DFT calculated NMR parameters for $\alpha$-TCP (see Figure 6.3b and Table 6.2). While it is not an identical replication of the experimental spectrum it does cover a very similar shift range and has a similar overall shape. The differences for the isotropic shift are expected to be low; indeed, DFT calculated and experimental NMR data for simpler structures in the literature have been shown to correlate reasonably well [41] [142]. From Table 6.2 there appears to be some discrepancies with the C$_Q$ parameters which will be dealt with below. At this stage it is impractical to draw any conclusions to the assignment of the crystal sites to specific resonances, and Table 6.2 indicates (from the predicted $\delta_{iso}$ values) that many resonances are expected to lie within one or two ppm of at least one other resonance. However, based on the DFT calculations, the isolated upfield (i.e. the most negative) resonance can probably be assigned to the site Ca5 as it is significantly shifted from the rest.

The literature does not provide an abundance of information that allows the $^{43}$Ca MAS data and the DFT calculations to be rationalised to particular environments, nevertheless some general observations can still be made. From the full breadth of the experimental and the calculated $^{43}$Ca chemical shift ranges shown in Figure 6.3 and Table 6.2, it can be established that they span $\sim 30\%$ of the entire reported $^{43}$Ca chemical shift range which is around 200 ppm [41]. Indeed this chemical shift range of $\sim 60$ ppm is even greater than that which has been previously established for calcium phosphates which is currently reported at being $\sim 40$ ppm [41]. The literature noted
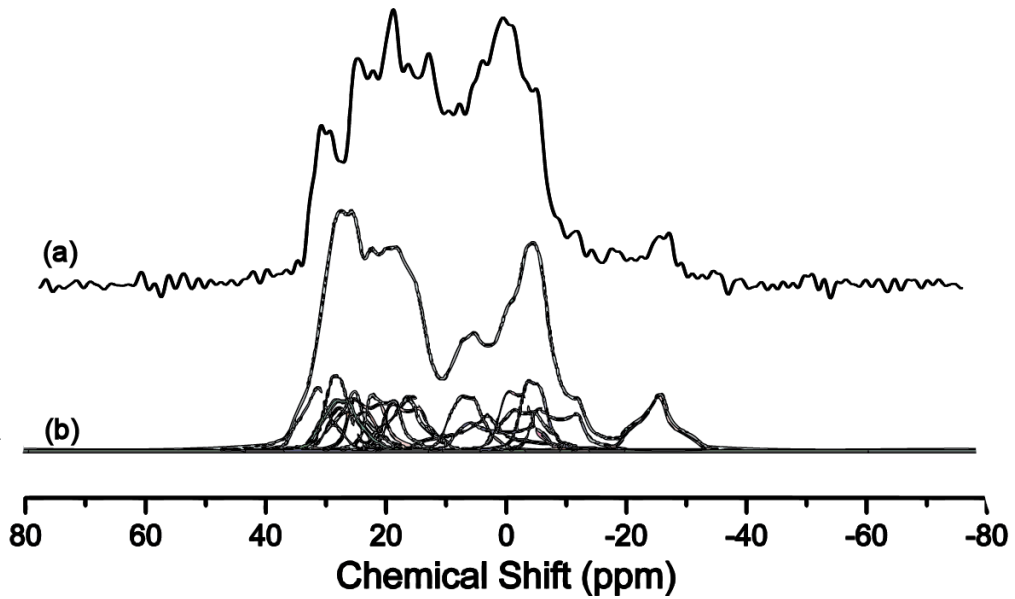
Figure 6.3: Comparison of (a) $^{43}Ca$ MAS NMR of 10% $^{43}Ca$ enriched $\alpha$-TCP at 20 T in a 4 mm probe, good signal to noise after 8000 repeat scans (b) simulated $^{43}Ca$ MAS NMR spectrum from GIPAW DFT calculations for $\alpha$-TCP showing the significant overlap of peaks

Table 6.2: Measured isotropic chemical shifts ($\delta_{iso}$) and $P_Q$ determined from the DOR experiments, along with the calculated GIPAW DFT parameters for each crystal site

| Experimental | Results | | Calculated | Paramaters | | |
|---|---|---|---|---|---|---|
| $\delta_{iso}$ | $P_Q$ | Site | $\delta_{iso}$ | $C_Q$ | $\eta$ | $P_Q$ |
| 33.46 | 2.142 | Ca13 | 37.81 | 2.176 | 0.8 | 2.397 |
| 32.39 | 3.028 | Ca18 | 34.09 | 2.443 | 0.55 | 2.563 |
| 30.20 | 3.034 | Ca6 | 33.15 | -2.779 | 0.27 | -2.813 |
| 26.93 | 2.75 | Ca16 | 32.69 | 1.856 | 0.48 | 1.926 |
| 26.77 | 3.012 | Ca10 | 32.41 | 2.256 | 1 | 2.605 |
| 24.65 | 3.395 | Ca12 | 29.34 | -2.494 | 0.16 | -2.505 |
| 21.71 | 2.976 | Ca4 | 26.02 | -2.365 | 0.12 | -2.371 |
| 18.37 | 3.056 | Ca1 | 23.88 | 2.528 | 0.78 | 2.773 |
| 20.24 | 3.415 | Ca15 | 23.21 | -2.622 | 0.22 | -2.643 |
| 19.29 | 3.584 | Ca11 | 22.04 | 2.339 | 0.63 | 2.489 |
| 13.74 | 4.604 | Ca7 | 16.29 | -3.341 | 1 | -3.858 |
| 13.51 | 4.866 | Ca9 | 12.65 | 3.833 | 0.19 | 3.856 |
| 9.80 | 3.121 | Ca2 | 11.69 | -2.298 | 0.48 | -2.385 |
| 5.48 | 2.597 | Ca14 | 3.89 | -2.793 | 0.45 | -2.886 |
| 2.14 | 2.983 | Ca8 | 2.67 | 2.185 | 0.33 | 2.224 |
| 2.53 | 3.32 | Ca17 | -1.23 | 1.949 | 0.33 | 1.984 |
| -0.01 | 2.469 | Ca3 | -1.85 | 2.94 | 0.32 | 2.990 |
| -19.40 | 3.422 | Ca5 | -19.55 | -2.459 | 0.9 | -2.771 |

that this shift range was for a considerable variety of calcium phosphate systems and that these compounds *included* hydroxyl groups and water. Therefore, it remains to be seen why a system such as $\alpha$-TCP containing only calcium and phosphate moieties is characterised by such a large shift range. In addition to this large diversity of chemical shifts, a concomitant large range of quadrupole parameters is expected. Table 6.2 shows that a range of $C_Q$ values spanning $\sim$ 1.5-4.5 MHz is evident which represents a significant distribution for the $^{43}$Ca nucleus; indeed, $C_Q$ values of $\sim$ 4.0 MHz are amongst the largest reported for this nucleus [150].

## 6.3.2 $^{43}$Ca DOR studies of $\alpha$-TCP

As demonstrated above, it is very difficult to get suitable levels of signal-to-noise and resolution from natural abundance $^{43}$Ca MAS NMR data. This situation is partially alleviated when enriched $^{43}$Ca is adopted, however the increased signal-to-noise does emphasize the resolution problem due to the overlapping second order quadrupole lineshapes when multiple sites have to be considered. With this in mind, and due to time constraints imposed by other resolution enhancing techniques which can be very insensitive such as $^{43}$Ca MQMAS, another experimental approach is required. This technique is Double Angle Rotation NMR (DOR) which essentially removes all second order quadrupole broadening by spinning the sample around two angles simultaneously (see Section 3.3). This technique has never been implemented for $^{43}$Ca studies before, though it has been shown to be a very powerful tool for studying nuclei such as $^{17}$O [151] , and $^{11}$B [152] in ordered systems where the chemical shift dispersion is minimal. The observed or *apparent* resonance in the DOR spectrum ($\delta_{DOR}$) does not appear at the isotropic shift ($\delta_{iso}$) position, rather it appears at the centre of gravity of the MAS spectrum. The shift of $\delta_{DOR}$ from $\delta_{iso}$ is called the quadrupole induced shift QIS, (see Section 2.5.3) and for a spin $I = 7/2$ nucleus these different shifts are related by the expression

$$\delta_{DOR} = \delta_{iso} - QIS = \delta_{iso} - \frac{1}{392}\frac{P_Q^2}{\nu_0^2} \quad (6.1)$$

Where $P_Q$ is the quadrupolar product,

$$P_Q = C_Q \sqrt{(1 + \frac{\eta_Q^2}{3})} \qquad (6.2)$$

From Equation 6.1 it is evident that $\delta_{DOR}$ is frequency dependant. By repeating the DOR measurement at different $\mathbf{B}_o$ field strengths (usually three) it is possible to determine $\delta_{iso}$ and $P_Q$ graphically. By plotting $\delta_{DOR}$ at each field against $1/\nu_0^2$ a straight line will be obtained where the intercept yields $\delta_{iso}$ and $P_Q$ can be calculated from the slope via the expression

$$slope = -10^6 \frac{P_Q^2}{392} \qquad (6.3)$$

This analysis is demonstrated in Figures 6.5 and 6.6.
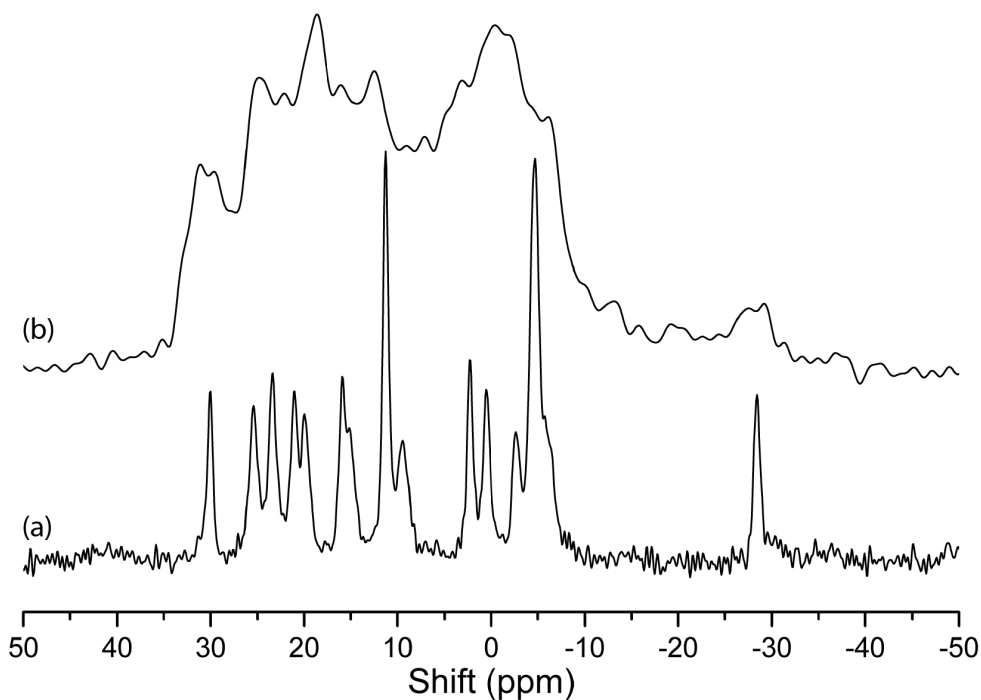


Figure 6.4: Comparison between $^{43}$Ca MAS (top) and $^{43}$Ca DOR (bottom) of $\alpha$-TCP at 20 T, DOR has removed all second order quadrupole broadening and all eighteen peaks have been resolved

Figure 6.4a shows the $^{43}$Ca DOR spectrum of $\alpha$-TCP obtained at 20T. It is obvious that a significant improvement to the resolution of the spectrum has been achieved in comparison to that of the corresponding MAS spectrum Figure 6.4b. The broad manifold of resonances spanning $\sim$ 4 KHz has been broken up into multiple lines of $\sim$ 50 Hz linewidth. As predicted by the $\alpha$-TCP crystal structure, eighteen $^{43}$Ca resonances are now evident; the double intensity resonance at $\sim$ 10 ppm is two overlapping lines which separate when the same experiment is repeated at a lower $\mathbf{B}_o$ field, and the broad intense resonance at $\sim$ –5 ppm (with two shoulders) is actually five resonances which is also verified by lower $\mathbf{B}_o$ field experiments. This is a highly significant result as it is represents the first $^{43}$Ca DOR experiment, it is the most lines obtained from a single DOR experiment, and this measurement reports the largest number of $^{43}$Ca signals obtained from a single (complex) system.
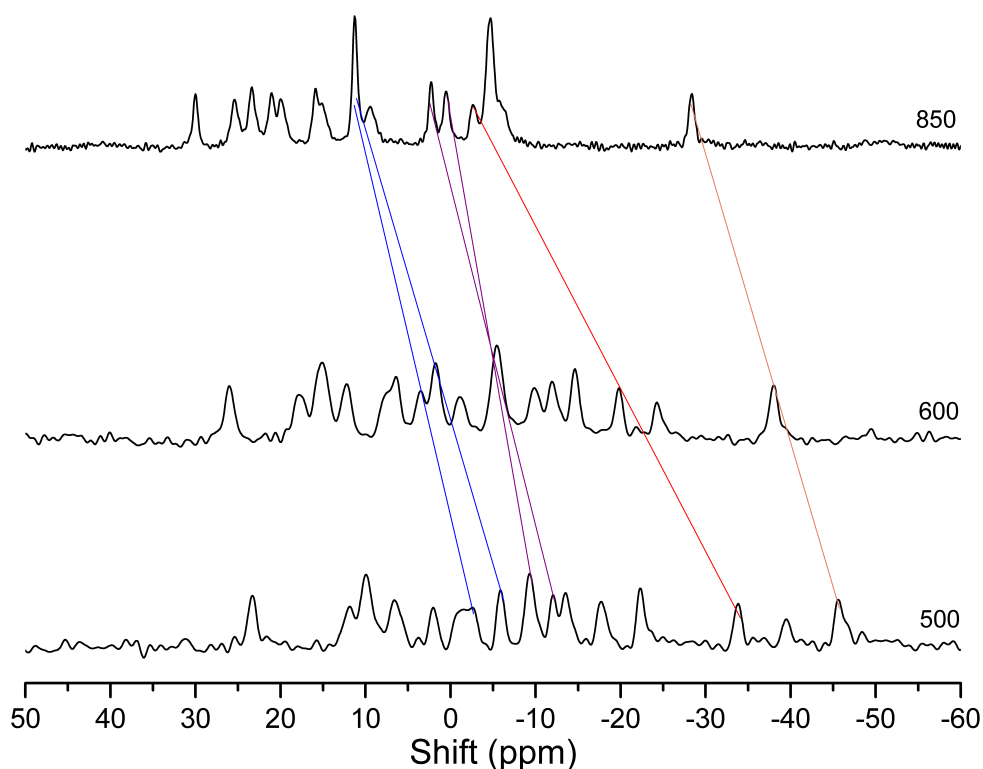


Figure 6.5: $^{43}$Ca DOR of $\alpha$-TCP at three different field strengths (top) 20 T (middle) 14.1 T (bottom) 11.7 T, demonstrating the field dependence of the DOR shift, some peaks move up to 30 ppm indicating some large $C_Q$ values. The coloured lines (not all are shown to avoid crowding) are to show how the peaks are related between fields due to differences in the $C_Q$ values. It can also be seen be seen that there is some cross over between fields making assignment tricky

Figure 6.5 shows the $^{43}$Ca DOR data acquired at three different magnetic fields (20 T, 14.1 T and 11.7 T) which has now unambiguously resolved all eighteen resonances. A large variation in the $\mathbf{B}_o$ dependence of these resonances is observed. Some resonances exhibit a change in $\delta_{DOR}$ of around 7-10 ppm while others shift by 30 ppm, thus indicating a substantial spread of C$_Q$s characterising the $\alpha$-TCP system. It is not possible to independently determine the C$_Q$ and $\eta$ values in this type of analysis as these parameters are degenerate as a product in the expression for P$_Q$.

After determining the corresponding resonances from the three different spectra (see Figure 6.5) then fitting each peak with a Gaussian line to determine their centre of mass, these $\delta_{DOR}$ values are then plotted against $1/\nu_0^2$ (Hz$^2$)to produce the graphical data of Figure 6.6. This method allows the field independent $\delta_{iso}$ to be read as the $y$ intercept, and the slope (multiplied by a spin-dependent constant) yields a value for P$_Q$. Figure 6.6 illustrates four examples from the $\alpha$-TCP structure which have been treated by this variable DOR analysis (not every line is included to avoid crowding). By executing this methodology for every resonance in the $\alpha$-TCP data, accurate values of $\delta_{iso}$ and P$_Q$ can be determined for every Ca site in the sample. These results are presented in Table 6.2.
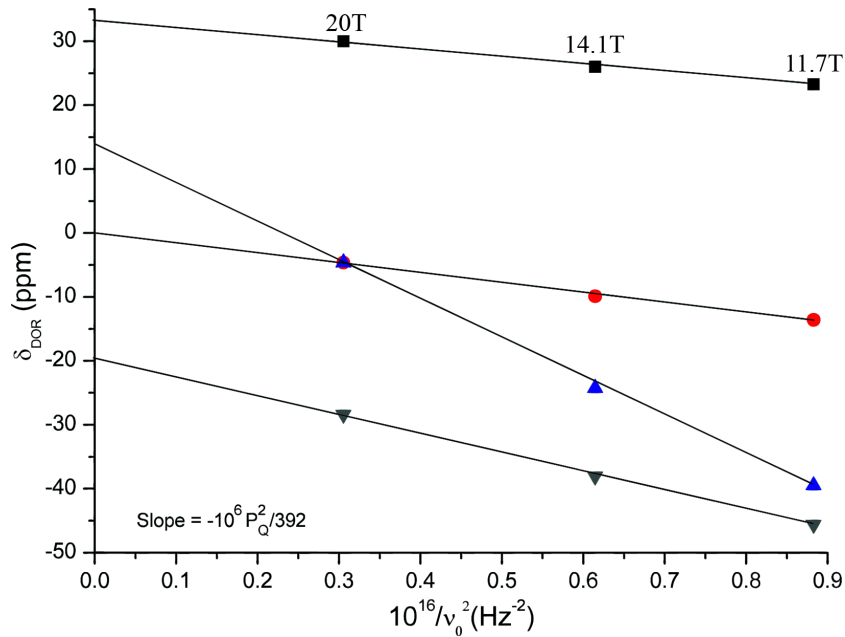


Figure 6.6: Plot of position against $1/\nu_0^2$ (Hz$^{-2}$) for some of the $^{43}$Ca resonances at different field strengths the slope gives P$_Q$ and the intercept gives the isotropic shift

### 6.3.2.1 Referencing the $^{43}$Ca Calculations

The isotropic shift information determined by experiment was used to reference the GIPAW DFT calculations so that they could be presented in terms of a referenced isotropic shift rather than as shielding relative to a bare atom. This is achieved by plotting the nuclear shielding ($\sigma_{calc}$) values from the calculations against the $\delta_{iso}$ values ascertained from the $^{43}$Ca DOR experiments at multiple $\mathbf{B}_o$ fields. A linear relationship was obtained, and the line of best fit yielded an intercept representing a value $\sigma_{ref}$ to reference the shielding, the slope is ideally -1 but is often found not to be the case [103]. This value is then used to determine the calculated isotropic shift $\delta_{calc}$ in the equation

$$\delta_{calc} = -1(\sigma_{calc} - \sigma_{ref}) \tag{6.4}$$

From Figure 6.7 below, the intercept $\sigma_{ref}$ was found to be 1170.1 and the slope was -1.06 for the $\alpha$-TCP data.
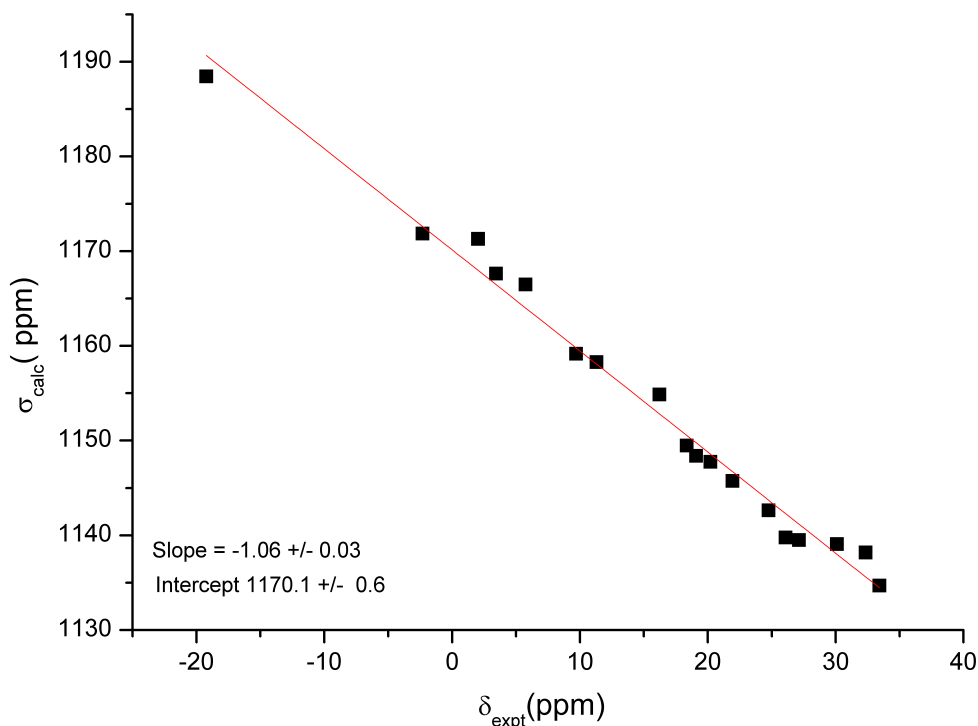


Figure 6.7: Plot of chemical shielding from the calculations $\sigma_{calc}$ versus the isotropic shift $\delta_{expt}$ determined by the DOR experiments so that the calculations can be presented in terms of isotropic shift values $\delta_{calc}$, the intercept gives a value for a shielding reference $\sigma_{ref}$, so that $\delta_{calc} = $ -Slope($\sigma_{calc}$ - $\sigma_{ref}$)

From Table 6.2 a systematic difference can be observed between the experimentally determined and GIPAW DFT calculated $P_Q$ values where the computed values appear consistently underestimated. This difference in $P_Q$ values obtained by calculations and experiment has been previously reported for [43]Ca studies which focussed on an underestimation in the $C_Q$ parameter [41] [142]. However, in similar calculations for [17]O and [35]Cl it has been observed that the $C_Q$ can be overestimated by as much as 10-20% [153] [154], though this discrepancy is not fully understood.

Figure 6.8 shows the plotted relationship between $\delta_{iso}$ and $P_Q$ for both the experimental and calculated data. The calculated data required all $C_Q$ values to be increased by 18 % to offset the underestimation that has been observed in $C_Q$, this value was determined by what provided the best overall correlation between the calculated and the experimental data in terms of $P_Q$.

Overall, despite the necessary increase in the $C_Q$ values, there is a good correlation between these experimental data and the calculated data. It is readily observed that these data break up into several natural groups, but unfortunately only a small number of the 18 resonances can be unambiguously assigned. In this representation two single isolated resonances are evident, in addition there are further groups of two, five and nine resonances. The outlying resonance at -19.4 ppm has already been assigned to Ca5 and there is very good agreement between the calculated and experimental values. The isolated resonance by itself at 33.45 ppm can tentatively be assigned to Ca16 based on the calculations, as this site exhibits the smallest predicted and measured $C_Q$. The group of two resonances at $\sim$ 14 ppm, represents the largest $C_Q$ values in $\alpha$-TCP (and are among the largest [43]Ca $C_Q$ values reported for any inorganic calcium phase), and these sites are corroborated by the DFT calculations. These sites can be assigned to Ca7 and Ca9 in the structure, but unfortunately there is no way of distinguishing further between the two. The remaining peaks can only be classified in their respective groups; the group of nine consists of Ca1, 4, 6, 10, 11, 12, 13, 15 and 18 while the of five consists of Ca2, 3, 4, 8, 14 and 17. However, it is possible that two of the resonances in the group of five are assignable, as the –0.01 ppm/2.469 MHz resonance and the resonance at 9.8 ppm/3.121 MHz resonance both exhibit an excellent correlation with the calculated value. Based on this correlation they are assigned to Ca17 and Ca2,
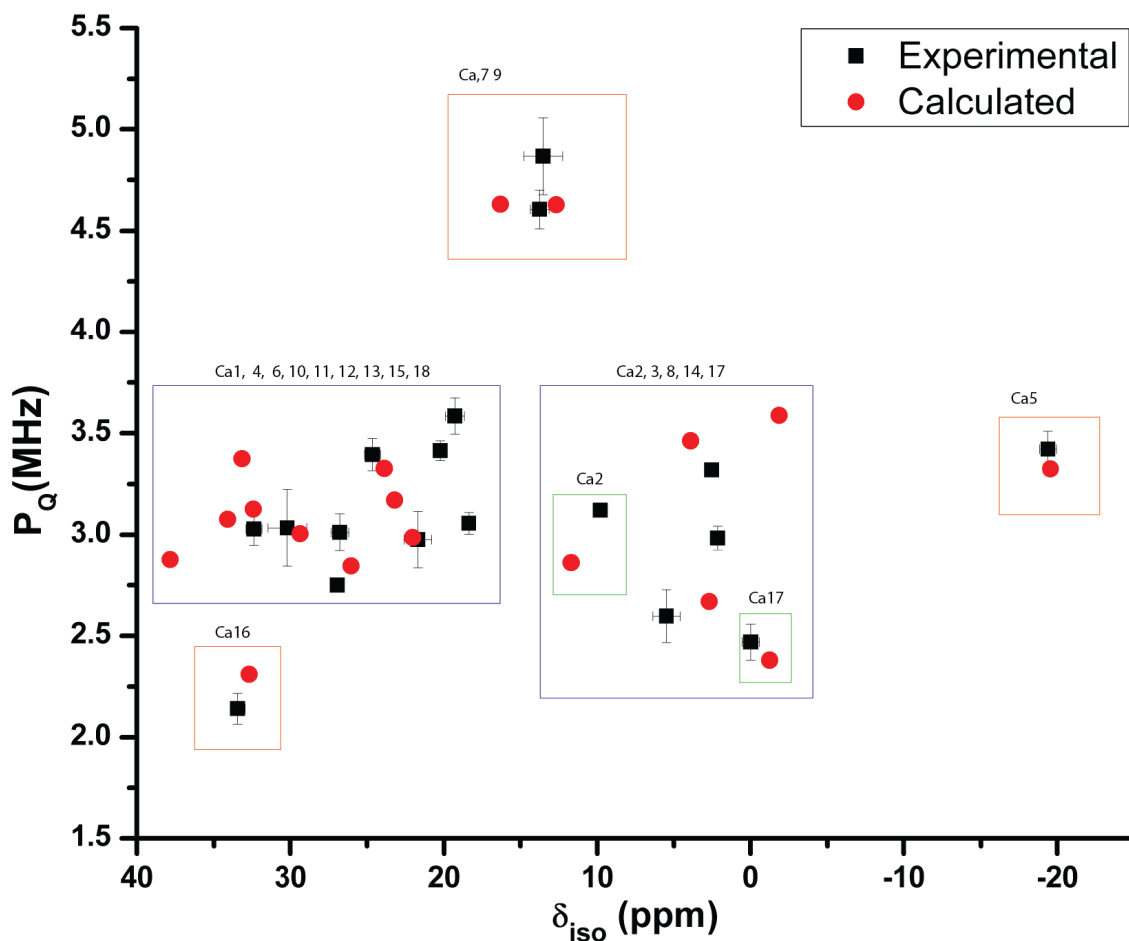
Figure 6.8: Isotropic shift versus $P_Q$ for experimental (squares) and calculated (circles). Overall a good correlation between the two sets of data is seen, while not good enough to achieve a complete assignment of the crystal sites, some isolated sites can still be assigned to within one or two positions in the unit cell and are marked on the plot. Some are more tentative (Ca16, Ca2 and Ca17) and the remaining resonances can only be assigned as a general group.

respectively.

At this stage there does not appear to be any easily identifiable structural trend with the values of $\delta_{iso}$. As the literature currently stands, the $^{43}$Ca isotropic chemical shift is related to structure by the average bond length of the Ca-O unit [139] and the coordination number [140]. Studies of borates, silicates and aluminates have found that $^{43}$Ca $\delta_{iso}$ values becomes more negative with increasing bond length of the primary calcium coordination sphere, the corresponding data was less clear for calcium phosphate systems [41]. Nevertheless, a study of hydroxyapatite with a hexagonal unit cell [39], found that the site with the shortest average bond length and lowest coordination did

in fact appear at a more positive shift than that of the site with higher coordination and longer average bond lengths.

This is clearly not the case here, the $\alpha$-TCP system offers an excellent distribution of coordination numbers ranging from five to nine, however the nine coordinated Ca site (assigned as Ca7), which exhibits the longest average bond length at 2.6297 Å only appears in the middle of the $\delta_{iso}$ range. The most upfield (negatively shifted) resonance, is assigned to seven coordinated Ca site (Ca5) with average Ca-O distance of 2.5598 Å, despite the fact that there are three other sites with longer average Ca-O bonds than this in the sample, namely Ca6, Ca7 and Ca9. Hence, while a correlation with Ca-O distance was found for other calcium minerals this relationship does not appear to be quite that straightforward for $\alpha$-TCP.
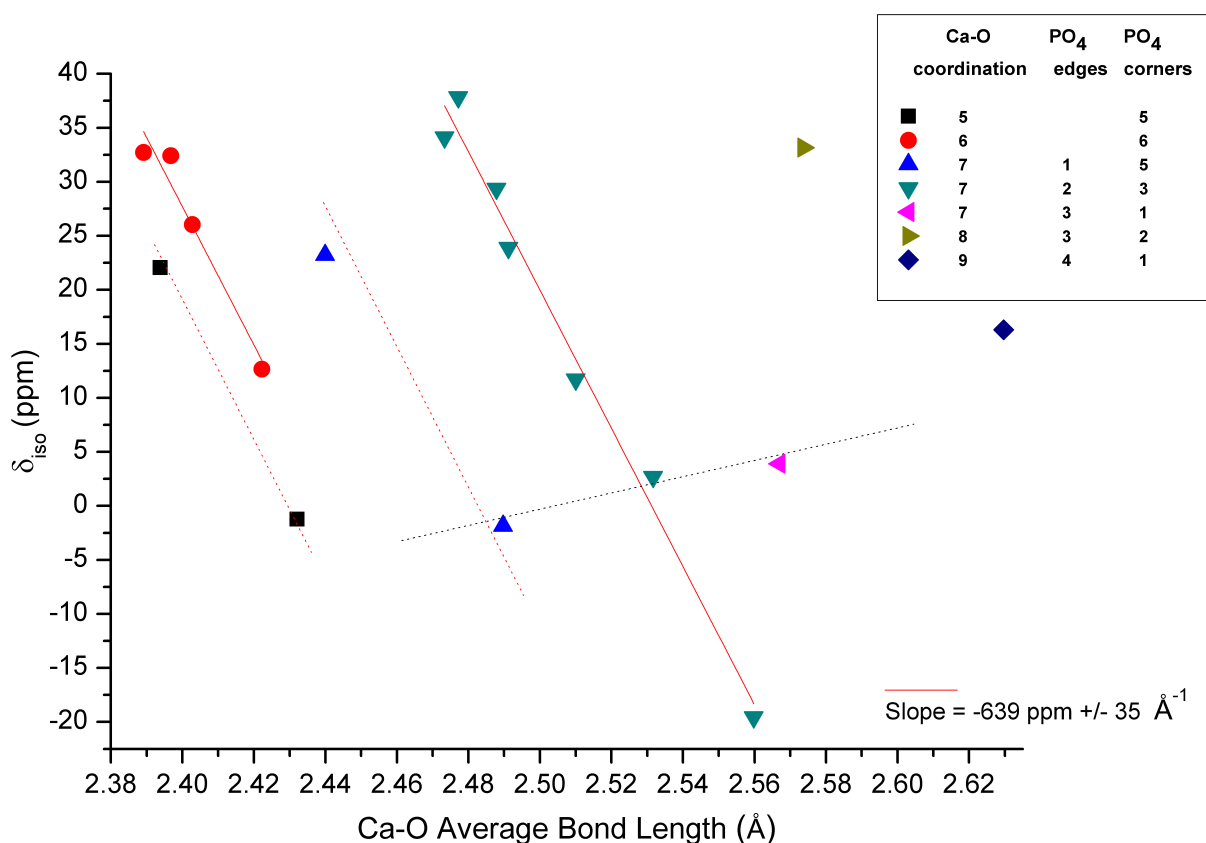


Figure 6.9: Plot of calculated $\delta_{iso}$ versus the calculated average Ca-O distance (Å) a trend is apparent when each calcium geometry is split into coordination number and by the number and type of tetrahedral connections. Dotted lines (red) show that even though only through two points they essentially have the same gradient as the calculated slope. The horizontal dotted line (black) highlights how the intercept will change for seven coordinated moieties depending on the number of edge connections.

While there was no obvious global trend linking the $^{43}$Ca $\delta_{iso}$ values with either the coordination number or Ca-O bond length, a more detailed analysis was performed, rationalizing the calculated $\delta_{iso}$ values with the average Ca-O distance for each Ca geometry and specific number of tetrahedral $PO_4^{3-}$ connections provides some very clear indications. It is not until the actual Ca-O coordination number *and* the number of edge shared and corner shared $PO_4^{3-}$ tetrahedra are fully accounted for does the full information content of Figure 6.9 become apparent. The behaviour of the calculated $\delta_{iso}$ with these more structurally defined moieties is now quite clearly defined, although some of these correlations are defined only by two points while some others (three configurations) are represented by a single point. While nothing can be concluded about the single points regarding a trend, the two groups of double points are still important as they can be considered to have the same gradient as the group of four and the group of seven. It is established that the gradient is 639($\pm$35) ppm/Å and is common to all of these sub-groups, and the only aspect that differentiates these subgroups is the intercept. This gradient is considerably larger than that reported by Geravais *et al* [41] who reported a value of 190 ppm/Å.

The seven coordinated Ca environments produce the clearest trend with increasing Ca-O bond length directly correlated with a more negative $\delta_{iso}$ value. However this only pertains to those Ca positions possessing the same type of $PO_4$ connection; i.e. two edge shared and three corner shared. The three other seven coordinated Ca sites define other lines which are clearly shifted from this in terms of $PO_4$ connectivity and average Ca-O distances. While a lot of information cannot be elucidated from a single point, it is clear that decreasing the $PO_4$ edge sharing character results in a marked decrease in average Ca-O distance. Similarly, if the points representing the five and six coordinated Ca environments are observed, the gradient is the same as that observed for the seven coordinated data but different intercepts are maintained through out. This type of behaviour where the intercept changes but the slope remains the same has been highlighted before, but for different families of compound and not within the same sample [139].

However, it appears that not only coordination number and average Ca-O bond length influence the $\delta_{iso}$ value, there is also some influence on the shift caused by

the number of corner connections present. This is illustrated on Figure 6.9 by the black dotted line. These three points are all seven coordinated sites and have similar $\delta_{iso}$ values. However, they have very different average Ca-O bond lengths. What differentiates them is the number of $PO_4$ edge sharing connections, the point at 2.4368 Å, has one, the point at 2.5316 Å has two and the point at 2.5669 Å has three. This would suggest that the shielding seen at the $^{43}$Ca nucleus is somewhat less for the same number of bonds when more of them are connected to $PO_4$ edges than corners and this will influence the $\delta_{iso}$ range, seen as a change in the intercept. This can tentatively be supported by the two outlying points, the eight and nine coordinated sites, which have a larger number of edge connections than most other sites, three and four respectively, both of these sites have the longest average Ca-O bond lengths. However, they are not the most negatively shifted; there are six other Ca sites at a more negative $\delta_{iso}$ value than these two and all but one have fewer edge connections or none. Whether this apparent behaviour is real and would also be seen with face centred connections to $PO_4$ needs further investigation.

In figure 6.10 is the same plot as Figure 6.9, but with the $\delta_{iso}$ values determined by the DOR experiment and the crystal site data from the original structure [1]. This gives a very similar plot, however in this case the assumption was made that the crystal sites were assigned correctly from the calculations (see Table 6.2), with no further attempt at assigning any of these sites correctly. This is reflected by the poorer quality of the plot, but the same overall theme that was observed with the calculated data is maintained. In this instance the gradient of the slopes is found to be 602($\pm$62) ppm/Å. This result is achieved when using either the experimental bond lengths or the calculated bond lengths, and again the same changes appear with an increasing value for the intercept with additional edge connections.
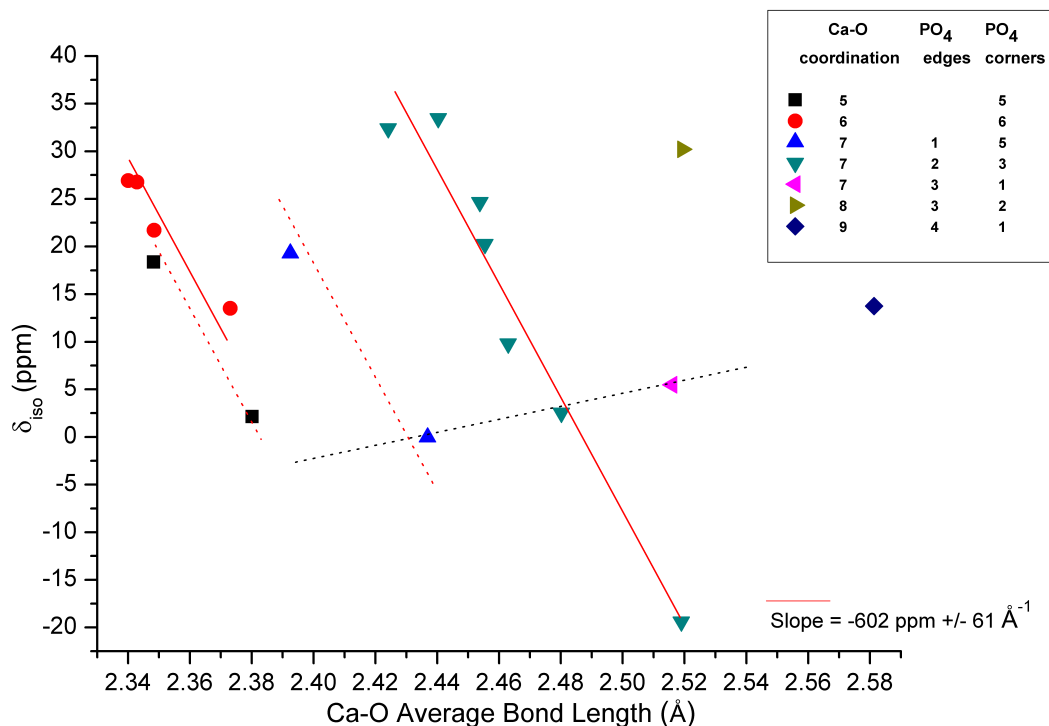
Figure 6.10: Plot of the measured isotropic shifts versus the average Ca-O bond distance (Å) determined by Mathew *et al* [1]. The same phenomena is apparent as in Figure 6.9. However, the plot reflects that the peak assignments are in the wrong order, as they were assigned according to the calculations

### 6.3.3 $^{43}$Ca MAS and DOR NMR studies of Silicon Substituted $\alpha$-TCP

Due to the success with the investigation of $\alpha$-TCP the same DOR experiments were attempted on $^{43}$Ca labelled Si-$\alpha$-TCP. The aim of this was to see if there were any detectable changes with regards to silicon incorporation in the structure. From our results in chapter 5 it has been established that there should be some disorder introduced by Ca-O units bonded only to $SiO_4$ and some Ca-O units bonded to a mixture of $PO_4$ and $SiO_4$. If this was to be the case, this would not only help to get a better understanding of the Si-$\alpha$-TCP, but would also be helpful in understanding how the $^{43}$Ca chemical shift relates to structures with mixed anions.

Unfortunately the results from the $^{43}$Ca MAS and DOR experiments for Si-$\alpha$-TCP in Figure 6.11 show that it is impossible to resolve any individual resonances in either data set. This is attributed to the large degree of chemical shift dispersion similarly observed in the $^{31}$P MAS date discussed in Chapter 5. The localised disorder has made
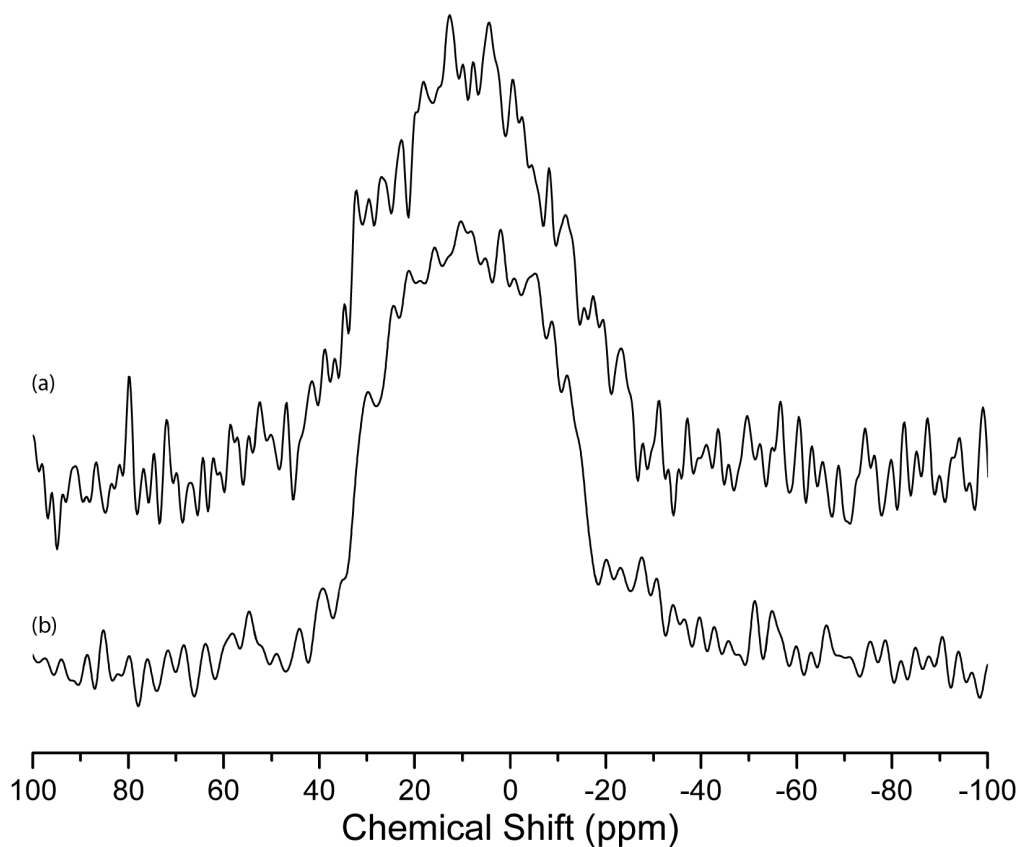
Figure 6.11: Results for Si-$\alpha$-TCP $^{43}$Ca experiments at 20 T (top) MAS spectrum signal-to-noise is poor due to early stoppage of the experiment and (bottom) DOR spectrum, the sample is now quite disordered and unfortunately not even DOR can gain any resolution

it impossible to easily extract any useful information, and while DOR can remove second order quadrupole broadening it cannot narrow lines that are broadened by disorder and chemical shift dispersion. Hence, Figure 6.11 shows very similar results for the MAS and DOR techniques.

## 6.4  Conclusions

While knowledge of the local environments around Ca cations continues to grow, it does remain a challenge to obtain useful $^{43}$Ca solid state NMR data. It has been shown that even with modest levels of enrichment and high magnetic fields good signal to noise can achieved in hours rather than days or weeks. Despite $^{43}$Ca enrichment, the effects of second order quadrupole broadening on spectral resolution when there

are multiple sites, is a significant problem. However, it is shown that this problem can be overcome to a certain extent with the help of calculations, when there are not too many resonances. It has been shown for ordered structures that contain multiple sites that DOR works extremely well in resolving the entire spectrum allowing accurate determination of the isotropic shift and $P_Q$ values for each resonance. While full assignment of the resonances to the crystal sites in $\alpha$-TCP was not possible from the 1D experiment as the calculations are not quite accurate enough for very large structures. Nevertheless, they gave a reasonable correlation with the data and will no doubt improve in the future. The relationship between average coordination number and Ca-O distance with isotropic shift has been confirmed. However, it is found that a third factor has to be taken into account; how neighbouring phosphate tetrahedra connect to the Ca-O geometry. This requires further study in other materials that have multiple sites and different types of connections like this, and should also be checked in different families of materials such as silicates or borates to see if present there too. If this phenomenon is found in other families of materials, then without supporting crystal structure data, this will have far reaching consequences in the study of glasses and amorphous materials, as it will be very difficult to satisfactorily determine the local calcium environments based on chemical shift alone.

# Chapter 7

# Concluding Remarks

## 7.1 Summary

The results of these investigations performed on $\alpha$-TCP and Si-$\alpha$-TCP show that while, experimentally challenging, it is possible to gain significant understanding of the parent structure and the changes that take place upon Si substitution through the use of advanced solid state NMR techniques supported by GIPAW calculations.

$^{31}$P MAS NMR studies show that $\alpha$-TCP is a highly ordered structure, although the observed level of resolution is very much dependant on the purity of the sample. Through the use of 2D $^{31}$P homonuclear re-coupling experiments to establish connectivity, and GIPAW DFT calculations, it is possible to accurately assign each individual resonance of the $^{31}$P MAS NMR spectrum to a specific site in the crystal structure. However, with the level of precision required it is not possible to rely solely on the GIPAW DFT calculations for assignment, as the extreme resolution exhibited by $\alpha$-TCP is testing the lower bound accuracy of the calculations.

Conversely the $^{31}$P MAS NMR and studies of Si-$\alpha$-TCP NMR show that the incorporation of Si in the structure even at low dopant levels causes significant disorder broadening to the spectrum. A comparison of the $^{31}$P MAS NMR data from a number of doped/impure $\alpha$-TCP systems shows that the disorder broadening caused by Si incorporation is markedly greater than that induced by other impurities.

It has been shown through the use of $^{29}$Si enrichment that good quality $^{29}$Si MAS

NMR data can be acquired, and good resolution is achievable despite the relatively low levels of Si in the sample. A full description and analysis of this data is very difficult to ascertain as there are so many overlapping/unresolved $^{29}$Si silicon resonances contributing to this signal. It was established that it was impossible to distinguish between $Q^0$ and $Q^1$ species by using $^{29}$Si MAS NMR alone, despite the breadth of published data in the literature. A certain amount of caution should be exercised when trying to assign Si species in the shift range of –68 to –76 ppm in substituted calcium phosphates in the future. As determined from this study previously unreported $Q^1$ species can exist in this shift range..

It has been shown that despite the low levels of Si present in the Si-$\alpha$-TCP sample, when enrichment is possible more advanced experiments such as the 2D $^{31}$P-$^{29}$Si HET-COR experiment are feasible which can provide useful qualitative information about the distribution of Si in the Si-$\alpha$-TCP structure. The majority of the $^{29}$Si-$^{31}$P correlations agree with unit cell positions that are supported by DFT calculations and these were manifest by a charge balance mechanism based around the formation of $O^{2-}$ vacancies where two adjacent cation-anion columns in the structure are bridged by an $Si_2O_7^{6-}$ unit. While some positions appear to be more favourable than others, if the P-P distance is short enough in the original structure, it is possible that $Si_2O_7^{6-}$ will form at all possible positions in the structure.

However, some contradictions and unanswered questions from these results remain. The energy minimisation and structural optimisation calculations for the two different charge balance mechanisms contradict the experimental results, with the $Ca^{2+}$ excess mechanism being predicted as the more energetically favourable option. The theoretically calculated lattice parameters effects suggest that the unit cell should increase in size with the $Ca^{2+}$ excess mechanism, and shrink in size with the $O^{2-}$ vacancy mechanism. This is in contradiction to the XRD results. The formation of the $Q^2$ $Ca_3Si_3O_9$ type structure in the sample and its relationship to the overall picture is poorly understood. However, it does appear to increase in intensity at higher levels of Si substitution. Taking this along with evidence that a $C_2S$ phase might also be present in the structure, and can exist as a solid solution, then it allows for the possibility that there is some dual process of charge balance in the structure, consisting of mostly $O^{2-}$

vacancies with some $Ca^{2+}$ excess in the structure. This could explain why there are contradictions between the observed and calculated data, and needs to be investigated further.

These multinuclear SS NMR investigations of $\alpha$-TCP show that DOR is a very applicable technique to the $^{43}$Ca nucleus, in part because high spinning speeds are not required and the $C_Q$ range is relatively small. However, it does require $^{43}$Ca enrichment to make the measurements achievable. It was possible to measure $P_Q$ and $\delta_{iso}$ for all eighteen crystallographic Ca sites and it is observed that $P_Q$ can vary widely within the sample; at least one site exhibits a $P_Q$ value higher than any other previously reported for the $^{43}$Ca nucleus. Interestingly, the $\delta_{iso}$ range described by the eighteen sites in the $\alpha$-TCP sample cover a large part of the total $^{43}$Ca chemical shift range, and all of that previously published for calcium phosphates. It was established that both coordination number and average bond length affect the $\delta_{iso}$ value, the change in coordination number affects the shift range, and the average bond length results in a linear shift within this range. However, it is also apparent that there is a third parameter constraining the $^{43}$Ca chemical shift, and relates to the nearest neighbour configuration defining the immediate Ca-O environment. By partitioning each coordination number into further classification regarding the number of edge and corner shared $PO_4^{3-}$ tetrahedra in the immediate environment, excellent linear correlations between $\delta_{iso}$ and the average Ca-O distance can be observed.

The $^{43}$Ca DOR studies of the Si-$\alpha$-TCP system are similar in nature to that of the $^{31}$P MAS NMR results on the same structure. These results show that the disorder is not just localised to the P sites in the structure as the chemical shift dispersion has removed all features from the $^{43}$Ca data.

## 7.2 Future Work

Many of the probes into the distribution of the Si in the Si-$\alpha$-TCP structure have given some satisfactory answers. However there does remain the question of what roles do $Ca_3Si_3O_9$ and possibly C$_2$S play in the structure, if any. Answering this will be extremely difficult, as the amount of Si involved is very small, and in the case of

$Ca_3Si_3O_9$ it makes up less than 5% of the total Si in the sample. Hence experiments like 2D $^{31}P$-$^{29}Si$ HETCOR are no longer a viable option for studying this minor component. Likewise, while able to prove the existence of $Q^1$ species, trying to prove that some of the Si speciation is definitely $Q^0$ is problematic and will require a different approach.

While the results are not completely conclusive on the Si-$\alpha$-TCP structure, the extreme sample and the potential number of Si locations in this system have demonstrated the problems associated with studying a system of this nature. The techniques applied here have shown that they can have general utility in other substituted calcium phosphate materials, in order to gain information about the location of substituted ions in the structure. Indeed, in relative terms it should be easier to interpret the data for smaller unit cells; for example, Si substituted hydoxyapatite which has only one or three possible crystallographic locations to accommodate the Si depending on the structural model used. Furthermore there is no reason why the HETCOR experiment should be limited to the $^{31}P$-$^{29}Si$ case, and theoretically it could be applied to any substituted calcium phosphate as long as the substituted nucleus is of high enough abundance.

The $^{43}Ca$ studies can be continued to other compounds of the calcium phosphate family using a combination of first principles GIPAW DFT calculations and DOR NMR, however enriched samples are still required. As demonstrated in this study the level of enrichment need not be much higher than 10%. This will allow a large body of data to be assembled to thus gain a better understanding of the relationship between structure and $^{43}Ca$ chemical shift. This method of study can also be extended to other calcium families, especially the calcium silicates which have crystal structures containing > 20 Ca positions.

# References

[1] Mathew, M. Schroder, L.W., Dickens, B., Brown, W.E. The crystal structure of $\alpha$-Ca$_3$(PO$_4$)$_2$. *Acta crystallographica*, B33:1325–1333, 1976.

[2] Ratner, B.D., Hoffman, A.S., Schoen, A.S., Lemons, J.E. *Biomaterials Science: An Introduction to Materials in Medicine*. Academic Press, 1996.

[3] Bhat, S.V. *Biomaterials*. Kluwer, 2002.

[4] Williams, D.F. Definitions in biomaterials: Proceedings of a consensus conference of the european society of biomaterials. 4, 1986.

[5] Nicholson, J.W. *The Chemistry of Medical and Dental Materials*. The Royal Society of Chemistry, 2002.

[6] Habibovic, P., Barralet, J.E. Bioinorganics and biomaterials: Bone repair. *Acta Biomaterialia*, 7:3013–3026, 2001.

[7] Grégoire, M., Orly, I., Menanteau, J. The influence of calcium phosphate biomaterials on human bone cell activities: An in vitro approach. *Journal of Biomaterial Research*, 24:165–177, 1990.

[8] Bagambisa, F.-B., Joos, U., Schilli, W. The interaction of osteogenic cells with hydroxylapatite implant materials in vitro and in vivo. *International Journal of Oral Maxillofac Implants*, 5:217–226, 1990.

[9] Ravaglioli, A, Krajewski, A. *Bioceramics*. Chapman and Hall, 1992.

[10] Mow, V.C, Huiskes, R. *Basic Orthopedic Bioceramics and Mechano-Biology*. Lippincott Williams Wilkins, 2005.

[11] Hench, L.L., Wilson, J. *An Introduction to Bioceramics*. World Sientific, 1993.

[12] Gibson, I.R., Bonfield, W.J. Preperation and characterization of magnesium/carbonate co-substituted hydroxyapatites. *Journal of Materials Science: Materials in Medicine*, 13:685–693, 2002.

[13] Martin, R.B., Burr, D.B., Sharkey, N.A. *Skeletal Tissue Mechanics*. Springer, 1998.

[14] Parfitt, A.M. Bone and plasma calcium homeostasis. *Bone*, 8:S1–8, 1987.

[15] Miller, S.C., Jee, W.S.S. Bone lining cells. in bone: Bone metabolism and mineralization. *Bone*, 4:1–19, 1992.

[16] Nery E.B., LeGeros, R.Z., Lynch, K.L., Lee, K. Tissue response to biphasic calcium phosphate ceramic with different ratios of HA/beta TCP in periodontal osseous defects. *Jounal of Periodontol*, 63:729–735, 1992.

[17] S. Carrodeguas, R.G., De Aza. $\alpha$-Tricalcium phosphate: Synthesis, properties and biomedical applications. *Acta Biomaterialia*, 7:3536–3546, 2011.

[18] Vallet-Regi, M., González-Calbet, J.-M. Calcium phosphates as substitution of bone tissues. *Progress in Solid State Chemistry*, 32:1–31, 2004.

[19] Christel, P., Meunier, A., Dorlot, J.-M., Crolet, J.-M., Witvoet, J., Sedel, L., Boutin, P. Biomechanical compatibility and design of ceramic implants for orthopedic surgery. *Annals of the New York Academy of Sciences*, 523:234–256, 1988.

[20] Hastings, G.W., Williams, D. *Mechanical properties of Bioamterials*. Wiley, 1980.

[21] Sudarsana, K., Young, R.A. Significant precision in crystal structural details: Holly springs hydroxyapatite. *Acta crystallographica*, B25:1534–1543, 1969.

[22] Stephen, J.A., Skakle, J.M.S., Gibson, I.R. Synthesis of novel high silicate-substituted hydroxyapatite by co-substitution mechanisms. *Key Engineering Materials (Bioceramics)*, 330-332:87–90, 2006.

[23] Langstaff, S., Sayer, M., Smith, T.J.N., Pugh, S.M., Hesp, S.A.M., Thompson, W.T. Resorbable bioceramics based on stabilized calcium phosphates. Part I: rational design, sample preperation and material characterization. *Biomaterials*, 20:1727–1742, 1999.

[24] Patel, N., Best, S.M., Bonfield, W., Gibson, I.R., Hing, K.A., Damien, E., Revell, P.A. A comparitive study on the in vivo behaviour of hydroxyapatite and silicon substituted hydroxyapatite granules. *Journal of Materials Science: Materials in Medicine*, 13:1199–1206, 2002.

[25] Vallet-Regi, M., Arcos, D.,. Silicon substituted hydroxyapatites: A method to upgrade calcium phosphate based implants. *Journal of Materials Chemistry*, 15:1509–1516, 2005.

[26] Zou, S., Huang, J., Best, S., Bonfield, W. Crystal imperfection studies of pure and silicon substituted hydroxyapatite using raman and XRD. *Journal of Materials Science: Materials in Medicine*, 16:1143–1148, 2005.

[27] Tang, X.L., Xiao, X.F., Liu, R.F. Structural characterization of silicon-substituted hydroxyapatite synthesized by a hydrothermal method. *Materials Letters*, 59:3841 – 3846, 2005.

[28] Vallet-Regi, M., Rodriguez-Carvajala, J., Arcos, D. The effect of the silicon incorporation on the hydroxylapatite structure: A neutron diffraction study. *Solid State Sciences*, 6:987–994, 2004.

[29] Gomes, S., Nedelec, J.-M., Jallot, E., Sheptyakov, D., Renaudin, G. Silicon location in silicate-substituted calcium phosphate ceramics determined by neutron diffraction. *Crystal Growth and Design*, 11:4017–4026, 2011.

[30] Yin, X., Stott, M.J. Theoretical insights into bone grafting silicon-stabilized $\alpha$–tricalcium phosphate. *The Journal of Chemical Physics*, 122:024709–1, 2005.

[31] Langstaff, S., Sayer, M., Smith, T.J.N., Pugh, S.M. Resorbable bioceramics based on stabilized calcium phosphates. Part II: Evaluation of biological response. *Biomaterials*, 22:135–150, 2001.

[32] Andrew, E.R. *Magic Angle Spinning: Encyclopedia of Magnetic Resonance.* John Wiley and sons Ltd., 2007.

[33] Jäger, C., Welzel, T., Meyer-Zaika, W., Epple, M. A solid-state NMR investigation of the structure of nanocrystalline hydroxyapatite. *Magnetic Resonance in Chemistry*, 44:573–580, 2006.

[34] Bohner, M., Lemaitre, J., Legrand, A.P., d'Espinose dela Caillerie, J.-B., Belgrand, P. Synthesis, X-ray diffraction and solid-state $^{31}$P magic angle spinning NMR study of $\alpha$-tricalcium othophosphate. *Journal of Materials Science: Materials in Medicine*, 7:457–463, 1996.

[35] Kim, S.-R., Riu, D.H., Lee, Y.J., Kim., Y.H. Synthesis and characterization of silicon substituted hydroxyapatite. *Key Engineering Materials*, 218-220:85–88, 2002.

[36] Gasquères, G., Bonhomme, C., Maquet, J., Babonneau, F., Hayakawa, S., Kanaya, T., Osaka, A. Revisiting silicate substituted hydroxyapatite by solid state NMR. *Magnetic Resonance in Chemistry*, 46:342–346, 2008.

[37] Rawal, A., Wei, X., Akinc, M., Schmidt-Rohr, K. Disperssion of silicate in tricalcium phosphate elucidated by solid-state NMR. *Chemistry of Materials*, 20:2583–2591, 2008.

[38] Gillespie, P., Wu, G., Sayer, M., Stott, M.J. Si complexes in calcium phosphate biomaterials. *Journal of Materials Science: Materials in Medicine*, 21:99–108, 2010.

[39] Laurencin, D., Wong, A., Dupree, R., Smith, M.E. Natural abundance $^{43}$Ca solid state NMR characterisation of hydroxyapatite: identification of the two calcium sites. *Magnetic Resonance in Chemistry*, 46:347–350, 2007.

[40] Laurencin, D., Wong, A., Hanna, J.V., Dupree, R., Smith, M.E. A high resoloution $^{43}$Ca solid state nmr study of the calcium sites of hydroxyapatite. *Journal of the American Chemical Society*, 130:2412–2413, 2008.

[41] Gervais, C., Laurencin, D., Wong, A., Pourpoint, F., Howes, A.P., Pike, K.J., Dupree, R., Mauri, F., Bonhomme, C., Smith, M.E. New perspectives on calcium environments in inorganic materials contianing calcium-oxygen bonds: a combine computational-experimental $^{43}$Ca approch. *Chemical Physics Letters*, 464:42–48, 2008.

[42] Pourpoint, F., Diogo, T.C., Gervais, C., Bonhomme, C., Fayon, F., Dalicieux, S.L., Gennero, I., Salles, J.-P., Howes, A.P., Dupree, R., Hanna, J.V., Smith, M.E., Mauri, F., Guerrero, G., Mutin, P.H., Laurencin, D. High-resolution solid state NMR experiments for the characterization of calcium phosphate biomaterials and biominerals. *Journal of Materials Research*, 26:2355–2368, 2011.

[43] Abragam, A. *Principles of Nuclear Magnetism*. Oxford, 1962.

[44] Levit, M.H. *Spin Dynamics: Basics of Nuclear Magnetic Resonance*. Wiley, 2001.

[45] Duer, M.J. *Introduction to Solid-State NMR Spectroscopy*. Blackwell, 2004.

[46] Harris, R.K. *Nuclear Magnetic Resonance Spectroscopy*. Pitman, 1983.

[47] Kittel, C. *Introduction to Solid State Physics - 7th ed.* Wiley, 1996.

[48] Stejskal, E.O., Memory, J.D. *High Resolution NMR in the Solid State*. Oxford, 1994.

[49] Gerstein, B.C., Dybowski, C.R. *Transient Techniques in NMR of Solids: An Introduction to Theory and Practice*. Academic Press, 1985.

[50] Fukushima, E., Roeder, S.B.W. *Experimental Pulse NMR: A Nuts and Bolts Approach*. Addison-Wesley, 1981.

[51] MacKenzie, K.J.D., Smith, M.E. *Multinuclear Solid-State NMR of Inorganic Materials*. Pergamon, 2002.

[52] Pearson, R.M. *Instrumation for the Home Builder: Encyclopedia of Magnetic Resonance*. John Wiley and sons Ltd., 2007.

[53] Hill, H.D.W. *Spectrometers: A general Overview: Encyclopedia of Magnetic Resonance.* John Wiley and Sons Ltd., 2007.

[54] Doty, F.D. *Probes for Instrumentation: Encyclopedia of Magnetic Resonance.* John Wiley and sons Ltd., 2007.

[55] Hill, H.D.W. *Probes for High Resoloution: Encyclopedia of Magnetic Resonance.* John Wiley and sons Ltd., 2007.

[56] McKay, R.A. *Probes for Special purposes: Encyclopedia of Magnetic Resonance.* John Wiley and sons Ltd., 2007.

[57] Samoson, A., Lippmaa, E., Pines, A. High-resolution solid state NMR averaging of $2^{nd}$-order effects by means of a double rotor. *Molecular Physics*, 65:1013–1018, 1988.

[58] Dupree, R. *Double Rotation (DOR) NMR: Encyclopedia of magnetic resonance.* John Wiley and sons Ltd, 2011.

[59] Kentgens, A.P.M. A practical guide to solid-state nmr of half integer quadrupolar nuclei with some applicaions to disordered systems. *Geoderma*, 80:271–306, 1997.

[60] Hahn, E.L. Spin echoes. *Physical Review*, 80:580–594, 1950.

[61] Bain, A.D. Coherence levels and coherence pathways in nmr. a simple way to design phase cycling procedures. *Journal of Magnetic Resonance*, 56:418–427, 1984.

[62] Bodenhausen, G., Kogler, H., Ernst, R.R. Selection of coherence-transfer pathways in nmr pulse experiments. *Journal of Magnetic Resonance*, 58:370–388, 1984.

[63] Freeman, R., Hill, H.D.W. Spin-lattice relaxation in high-resoloution NME spectra of carbon-13. *Journal of Chemical Physics*, 53:4103–4105, 1970.

[64] Freeman, R., Hill, H.D.W. Fourier transform study of nmr spin-lattice relaxation by progressive saturation. *Journal of Chemical Physics*, 54:3367–3377, 1971.

[65] Granwehr, J. Multilicative or $t_1$ noise in NMR spectroscopy. *Applied Magnetic Resonance*, 32:113–156, 2007.

[66] Spiess, H.W. *Double quantum NMR spectroscopy of dipolar coupled spins under fast magic angle spinning: Encyclopedia of Magnetic Resonance.* John Wiley and sons Ltd., 2007.

[67] Lee, Y.K, Kurur, M., Helmle, M, Johannessen, O.G., Nielsen, N.C, Levitt, M.H. Efficient dipolar recoupling in the nmr of rotating solids a sevenfold symmetric radiofrequency pulse sequence. *Chemical Physics Letters*, 242:304–309, 1995.

[68] Lopez, J.J, Kaiser, C., Shastri, S, Glaubitz, C. Double quantum filtering homonuclear MAS NMR correlation spectra: A tool for membrane protien studies. *Journal of Biomolecular NMR*, 41:97–104, 2008.

[69] Carravetta, M., Edén, M., Johannessen, O.G., Luthman, H., Verdegem, P.J.E., Lugtenburg, J., Sebald, A., Levitt, M.H. Estimation of carbon-carbon bond lengths and medium-range internuclear distances by solid-state nuclear magnetic resonance. *Journal of the American Chemical Society*, 123:10628–10638, 2001.

[70] Carravetta, M., Edén, M., Zhao, X., Brinkmana, A., Levitt, M.H. Symmetry principles for the design of radiofrequency pulse sequences in the nuclear magnetic resonance of rotating solids. *Chemical Physics Letters*, 321:205–215, 2000.

[71] Fayon, F., Massiot. D., Levitt, M.H., Titman, J.J., Gregory, D.H., Duma, L., Emsley, L., Brown, S.P. Through space contributions to two dimensional double quantum J correlation NMR spectra of magic angle spinnng solids. *The Journal of Chemical Physics*, 122:194313, 2005.

[72] Bax, A., Freeman. R., Frenkiel, T.A. An NMR technique for tracing out the carbon skeleton of an organic molecule. *Journal of the American Chemical Society*, 103:2102–2104, 1981.

[73] Lesage, A., Bardet. M., Emsley, L. Through bond carbon-carbon connectivities in disordered solids by NMR. *Journal of the American Chemical Society*, 121:10987–10993, 1999.

[74] Pines, A., Gibby, M.G., Waugh, J.S. Proton enhanced NMR of dilute spins in solids. *Journal of Chemical Physics*, 59:569–590, 1973.

[75] Caravatti, P., Bodenhausen, G., Ernst, R.R. Hetronuclear solid state correlation spectroscopy. *Chemical Phyics Letters*, 89:363–367, 1982.

[76] Hartmann, S.R., Hahn, E.L. Nuclear double resonance in the rotating frame. *Journal of Chemical Physics*, 128:2042–2053, 1962.

[77] Peersen, O.B., Wu. X., Kustanovich, I., Smith, S.O. Variable-amplitude cross-polarisation MAS NMR. *Journal of Magnetic Resoance*, 104:334–339, 1993.

[78] L.L. Hench. Bioceramics. *Journal of the American Ceramic Society*, 81:1705–1728, 1998.

[79] M. Jarcho. Calcium-phosphate ceramics as hard tissue prosthetics. *Clinical Othopaedics and Related Research*, 157:259–278, 1981.

[80] Cook, S.D., Thomas, K.A., Haddad, R.J., Jarcho, M., Kay, J. Hydroxyapatite-coated titanium for orthopedic implant applications. *Clinical Othopaedics and Related Research*, 232:225–243, 1988.

[81] Dickens, B., Schroder, L.W., Brown, W.E. The crystal structure of pure $\beta$-$Ca_3(PO_4)_2$. *Journal of Solid State Chemistry*, 10:232–248, 1974.

[82] Yashima, M., Sakai, A. High-temperatue neutron powder diffraction study of the structural phase transition beween $\alpha$ and $\alpha$' phases in tricalcium phosphate $Ca_3(PO_4)_2$. *Chemical Physics Letters*, 372:779–783, 2003.

[83] Fix, W., Heymann, H., Heinke, R. Subsolidus relations in the system 2Ca.SiO2–3CaO.P2O5. *Journal of the American Ceramic Society*, 52:346–347, 1969.

[84] Duncan, J. *et al.* Work in progress. 2012.

[85] Ried, J.W., Tuck, L., Sayer, M., Fargo, K., Hendry, J.A. Synthesis and characterization of single-phase silicon-substituted $\alpha$–tricalcium phosphate. *Biomaterials*, 27:2916–2925, 2006.

[86] Sayer, M., Stratilatov, A.D., Reid, J., Calderin, L., Stott, M.J., Yin, X., MacKenzie, M., Smith, T.J.N., Hendry, J.A, Langstaff, S.D. Structure and composition of silicon-stabilized tricalcium phosphate. *Biomaterials*, 24:369–382, 2003.

[87] Yin, X., Stott, M.J. $\alpha$ and $\beta$-Tricalcium phosphate: A density functional study. *Physical Review B*, 68:205205, 2003.

[88] Mackay, A.L. A preliminary examination of the structure of $\alpha$-Ca$_3$(PO$_4$)$_2$. *Acta Crystallographica*, 6:743, 1953.

[89] Gossner, B. Glaserite. *Neues Jahrbuch fr Mineralogie*, 57A:89–116, 1928.

[90] Massie, I., Skakle, J.M.S., Gibson, I.R. Synthesis and phase stability of silicate-substituted alpha-tricalcium phosphate. *Key Engineering Materials*, 361–3631:67–70, 2008.

[91] Yashima, M., Kawaike, Y., Tanaka, M. Determination of precise unit-cell paramaters of the $\alpha$-tricalcium phosphate phase Ca$_3$(PO$_4$)$_2$ through high-resolution synchrotron powder diffraction. *Journal of the American Ceramic Society*, 90:272–274, 2007.

[92] Accelrys Inc., 10188 Telesis Court, Suite 100 San Diego, CA 92121, USA.

[93] Clark, S.J., Segall, M.D., Pickard, C.J., Hasnip, P.J., Probert, M.J., Refson, K., Payne, M.C. First principles methods using CASTEP. *ZEITSCHRIFT FUR KRISTALLOGRAPHIE*, 220:567–570, 2005.

[94] Perdew, J.P., Chevary, J.A., Vosko, S.H., Jackson, K.A., and Pederson, M.R., Singh, D.J., Fiolhais, C. Atoms, molecules, solids, and surfaces - applications of the generalized gradient approximation for exchange and correlation. *Physical Review b*, 46:6671–6687, 1992.

[95] Profeta, M., Benoit, M., Mauri, F., Pickard, C.J. First-principles calculation of the $^{17}$O NMR parameters in Ca oxide and Ca aluminosilicates: the partially covalent nature of the Cao bond, a challenge for Density Functional Theory. *Journal of the American Chemical Society*, 126:12628–12635, 2004.

[96] Pickard, C.J., Mauri, F. All-electron magnetic response with pseudopotentials: NMR chemical shifts. *Physical Review b*, 63:245101, 2001.

[97] Yates, J.R., Pickard, C.J., Mauri, F. Calculation of NMR chemical shifts for extended systems using ultrasoft pseudopotentials. *Physical Review b*, 76:024401, 2007.

[98] Massiot, D., Fayon, F., Capron, M., King, I., Le Calvé, S., Alonso, B., Durand, J.O., Bujoli, B., Gan, Z., Hoasten, G. Modelling one and two dimensional solid-state nmr spectra. *Magnetic Resonance in Chemistry*, 40:70–76, 2002.

[99] Turner, G.L., Smith, K.A., Kirkpatrick, R.J., Oldfield, E. Structure and cation effect on phosphorous–31 NMR chemical shifts and chemical–shift anisotropies of orthophosphates. *Journal of Magnetic Resoance*, 70:408–415, 1986.

[100] Cheetham, A.K., Clayden, N.J., Dobson, C.M., Jakeman, J.B. Correlations between $^{31}$P N.M.R chemical shifts and structural paramaters in crystalline inorganic phosphates. *Journal of the American Chemical Society Communications*, 3:195–197, 1986.

[101] Bohner, M. Silicon-substituted calcium phosphates – a critical view. *Biomaterials*, 30:6403–6406, 2009.

[102] Oldfield, E., Kinsey, R.A., Smith, K.A., Nichols, J.A., Kirkpatrick, R.J. High resolution NMR of inorganic solids, influence of magnetic centers on magic–angle sample spinning lineshapes in some natural aluminosilicates. *Journal of Magnetic Resonace*, 51:325–329, 1982.

[103] Johnston, J.C., Luliucci, R.J., Facelli, J.C., Fitzgerald, G., Mueller, K.T. Intermolecular shielding contributions studied by modeling the $^{13}$c chemical-shift tensors of inorganic single crystals with plane waves. *The Journal of Chemical Physics*, 131:144503, 2009.

[104] Witter, R., Hartmann, P., Vogel, J., Jäger, C. Measurements of chain length distribution in calcium phophate glasses using 2d $^{31}$P double quantum NMR. *Solid State Nuclear Magnetic Reonance*, 13:189–200, 1998.

[105] Obadia, L., Deniard, P., Alonso, B., Rouillon, T., Jobic, S., Guicheux, J., Julien, M., Massiot, D., Bujoli, B., Bouler, J. Effect of sodium doping in $\beta$-Tricalcium phosphate on its structure and properties. *Journal of the American Ceramic Society*, 18:1425–1433, 2006.

[106] Enderle, R., Gotz-Neunhoeffer, F., Gobbels, M., Muller, F.A., Greil, P. Influence of magnesium doping on the phase transformation temperature of $\beta$-TCP ceramics by Rietveld refinement. *Biomaterials*, 26:3379–3384, 2005.

[107] Duncan, J. *Silicon-Containing $\alpha$-Tricalcium Phosphate*. PhD thesis, University of Aberdeen, 2012.

[108] Tilley, C.E. Tricalcium disilicate (rankinite), a new mineral from Scawt Hill, Co. Antrim. *Mineral Magazine*, 28:190–196, 1942.

[109] Yamanaka, T., Mori, H.,. The structure and polytypes of alpha - $CaSiO_3$(psuedowollasonite). *Acta Crystallographica Section b-Structural science*, 37:1010–1017, 1981.

[110] Martínez, I.M., Velásquez, P.A, De Aza, P.N. Synthesis and stability of $\alpha$-tricalcium phosphate doped with dicalcium silicate in the system $Ca_3(PO_4)_2$-$Ca_2SiO_4$. *Materials Characterization*, 61:761–767, 2010.

[111] Martínez, I.M., Velásquez, Meseguer-Olmo, L., P., De Aza, P.N. Production and study of in vitro behaviour of monolithis $\alpha$-tricalcium phosphate based ceramics in the system $Ca_3(PO_4)_2$-$Ca_2SiO_4$. *Ceramics International*, 37:2527–2535, 2011.

[112] Udagawa, S., Urabe, K., Yano, T. Crystal structure analysis of $\alpha$-$Ca_2SiO_4$. *Semento Hijutsu Nempo*, 31:26–29, 1977.

[113] Dickens, B., Brown, W.E.,. The crystal structure of $Ca_5(PO_4)_2SiO_4$ (Silicocarnotite). *Tschermaks Meneralogische und Petrographische Mitteilungen*, 16:1–27, 1978.

[114] Coelho, C., Babonneau, F., Azais, T., Bohomme-Coury, L., Maquet, J., Laurent, G., Bonhomme, C. Chemical bonding in silicophosphate gels: Contribution of

dipolar and J-derived solid state NMR techniques. *Journal of Sol-Gel Science Technology*, 40:181–189, 2006.

[115] Dupree, R., Lewis, M.H., Leng Ward, G., Williams, D.S. Co-ordination of Si atoms in silicon-oxynitrides determined by magic-angle spinning NMR. *Journal of Materials Science Letters*, 4:393–395, 1985.

[116] Dupree, R., Holland, D., McMillan, P.W., Pettifer, R.F. The structure of soda-silica glasses: A MAS NMR study. *Journal of Non-Crystalline Solids*, 68:399–410, 1984.

[117] Lippmaa, E., Magi, M., Samoson, A., Tarmak, M., Engelhardt, G. Investigation of the structure of zeolites by solid-state high-resoloution 29si nmr spectroscopy. *Journal of the American Chemical Society*, 103:4992–4996, 1981.

[118] Magi, M., Lippmaa, E., Samoson, A., Engelhardt, G., Grimmer, A.-R. Solid-state high-resolution silicon-29 chemical shifts in silicates. *Journal of Physical Chemistry*, 88:1518–1522, 1984.

[119] De Aza, P.N., Guitián, F. Phase diagram of wollastonite-tricalcium phosphate. *Journal of the American Ceramic Society*, 78:1653–1656, 1995.

[120] Gomes, S., Renaudin, G., Jallot, E., Bonhomme, C., Babonneau, F., Nedelec, J.-M. Thorough analysis of silicon substitution in biphasic calcium phosphate bioceramics: A multi-technique study. *Acta Biomaterialia*, 6:3264–3274, 2010.

[121] Sherriff, B.L., Grundy, H.D., Hartman, J.S. The relationship between [29]Si mas nmr chemical shift and silicate mineral structure. *European Journal of Mineralology*, 3:751–768, 1991.

[122] Astala, R.. Calderin, L., Yin, X., Stott, M.J. Ab initio simulation of si-doped hydroxyapatite. *Chemistry of Materials*, 18:413–422, 2006.

[123] Sherriff, B.L., Grundy, H.D. Calculations of ^{29}Si MAS NMR chemical shift from silicate mineral structure. *Nature*, 332:819–822, 1988.

[124] Massiot, D., Fayon, F., Deschamps, M., Cadars, S., Florian, P., Montouillout, V., Pellerin, N., Hiet, J., Rakhmatullin, A., Bessada, C. Detection and use of small J-couplings in solid state NMR experiments. *Comptes Rendus Chimie*, 13:117–129, 2010.

[125] Florian, P., Fayon, F., Massiot, D. 2J Si-O-Si scalar spin–spin coupling in the solid state: Cystalline and glassy wollastonite $CaSiO_3$. *Journal of Physical Chemistry*, 113:2562–2572, 2009.

[126] Shmidt-Rohr, K, Spiess, H.W., (Eds). *Multidimensional Solid-State NMR and Polymers. p.19.* Academic Press, New York, 1996.

[127] Franke, D., Hudalla, C., Maxwell, R., Eckert, H. $^{31}$P-113Cd and $^{31}$P-$^{29}$Si CP/MAS-NMR in inorganic semi conductors. *Chemical Physics Letters*, 96:7506–7509, 1992.

[128] Lejeune, C., Coelho, C., Bohomme-Coury, L., Azais, T., Maquet, J., Bonhomme, C. Studies of silicophosphate derivatives by $^{31}$P-$^{29}$Si CP MAS NMR. *Solid State Nuclear Magnetic Resoance*, 27:242–246, 2005.

[129] Greenwood, N.N., Earnshow, A. *Chemisty of the Elements, $2^{nd}$ Ed.* Butterworth-Heinemann, 1997.

[130] Kokubo, T., Kim, H.-M., Kawashita, M. Novel bioactive materials with different mechanical properties. *Biomaterials*, 24:2161–2175, 2003.

[131] Lowenstein, T.K., Hardie, L.A., Timofeeff, M.N., Demicco, R.V. Secular variation in seawater chemistry and the origin of calcium chloride basinal brines. *Geology*, 31:857–860, 2003.

[132] R.G., Ganapathy, S., Kennedy, S.D. Bryant,. High-resolution calcium-43 NMR in solids. *Journal of Magnetic Resonance*, 72:376–378, 1987.

[133] Trokiner, A., LeNoc, L., Mikhalev, K., Yakubovskii, A, LÜtgemeier, H., Hienmaa, I., Gippus, A., Verkhovskii, S., Goldschmidt, D., Eckstien, Y.,. Structural

properties of CaBaLaCu$_3$O$y$ studied by NMR/NQR method. *Physica*, 226C:43–52, 1994.

[134] Zanni, H., Rassem-Bertolo, R., Massie, S., Fernandez, L, Nieto, P., Breson, B. A spectroscopic NMR investigation of the calcium silicate hydrates present in cement and concrete. *Magnetic Resonance Imaging*, 14:827–831, 1996.

[135] Bryce, D.L. Calcium binding environments probed by $^{43}$Ca spectroscopy. *Dalton Transactions*, 39:8593–8602, 2010.

[136] Siegel, R., Nakashima, T.T., Wasylishen, R.E. Sensitivity enhancement of NMR spectra of half-integer quadrupolar nuclei in the solid state via population transfer. *Concepts in Magnetic Resonance Part A*, 26A:47–61, 2005.

[137] Medek, A., Hrwood, J.S, Frydman, L. Multiple-quantum magic-angle spinning NMR: A new method for the study of quadrupolar nuclei in solids. *Journal of the American Chemical Society*, 117:12779–12787, 1995.

[138] Shimoda, K., Tobu, Y, Kanehashi, K, Nemoto, T., Saito, K,. Local enviornments of slags: The first application of $^{43}$Ca MQMAS NMR technique. *Chemistry Letters*, 34:1588–1589, 2005.

[139] Dupree, R., Howes, A.P., Kohn, S.C. Natural abundance solid state $^{43}$Ca nmr. *Chemical Physics Letters*, 276:399–404, 1997.

[140] Lin, Z., Smith, M.E., Sowrey, F.E., Newport, R.J. Probing the local environment of calcium by natural abundance solid-state $^{43}$Ca NMR. *Physical Review*, 69B:224107, 2004.

[141] Wong, A., Howes, A.P., Dupree, R., Smith, M.E. Natural abundance $^{43}$Ca nmr study of calcium containing organic solids: A model study for Ca-binding biomaterials. *Chemical Physics Letters*, 427:201–205, 2006.

[142] Bryce, D.L., Bultz, E.B, Aebi, D. Calcium-43 chemical shift tensors as probes of calcium binding environments. insight into the structure of the valerite CaCO$_3$

polymorph by $^{43}$Ca solid state NMR spectroscopy. *Journal of the American Chemical Society*, 130:9282–9292, 2008.

[143] Shimoda, K., Tobu, Y, Kanehashi, K, Nemoto, T., Saito, K. Total understanding of the local structures of an amorphous slag: perspective from multi-nuclear ($^{29}$Si, $^{27}$Al, $^{17}$O, $^{25}$Mg, and $^{43}$Ca solid state NMR. *Journal of non-Crystalline Solids*, 354:1036–1043, 2008.

[144] Shimoda, K., Tobu, Y, Kanehashi, K, Saito, K. First evidence of multiple Ca sites in amorphous slag structure: Multiple quantum MAS-NMR spectroscopy on calcium-43 at high magnetic field. *Solid State Nuclear Magnetic Resonance*, 30:198–202, 2006.

[145] Shimoda, K., Tobu, Y, shimoikeda, Y, Nemoto, T., Saito, K. Multiple ca$^{2+}$ environments in silicate glasses by high-resolution $^{43}$Ca MQMAS NMR at high and ulta high (21.8 t) magnetic fields. *Journal of Magnetic resoance*, 34:156–159, 2007.

[146] Wong, A., Laurencin, D., Dupree, R., Smith, M.E. Two-dimensional $^{43}$Ca–$^{1}$H correlation solid state nmr spectroscopy. *Solid State Nuclear Magnetic Resonance*, 35:32–36, 2009.

[147] Golovastikov, N.I., Matveeva, R.G., Belov, N.V. Crystal structure of the tricalcium silicate (Ca O Si O$_2$)$_3$ = C$_3$S. *Kristallografiya*, 20:721–729, 1975.

[148] Moudrakovski, I.L., Alizadeh, R., Beaudoin, J.J. Natural abundance high field $^{43}$Ca solid state NMR in cement science. *Physical Chemistry Chemical Physics*, 12:6961–6969, 2010.

[149] Wong, A., Howes, A.P., Pike, K.J., Lemaître, V., Watts, A., Anupôld, T., Past, J., Samoson, A., Dupree, R., Smith, M.E. New limits for solid state 17o nmr spectroscopy: Complete resoloution of multiple oxygen sites in a simple biomolecule. *Journal of the American Chemical Society*, 128:7744–7745, 2006.

[150] Angeli, F., Gaillard, M., Jollivet, P., Charpentier, T. Contribution of $^{43}$Ca MAS NMR for probing the structural configuration of calcium glass. *Chemical Physics Letters*, 440:324–328, 2007.

[151] Wong, A., Howes, A.P., Yates, J.R., Watts, A., Anupôld, T., Past, J., Samoson, A., Dupree, R., Smith, M.E. Ultra-high rsoloution $^{17}$O solid-state NMR spectroscopy of biomolecules: A comprehensive spectral analysis of monosodium L-glutamate-monohydrate. *Physical chemistry Chemical Physics*, 13:12213–12224, 2011.

[152] Hung, I., Howes, A.P., Parkinson, B.G., Anupôld, T., Samoson, A., Brown, S.P., Harrison, P.F., Holland, D., Dupree, R. Determination of the bond-angle distribution in vitreous $B_2O_3$ by $^{11}$B double rotation(DOR) nmr spectroscopy. *Journal of Solid State Chemistry*, 182:2402–2408, 2009.

[153] Gervais, C., Dupree, R., Pike, K.J., Bonhomme, C., Profeta, M., Pickard, C.J., Mauri, F. Combined first-principle computaitional and experimental mutinuclear solid state nmr investigation of amino acids. *Journal of Physical Chemistry*, 109A:6960–6969, 2005.

[154] Bryce, D.L., Bultz, E.B. Alkaline earth chloride hydrates: Chlorine quadrupolar and chemical shift tensors by solid-state NMR spectroscopy and plane wave pseudopotential calculations. *Chemistry European Journal*, 13:4786–4796, 2007.